SANDIA REPORT

SAND96–0995 • UC–810
Unlimited Release
Printed April 1996

Modeling, System Identification, and Control for Slosh-Free Motion of an Open Container of Liquid

John Feddema, Roy Baty, Ron Dykhuizen, Clark Dohrmann, Gordon Parker, Rush Robinett, Vicente Romero, Dan Schmitt

Prepared by
Sandia National Laboratories
Albuquerque, New Mexico 87185 and Livermore, California 94550
for the United States Department of Energy
under Contract DE-AC04-94AL85000

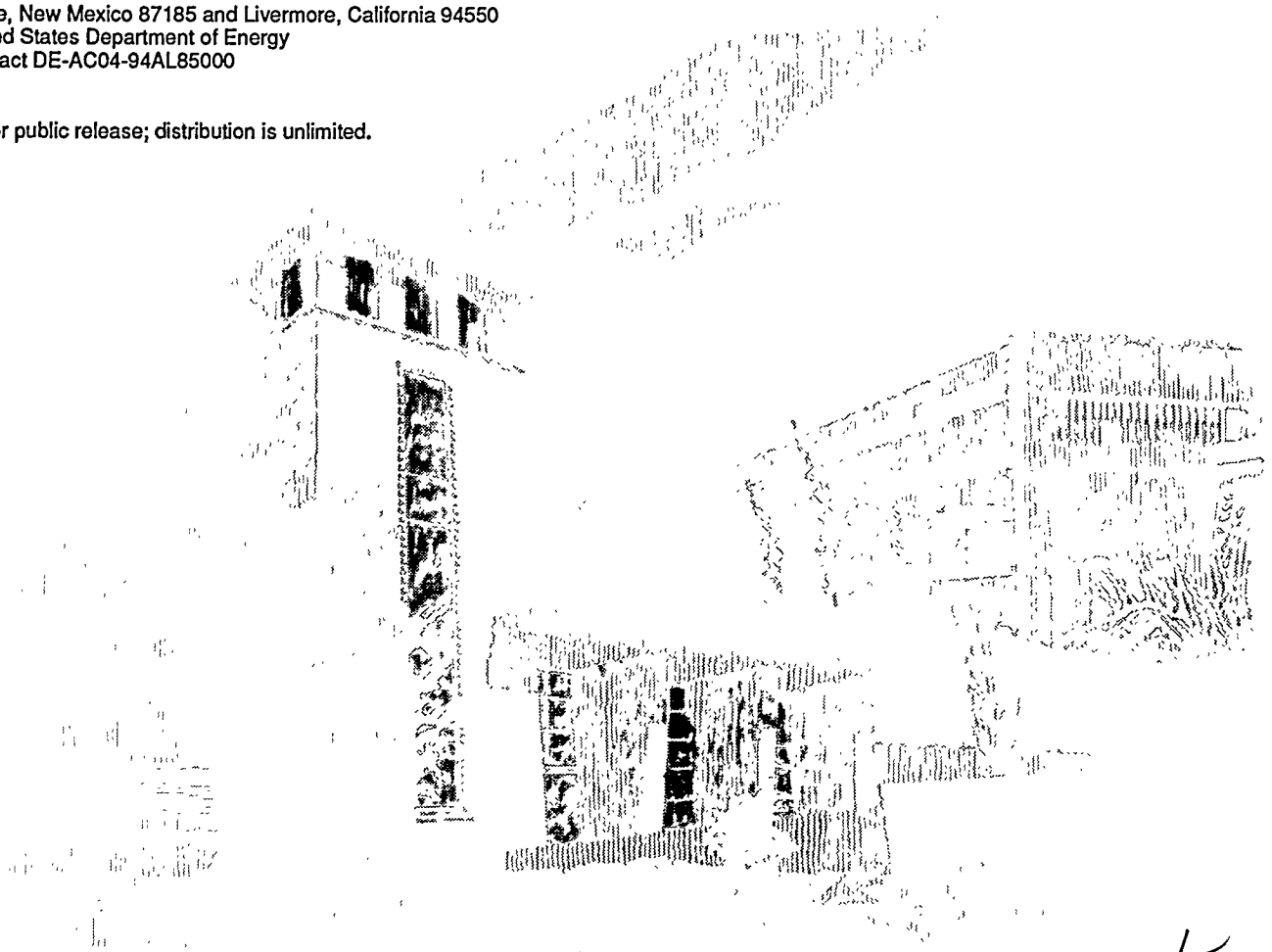

Issued by Sandia National Laboratories, operated for the United States Department of Energy by Sandia Corporation.

Available to DOE and DOE contractors from
Office of Scientific and Technical Information
PO Box 62
Oak Ridge, TN 37831

Prices available from (615) 576-8401, FTS 626-8401

Available to the public from
National Technical Information Service
US Department of Commerce
5285 Port Royal Rd
Springfield, VA 22161

NTIS price codes
Printed copy: A07
Microfiche copy: A01

SAND96-0995
Unlimited Release Category
Printed April 1996

Distribution
UC--810

Modeling, System Identification, and Control for Slosh-Free Motion of an Open Container of Liquid

John Feddema, Intelligent Systems, Sensors & Controls
Roy Baty, Aerosciences and Fluid Dynamics
Ron Dykhuizen, Thermal and Fluid Engineering
Clark Dohrmann, Structural Dynamics
Gordon Parker, Structural Dynamics
Rush Robinett, Intelligent Systems, Sensors & Controls
Vicente Romero, Thermal and Fluid Engineering
Dan Schmitt, Intelligent Systems, Sensors & Controls

Sandia National Laboratories
Albuquerque, NM 87185

ABSTRACT

This report discusses work performed under a Cooperative Research And Development Agreement (CRADA) with Corning, Inc., to analyze and test various techniques for controlling the motion of a high speed robotic arm carrying an open container of viscous liquid. A computer model was generated to estimate the modes of oscillation of the liquid based on the shape of the container and the viscosity of the liquid. This fluid model was experimentally verified and tuned based on experimental data from a capacitive sensor on the side of the container. A model of the robot dynamics was also developed and verified through experimental tests on a Fanuc S-800 robot arm. These two models were used to estimate the overall modes of oscillation of an open container of liquid being carried by a robot arm. Using the estimated modes, inverse dynamic control techniques were used to determine a motion profile which would eliminate waves on the liquid's surface. Experimental tests showed that residual surface waves in an open container of water at the end of motion were reduced by over 95 percent and that in-motion surface waves were reduced by over 75 percent.

Intentionally Left Blank

Figures

1.0 INTRODUCTION

Sandia National Laboratories (SNL) analyzed and tested various techniques for controlling the motion of a robotic arm carrying an open container of viscous liquid, in this case, molten glass. This report is a summary of the work performed under a Cooperative Research And Development Agreement (CRADA) with Corning, Inc.

The objective of the CRADA was to develop and test the concept that an open container of viscous fluid could be moved so as to eliminate surface defects and chill marks. Through dynamic modeling and system identification (Section 2.0), inverse dynamic controls (Section 3.0), and experimental tests (Section 4.0), the Sandia team was able to show that it is possible to control the motion of the robot to eliminate sloshing of a very low viscosity liquid such as water.

We developed a computer model which was used to estimate the modes of oscillation of the liquid based on the shape of the container and the viscosity of the liquid. This model was verified with experimental tests that used a Sandia developed capacitive sensor to measure the oscillation of the liquid. We also developed a mathematical model of the robot dynamics so that we could compensate for tracking errors which occur when the robot moves at high speeds. Because of the large gear ratio of the robot joints, we were able to reduce this model to a single-input single-output set of equations. Using system identification techniques we identified these transfer functions, which appear to be unity for slow speeds and second order for higher speeds.

Three different techniques were used to control the liquid motion. All three required the knowledge of the fundamental mode of oscillation and damping of the liquid within the container as estimated from the fluid model. The first two techniques created near slosh-free motion where the only sloshing of the liquid was during the acceleration and deceleration portion of the robot motion. The third technique eliminated even this sloshing by tilting the container such that the surface normal of the liquid was opposing the resulting acceleration of the robot and gravity.

Intentionally Left Blank

2.0 DYNAMIC MODELING AND SYSTEM IDENTIFICATION

In order to control the liquid in a slosh-free motion both the dynamics of the liquid and the robot arm must be known. The next two subsections describe the mathematical models and the methods of system identification used.

2.1 Fluid Modeling

In support of the Corning CRADA, a broad variety of fluid modeling activities were undertaken in the following areas.

1) Characterization and simulation of fluid sloshing behavior of low viscosity liquids in robotically moved containers;

2) Scaling analyses for estimating flow tendencies of high viscosity liquids (such as molten glass) under various acceleration fields; and

3) Scoping investigation of the computational tools and resources required to solve the coupled thermal/fluid equations for flowing molten glass.

In this section the authors summarize efforts in these areas and point to appendices for more detail as appropriate.

2.1.1 Fluid Sloshing Behavior

In an effort to characterize fluid sloshing behavior, several initiatives were pursued. Appendix A [Baty memo, 6/3/94] reports the details of an analytical separation-of-variables solution for sloshing frequencies with linear wave formation in a potential fluid (*i.e.*, an incompressible, irrotational, inviscid fluid) contained in a right-circular cylinder experiencing constant linear acceleration.

This analysis was followed by development of a computer model for simulating fully transient non-linear (high-amplitude) waves in pseudo-viscous liquids in horizontally moving rectangular containers. The effects of viscosity were approximated by imparting Rayleigh damping to a potential-flow model of the fluid. A boundary element approach with Lagrangian node movement at the liquid-free surface was used to efficiently handle the time-changing fluid geometry and allow for violent sloshing motions. Appendix B [Romero memo, 11/6/94] describes the

numerical model in detail and establishes credibility of the model by comparing results against other nonlinear results in the literature.

Further verification was accomplished by comparing a separation-of-variables series solution of a transient linear model problem with a simulation of the numerical model See Appendix C [Baty memo, 11/18/94]. The nonlinear model performs well in the linear limit, correctly predicting sloshing behavior in the linear flow regime of the model problem. With the 2-D computer model satisfactorily verified, its applicability for modeling the 3-D sloshing of water in horizontally translating containers was investigated. Specifically, model predictions were compared with 3-D sloshing data generated in experiments documented in Section 4.0 of this report. Appendix D [Romero memo, 9/7/95] documents the comparisons.

The model appears to predict sloshing frequency quite well for any type of bowl motion or geometry. However, the amplitudes resulting from forced bowl maneuvers are sometimes considerably over predicted by the model. The over predictions generally get worse as the maneuver becomes more extreme. As a partial remedy, adding surface tension to the model would have a correcting effect on these errors without impacting sloshing frequency appreciably. A Rayleigh damping coefficient of $\mu = 0.55/sec$ results in significantly greater damping rates than experimental data indicate, though this effect can be easily corrected to a large extent by decreasing a single parameter (μ) in the model.

It should also be mentioned that discrepancies between prediction and experiment can be partly attributed to the experimental data itself, which possess appreciable uncertainty because of the substantial drift errors and hysteresis effects evident in the sensor responses. Though considerable differences sometimes exist between simulation and experiment, the results are encouraging, considering that the 2-D model is being used to estimate 3-D sloshing behavior, and that a large potential exists to better reconcile measurements with predictions by adding, changing, and correcting factors in the model and experiments.

2.1.2 Scaling Analyses for Estimating Flow Tendencies

A second aspect of fluids modeling in the CRADA involved scaling analyses for estimating flow tendencies of very viscous liquids (such as molten glass) under various acceleration fields. The goal of this work was to identify candidate motions for increasing the spreading rates of a molten glass "blob" in order to eliminate or reduce surface defects that develop from insufficiently fast spreading. Appendix E [Dykhuizen memo, 1/11/95] analyzes the spreading of a viscous "blob" induced by impact onto a flat substrate. Subsequent spreading of the viscous blob due to

gravity and possible added vertical acceleration of the substrate was also investigated.

Scaling results indicate that the spreading of the blob is not very sensitive to either impact velocity or vertical acceleration. Thus, these factors would have to be increased substantially from their nominal values in the current processes in order to achieve significantly increased spreading rates. A second set of scaling analyses (see Appendix F [Dykhuizen memo, 1/24/95]) investigated shear spreading under lateral accelerations and radial spreading induced by blob rotation. The analysis predicted only a small amount of shear spreading due to nominal lateral accelerations in the current production environment. On the other hand, spinning the blob even at modest rates is predicted to impart significant spreading to the glass.

2.1.3 Computational Tools and Resources Required

Finally, a quick scoping investigation was performed to estimate the computational tools and resources required to solve the coupled thermal/fluid equations for flowing molten glass. The investigation revealed that both commercial and Sandia codes presently exist which can be quickly modified to simulate transient 3-D flows under gravity and other acceleration fields. The computing resources and expertise that would be required are not widely available, but are readily accessible at Sandia. It is estimated that 0.5 man-years of labor would be required for the effort.

2.2 Robot Modeling

In addition to the dynamics of the liquid, the dynamics of the robot must be known in order to control the motion of the open container at high speeds. As will be shown below, at lower speeds the dynamics of the robot are negligible, and it can be assumed that the robot tracks the desired motion profile. However, at higher speeds, the robot does not track the desired motion profile, and the robot dynamics become significant.

When developing hi-performance robot control for speed and tracking, accurate knowledge of the differential equations of motion is required. These equations include measurable physical parameters, such as link geometries and mass properties. However, accurate direct measurements for many of these quantities necessitates the dismantling of the robot. This time consuming task is avoidable if accurate indirect measurements can be made which allow for the computation of the desired physical parameters. There exist many such system identification methods

for non-robotic, linear systems. However, no general techniques exist for nonlinear systems indicative of robots.

A new nonlinear system identification method for robotic systems was developed during this project and is described in detail in Section 2.2.2. For the specific case of the FANUC S-800, the fully coupled, nonlinear differential equations are approximated by a set of decoupled, linear, single-input, single-output equations due to large gear ratio effects. These equations facilitate less complicated methods of slosh-free trajectory design. The justification for the linearization and decoupling of the equations of motion is given in Section 2.2.1.

2.2.1 Equations of Motion

In this section the validity of the linearization and decoupling of the robot equations of motion are examined. First, the fully coupled, nonlinear equations are presented. Next, combined equations are derived including joint gear train assemblies. Finally, the linearizing assumptions are presented.

The nonlinear, coupled differential equations of motion relating joint torque inputs to joint angle outputs may be expressed in the form

$$H_{ij}(x_p)\ddot{x}_j + h_{ijk}(x_p)\dot{x}_j\dot{x}_k + G_i(x_p) = \tau_{Li} \tag{1}$$

where x_p is a vector of joint angles, $H_{ij}(x_p)$ is the configuration dependent inertia matrix of the robot, $h_{ijk}(x_p)$ is the configuration dependent tensor of centrifugal and Coriolis effects, $G_i(x_p)$ is the configuration dependent gravity vector and τ_{Li} is the vector of input joint torques. For the FANUC S-800, the input torques τ_{Li} are supplied by the output torque from a gear train driven by an external power source.

A simple two gear system is shown in Figure 1. While this is most likely not the exact configuration used in FANUC S-800, it illustrates the effects caused by the actual gear train system of the S-800. The torque, τ_i is the torque generated by the power source;

- B_{1i} ,B_{2i} are the coefficients of viscous friction for the gears 1 and 2 of the ith gear train;
- J_{1i} ,J_{2i} are the gear inertias;

- τ_{1i} ,τ_{2i} are the gear torques; and
- τ_{1i} is the total load torque on the gear train caused by the link, and all outboard links.

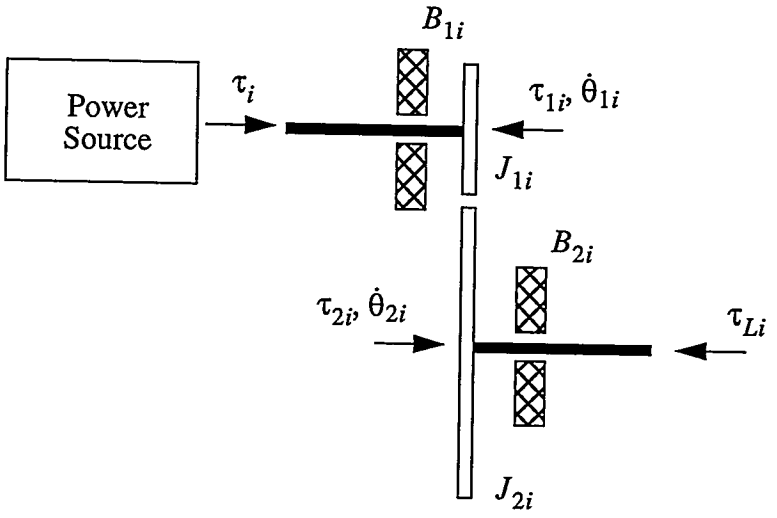

Figure 1 Two Gear Train

The equations of motion for the gear assembly are given by

$$\begin{aligned} J_{1i}\ddot{\theta}_{li} + B_{1i}\dot{\theta}_{li} + \tau_{1i} &= \tau_i \\ J_{2i}\ddot{\theta}_{2i} + B_{2i}\dot{\theta}_{2i} + \tau_{Li} &= \tau_{2i} \\ \frac{-\tau_{1i}}{\tau_{2i}} = \frac{-\theta_{2i}}{\theta_{1i}} &= \frac{N_{1i}}{N_{2i}} \end{aligned} \tag{2}$$

where N_{1i} ,N_{2i} are the number of teeth for gears 1 and 2 of the ith gear assembly.

Combining the relations of equation 2, and noting that θ_{2i} is the angle of the ith joint of the robot, yields a set of equations relating the load torques, τ_{Li}, and the power source torques, τ_i, to the joint angles, x_j as

$$(J_{2ij} + r_{(i)}^2 J_{1ij})\ddot{x}_j + (B_{2ij} + r_{(i)}^2 B_{1ij})\dot{x}_j = r_{(i)}\tau_i + \tau_{Li} \tag{3}$$

where J_{1ij} ,J_{2ij} are diagonal matrices whose elements are the gear inertias J_{1i} ,J_{2i} ; the matrices B_{1ij} ,B_{2ij} are also diagonal with elements of B_{1i} ,B_{2i} ; and the scalar value r_i is the ith gear ratio N_{2i} /N_{1i}.

A combined robot and gear assembly equation of motion, in matrix form, can be found by substituting equation 1 into equation 3 to yield

$$\left(H_{ij} + J_{2ij} + r_{(i)}^2 J_{1ij}\right)\ddot{x}_j + \left(B_{2ij} + r_{(i)}^2 B_{1ij}\right)\dot{x}_j + h_{ijk}\dot{x}_j\dot{x}_k + G_i = r_{(i)}\tau_i \qquad (4)$$

where the dependence of H_{ij} ,h_{ijk} ,G_i on x_p has been omitted to make the notation compact.

Equation 4 represents n differential equations, where n is the number of joints of the robot. In the case of the FANUC S-800, $n = 6$. These equations relate the torque produced by the power source to the physical joint angles. Each equation contains one, and only one, gear ratio r_1. Dividing each equation by the square of its gear ratio clarifies the assumptions required to linearize and decouple the equations of motion. Specifically if the following conditions are valid,

$$\begin{aligned} r_{(i)}^2 &>> \left(J_{2i} + H_{ij}\ddot{x}_j\right) \\ r_{(i)}^2 &>> B_{2ij} \\ r_{(i)}^2 &>> h_{ijk}\,\dot{x}_j\,\dot{x}_k \end{aligned} \qquad (5)$$

then equation 4 becomes the decoupled and linear system of equation 6.

$$J_{1ij}\ddot{x}_j + B_{1ij}\dot{x}_j = \frac{1}{r_{(i)}}\tau_i \qquad (6)$$

It is noteworthy that the conditions of equation 5, when valid for some nominal motion, become less valid as the joint rates, $\dot{x}_p$ increase. Although the values of J_{2i} ,H_{ij} ,B_{2ij} ,h_{ijk} are not exactly known for the S-800, the experimental data obtained during typical maneuvers indicate that the assumptions of equation 5 are indeed valid.

2.2.2 System Identification

As mentioned in the introduction to Section 2.2, the linearizing assumptions described in the above section may not be valid for fast robotic maneuvers. In these situations, the full nonlinear equations of motion must be used for successful trajectory planning and control. Forming the nonlinear equations requires the knowledge of the quantities in H_{ij} ,h_{ijk} ,G_i. In this section, a nonlinear system identification technique is described for determining these unknown parameters. This technique is called the Backward Propagation Technique (BPT).

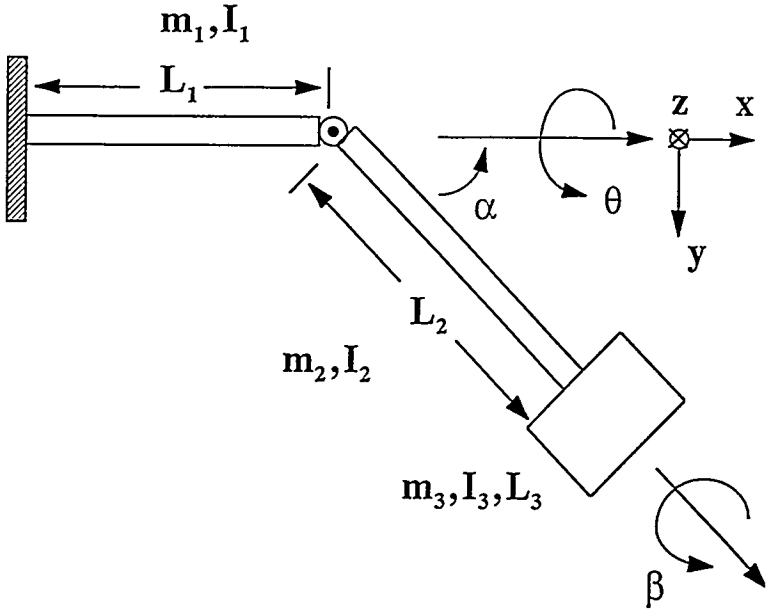

Figure 2 Three Degree of Freedom Model

The BPT approach begins with the outermost joint and works inboard (or backward) a joint at a time until the robot is completely identified. To illustrate this process, a three joint model of a robot (representing the last three joints of the Fanuc S-800) is identified with BPT. Figure 2 shows the kinematic and dynamic structure of the three degree of freedom robot model. The equations of motion as derived with Lagrange's equations are

$$\begin{bmatrix} M_{11} & 0 & M_{13} \\ 0 & M_{22} & 0 \\ M_{31} & 0 & M_{33} \end{bmatrix} \begin{bmatrix} \ddot{\theta} \\ \ddot{\alpha} \\ \ddot{\beta} \end{bmatrix} + \begin{bmatrix} c_{11} & 0 & 0 \\ 0 & c_{22} & 0 \\ 0 & 0 & c_{33} \end{bmatrix} \begin{bmatrix} \dot{\theta} \\ \dot{\alpha} \\ \dot{\beta} \end{bmatrix} + \begin{bmatrix} k_{11} & 0 & 0 \\ 0 & k_{22} & 0 \\ 0 & 0 & k_{33} \end{bmatrix} \begin{bmatrix} \theta \\ \alpha \\ \beta \end{bmatrix} +$$

$$\begin{bmatrix} -D_1 (\sin\alpha)^2 \\ 0 \\ -I_{x3} \sin\alpha \end{bmatrix} \dot{\theta}\dot{\alpha} + \begin{bmatrix} 0 \\ I_{x3} \sin\alpha \\ 0 \end{bmatrix} \dot{\theta}\dot{\beta} + \begin{bmatrix} -I_{x3} \sin\alpha \\ 0 \\ 0 \end{bmatrix} \dot{\beta}\dot{\alpha} + \begin{bmatrix} 0 \\ 0.5 D_1 (\sin\alpha)^2 \\ 0 \end{bmatrix} \dot{\theta}^2 = \begin{bmatrix} 0 \\ 0 \\ 0 \end{bmatrix} \tag{7}$$

where

$$M_{33} = I_{x3}$$

$$M_{31} = M_{13} = I_{x3} \cos\alpha$$

$$M_{22} = I_{y2} + I_{y3} + 0.25 m_2 L_2^2 + m_3 (L_2 + 0.5 L_3)^2$$

$$M_{11} = I_{x1} + (I_{x2} + M_{33}) (\cos\alpha)^2 + M_{22} (\sin\alpha)^2$$

$$D_1 = I_{x2} + M_{33} - M_{22} .$$

The first step in the BPT process is to analyze the equations of motion and identify the appropriate robot configurations that are necessary to isolate each joint and associated model parameters. The typical second order system parameters are identified by performing Single-Input-Single-Output (SISO) maneuvers (typically, step command and/or sine sweep) with two different known payloads on each joint with the other joints held at zero degrees. The SISO maneuver on the third (outer most) joint provides the values of M_{33}, c_{33} and k_{33}. The SISO maneuver on the second joint provides the values of M_{22}, c_{22}, and k_{22}. Next, the first joint is configured at $\alpha = 0$ and $\alpha = \pi / 2$ for a set of SISO maneuvers to obtain I_{x1}, I_{x2}, c_{11} and k_{11}. As a result M_{11}, M_{13}, M_{31}, and D_1 are calculated from the previously identified parameters and a fully coupled, nonlinear model is created from a series of SISO system identification procedures.

Whether performing the linear system identification of equation 6 or the nonlinear BPT of equation 7, various transfer functions must be fit to experimental data

relating input joint angle commands to the joint angle response. In brief, the method employed for obtaining transfer functions may be stated as a four step procedure:

1. Obtain experimental joint response data for a known input joint angle command profile.
2. Postulate a transfer function relating input joint angle commands to output joint angle response, where the transfer function is parameterized using several unknown quantities.
3. Define a cost function reflecting the amount of error between the experimental joint angle response data and the output of the transfer function for a known input.
4. Using a numerical optimization code, find values for the initially unknown parameters of the transfer function which minimize the cost function.

Several types of input joint angle commands were examined in an effort to determine the best type of input/output data sets for generating accurate joint angle transfer functions. The results indicated that a simple step input yielded the most reliable estimation of input/output transfer functions.

The postulated transfer function was based on the form of equation 6, with a Proportional-Derivative (PD) controller connected in series. A block diagram representing the postulated system is shown in Figure 3, where θ_{in} is the input joint angle command; θ_{out} is the joint angle response; θ_e is joint angle error; K_p, K_d are the proportional and derivative gains of the PD controller; K, D_0 are parameters of the joint angle dynamics; and s is the Laplace transform variable. The unknown parameters being estimated include K_p, K_d, K, D_0. The net transfer function relating joint angle input commands to joint angle response is

$$\frac{\theta_{out}}{\theta_{in}} = \frac{K(K_d s + K_p)}{s^2 + (D_o + KK_d)s + KK_p} \tag{8}$$

The cost function used for the optimization procedure is the integrated weighted squared error between the measured joint angle response and the predicted joint angle response based on the transfer function of equation 8, for several sets of data. The cost function is given by

$$J = \sum_{i=1}^{n} W_i \int_{t_o}^{t_f} \left(\theta_m - \theta_a\right)_i^2 dt \tag{9}$$

where n is the number of data sets used, W_i are weighting constants, t_0 is the start time of the maneuver, t_f is the final time of the maneuver, θ_m is the experimentally measured joint angle, and θ_a is the analytically determined joint angle response. The primary feature of this cost function is that as the *predicted* angle response approaches the *measured* angle response, the cost function tends to zero.

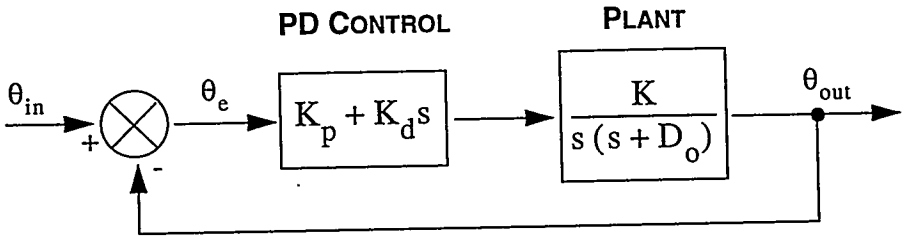

Figure 3 Block Diagram of Postulated Input/Output System for Determining the Input/Output Transfer Function

The optimization code is taken directly from MATLAB's optimization toolbox via the "constr" function. This code implements a quadratic programming technique for finding the values of K_p, K_d, K, D_0 that minimize the cost function of equation 9.

In Section 3.3, the specific details of using this procedure for estimating a transfer function from experimental data is described. The block diagram of Figure 3 is modified based on the observation of a nonlinear limiting behavior of the input commands for large angular rate commands.

3.0 CONTROLLED MOTION OF LIQUID

The following subsections describe three methods of controlling the motion of the liquid. In these subsections, it is assumed that the fundamental mode of oscillation of the liquid is known using the model in Section 2.1. It is also assumed that the robot dynamics are negligible, and the robot accurately tracks the prescribed profile. When the robot dynamics are *not* negligible, the robot's transfer function can be used to alter the nominal profile so that the desired motion can be achieved.

3.1 Optimization Technique

In this section, the motion of the container is restricted to simply translating the liquid along a horizontal path on a straight line. The end effector trajectories are generated using a second order linear model of the liquid's sloshing motion. The acceleration profile of the end effector is postulated as being of a bang-coast-bang form, as shown in Figure 4. A numerical nonlinear optimization routine is used to find the parameters of the acceleration profile, in conjunction with the slosh model, resulting in *near* slosh free motion of the payload. There is an initial and final movement of the liquid within the container associated with the acceleration and deceleration of the container, but no residual sloshing when the motion is complete.

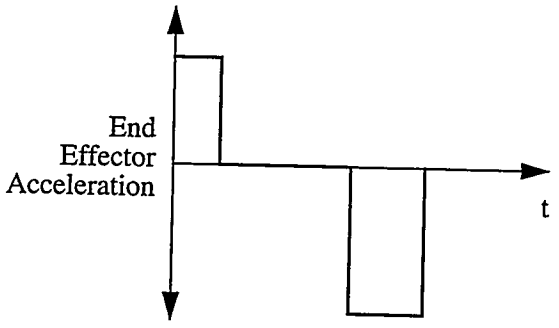

Figure 4 Postulated End-Effector Acceleration Profile for Slosh-Free Motion.

The model of the slosh is that of a simple harmonic oscillator

$$\ddot{\theta} + 2\zeta\omega_n\dot{\theta} + \omega_n^2\theta = \ddot{x} \tag{10}$$

where θ is the slosh displacement, ζ is the damping ratio, ω_n is the slosh natural frequency, and x is the translation of the container along the horizontal axis.

Near slosh-free end effector motion is determined by numerically solving for the end-effector acceleration profile parameters such that at the end of the maneuver $\theta = 0$, $\dot{\theta} = 0$, $x(t_f) = 1.4m$, and $t_f = 2.0s$. The simulated slosh response is shown in Figure 5, where the container trajectory is expressed in meters. The slosh displacement, however, is in units of scaled meters. Container accelerations are maintained below $0.25g$ in an effort to keep slosh displacements low during the maneuver. Although the maneuver time was chosen as 2.0s, the container distance and slosh requirements can be achieved using lesser or greater maneuver times if desired.

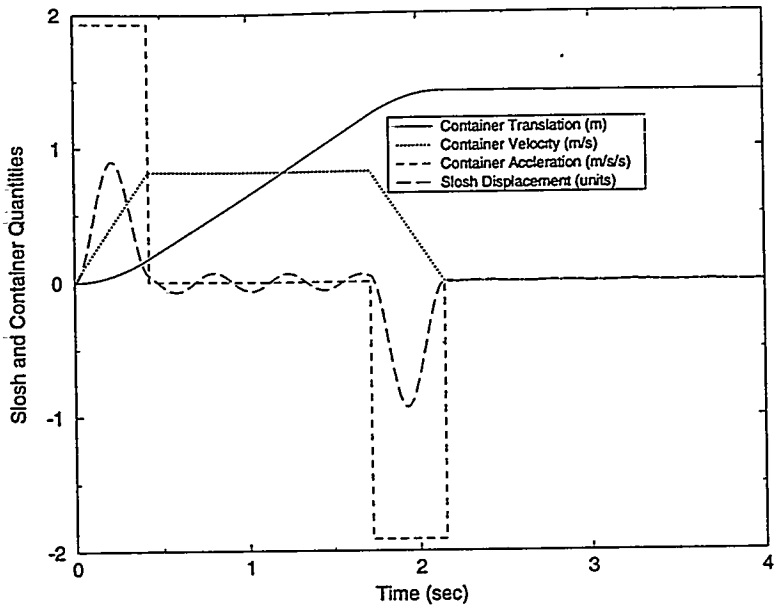

Figure 5 Slosh and Container Trajectories for $\omega_n = 14.45$ rad / s and $\zeta = 0.0172$.

3.2 Infinite Impulse Response Filtering

In this section, the container is again restricted to travel along a straight-line horizontal path, except now the motion profile is not restricted to a bang-coast-bang acceleration/deceleration. Instead, an infinite impulse response (IIR) filter is used to pre-shape the input of an underdamped second order system so that the overall system becomes a critically damped third order plant. The IIR filter is implemented via the following difference equation (Feddema, 1993):

$$\begin{aligned} y(k) &= -a_1 y(k-1) - a_2 y(k-2) - a_3 y(k-3) + b_0 u(k) \\ &+ b_1 u(k-1) + b_2 u(k-2) + b_3 u(k-3) + b_4 u(k-4) \end{aligned} \tag{11}$$

where $y(k)$ is the output of the filter and $u(k)$ is the input to the filter (acceleration in horizontal direction $\ddot{x}$) at discrete time k. The IIR filter coefficients a_i and b_i are a

function of the natural frequency ω_n, damping ratio ζ, a scaling factor, and the sampling period T. The scaling factor is used to shorten the settling time of the shaping filter. The larger the value, the shorter the settling time of the filter. However, a shorter settling time means the filter may try to drive the system faster than capable. Typically, the scaling factor is chosen so that the settling time is approximately equal to one half the period of oscillation.

Figure 6 shows the acceleration profile along the x axis before and after filtering. Notice that the filter delays the profile. The natural frequency and damping ratio used in the figure are the values determined in the Section 4.2. Figure 7 shows the estimated angle before and after filtering. As seen in the figure, this method eliminates residual oscillation at the end of the motion. Experimental results very closely match the modeled response and can be found in Appendix G [Feddema *et. al.*].

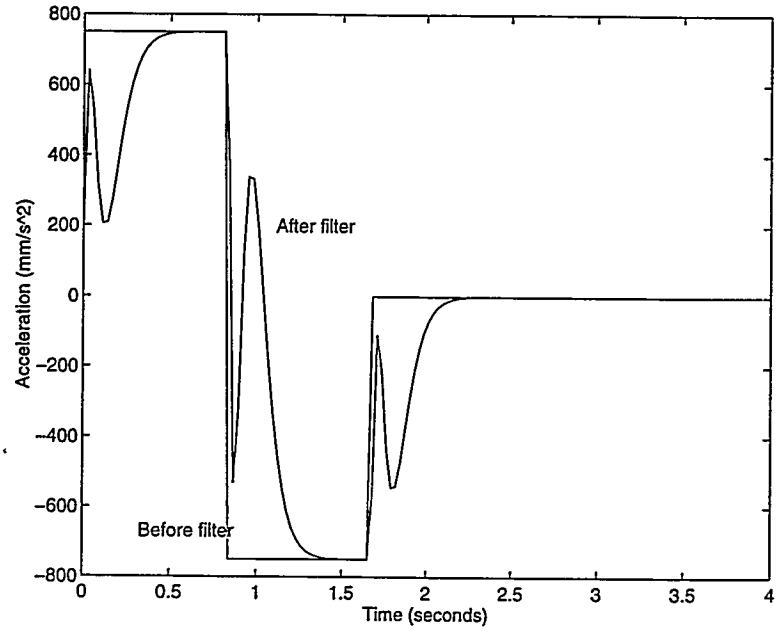

Figure 6 Acceleration Profiles Before and After Filtering

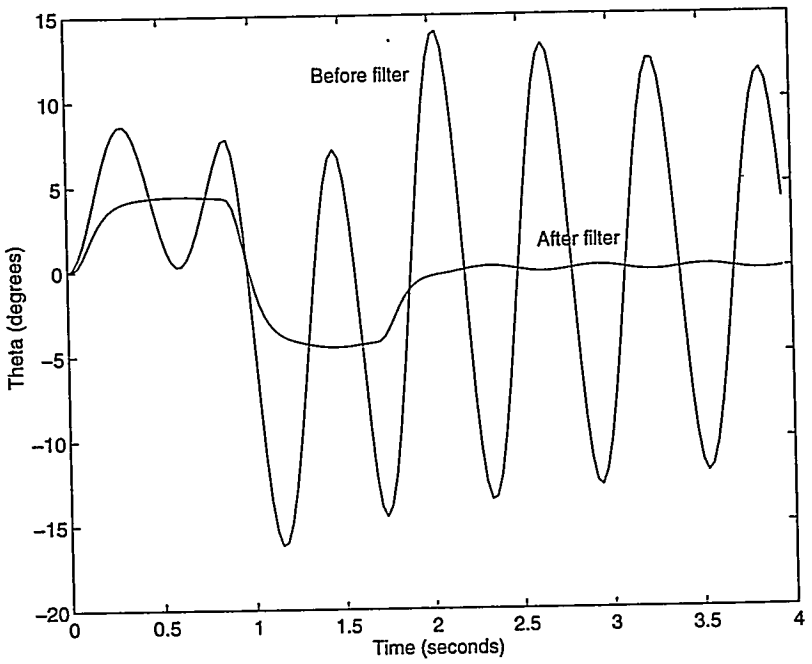

Figure 7 The Predicted Angle of the Fluid Relative to the Container.

3.3 Slosh-Free Control

Some applications may require that the liquid not move relative to the container. For Corning, it may be desirable to keep the molten glass from moving up the sides of the container wall where a thin film will form. In order to do this, the robot must be able to rotate about an axis that is orthogonal to the plane of translation.

Similar to the previous subsection, a simplified model assumes that the liquid surface remains flat during the robotic maneuvers and, therefore, can be modeled as an oscillating pendulum. Adding the rotation of the container, the liquid and container can be modeled by a double pendulum with a moving base as shown in Figure 8. The symbol m is the mass of the liquid, r_m is the length of the equivalent pendulum, r_L is the distance from the center of rotation of the robot to the center of rotation of the pendulum, x is the translational position of the center of rotation of the robot, and θ and β are the angle of rotation of the pendulum and the robot, respectively.

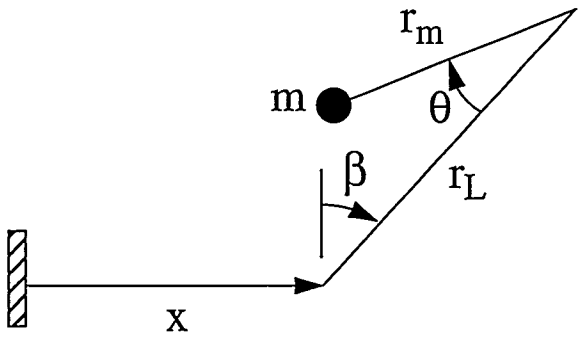

Figure 8 Double Pendulum Model of a Fluid in a Spherical Container

The governing equation of motion for the model is given by

$$\frac{d^2\theta}{dt^2}+\left(1-\frac{r_L}{r_m}\cos\theta\right)\frac{d^2\beta}{dt^2}+\frac{g}{r_m}\sin(\theta+\beta)-\frac{r_L}{r_m}\dot{\beta}^2\sin\theta-\frac{d^2x}{dt^2}\cos(\theta+\beta)/r_m+\frac{c_m}{mr_m^2}\dot{\theta}=0 \quad (12)$$

where g is the acceleration of gravity, c_m is the damping coefficient, and m is the mass of the fluid. Setting β, $\dot{\beta}$, and the second derivatives of x and β, equal to zero in equation 12 yields

$$\frac{d^2\theta}{dt^2}+2\varsigma\omega_n\dot{\theta}+\omega_n^2\sin\theta=0 \quad (13)$$

where

$$\omega_n^2=\frac{g}{r_m} \quad (14)$$

and

$$\zeta=\frac{c_m}{2mr_m^2\omega_n} \quad (15)$$

For small values of θ, equation 13 simplifies to that of a linear, damped, harmonic oscillator. Estimates for ω_n and ζ can be determined experimentally from small-angle, free vibration data using standard techniques.

The goal of slosh-free motion is to have no relative motion between the container and the fluid. With reference to Figure 8, achieving this goal is equivalent to keeping the angle θ, equal to zero at all times. Setting θ, and its time derivatives equal to zero in equation 12, one obtains the following constraint equation:

$$\frac{d^2\beta}{dt^2} + \omega_0^2 \sin\beta = \left(\omega_o^2 / g\right)\frac{d^2x}{dt^2}\cos\beta \tag{16}$$

where

$$\omega_0^2 = \frac{\omega_n^2}{1 - r_L / r_m} \tag{17}$$

Slosh-free motion is accomplished by controlling the angle β so that equation 16 is satisfied. Of particular interest to this study are constant acceleration maneuvers in which

$$\frac{d^2x}{dt^2} = \varepsilon g \tag{18}$$

where the magnitude of the scalar constant ε is typically less than unity.

The analytical solution to equation 16 developed below is based on a modification of a perturbation procedure presented in Lichtenberg (Lichtenberg,. *et al*) . The basic approach is to expand β in ascending powers of ε as

$$\beta(t,\varepsilon) = \varepsilon\beta_0(\omega t) + \varepsilon^3\beta_2(\omega t) + \varepsilon^5\beta_4(\omega t) + \ldots \tag{19}$$

where ω is expanded in ascending powers of ε as

$$\omega = \omega_0 + \varepsilon^2\omega_2 + \varepsilon^4\omega_4 + \ldots \tag{20}$$

Substituting equations 18-20 into equation 16, equating coefficients of like powers of ε , and solving the resulting differential equations such that there are no secular terms and the initial conditions $\beta(0) = 0$ and $\dot{\beta}(0) = 0$ are satisfied yields

$$\beta(t,\varepsilon) = \varepsilon(1-\cos\omega t) + \frac{\varepsilon^3}{192}(-64+63\cos\omega t+\cos 3\omega t) + \frac{\varepsilon^5}{61440}(12288-11985\cos\omega t-300\cos 3\omega t-3\cos 5\omega t)+\ldots \quad (21)$$

where

$$\omega = \left(1+3\varepsilon^2/16-69\varepsilon^4/1024+\ldots\right)\omega_0 \quad (22)$$

The wrist translation acceleration profile used for slosh-free maneuvers is shown in Figure 9. With this acceleration profile, a wrist initially at rest will be at rest for $t \geq T$ having traversed a distance of $\varepsilon g\left(t_1^2 + t_1 t_2\right)$. During the coast portion of the maneuver $\left(t_1 \leq t_1 + t_2\right)$, the angle β is set equal to zero. Consequently, for the motion to be slosh-free over this time interval both $\beta(t_1)$ and $\dot{\beta}(t_1)$ must equal zero. These conditions are satisfied by equation 21 if

$$t_1 = \frac{2\pi n}{\omega} \quad (23)$$

where n is an integer.

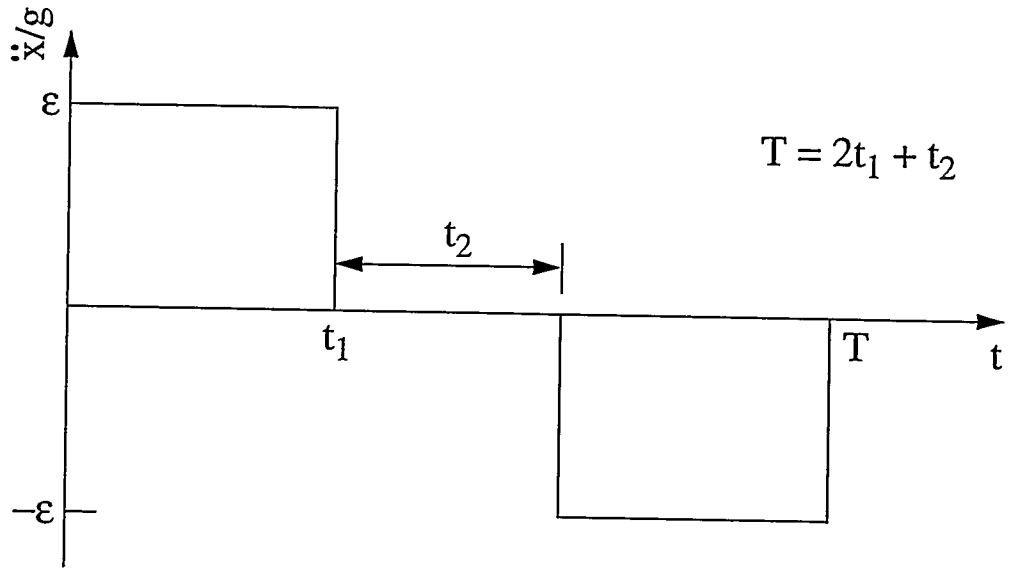

Figure 9 Wrist Translation Acceleration Profile for a Slosh-Free Maneuver

A sample problem is used to demonstrate the use of equations 21-23 for slosh-free maneuvers. In the sample $T=1$, $\omega_n = 2.3(2\pi)$, $\zeta = 0.1$, $r_L / r_m = 1/2$ and $n=1$. Acceleration profiles corresponding to $\varepsilon = 1/4$ and $\varepsilon = 1/2$ are considered.

Using the parameter values given above, ω is determined from equation 11. equation 21 is then used to determine $\beta(t)$ during the time intervals $0 \le t \le t_1$ and $t_1 + t_2 \le t \le T$. The function $\theta(t)$ is obtained from numerical integration of equation 12 using the known acceleration profile and the calculated $\beta(t)$.

Time histories of β for $\varepsilon = 1/4$ and $\varepsilon = 1/2$ are shown in Figures 10 and 11 respectively. The corresponding time histories of θ are shown in Figures 12 and 13. Ideally, $\theta(t)$ would equal zero for all times. This is not the case, however, because the analytical solution to equation 16 is only approximate. Nevertheless, it is clear from Figs. 12 and 13 that the analytical solution is quite effective in limiting the magnitude of θ to small values (*i.e.* 10^{-5} and 10^{-3} radians) for the acceleration profiles considered. Experimental results of this approach can be found in Appendix G.

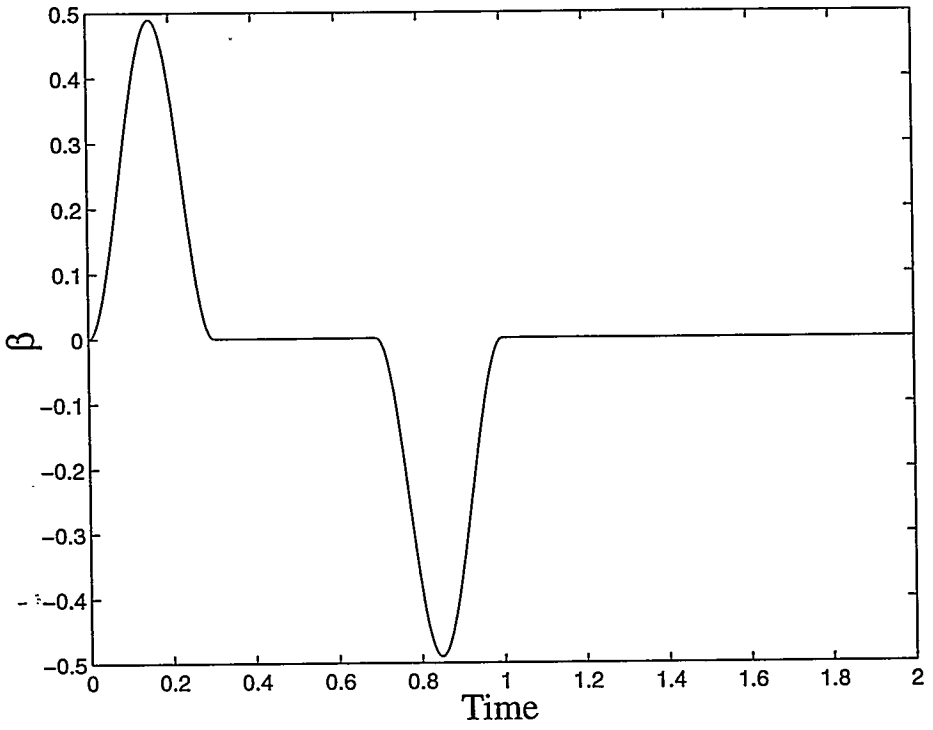

Figure 10 Time history of β for $\varepsilon = 1/4$

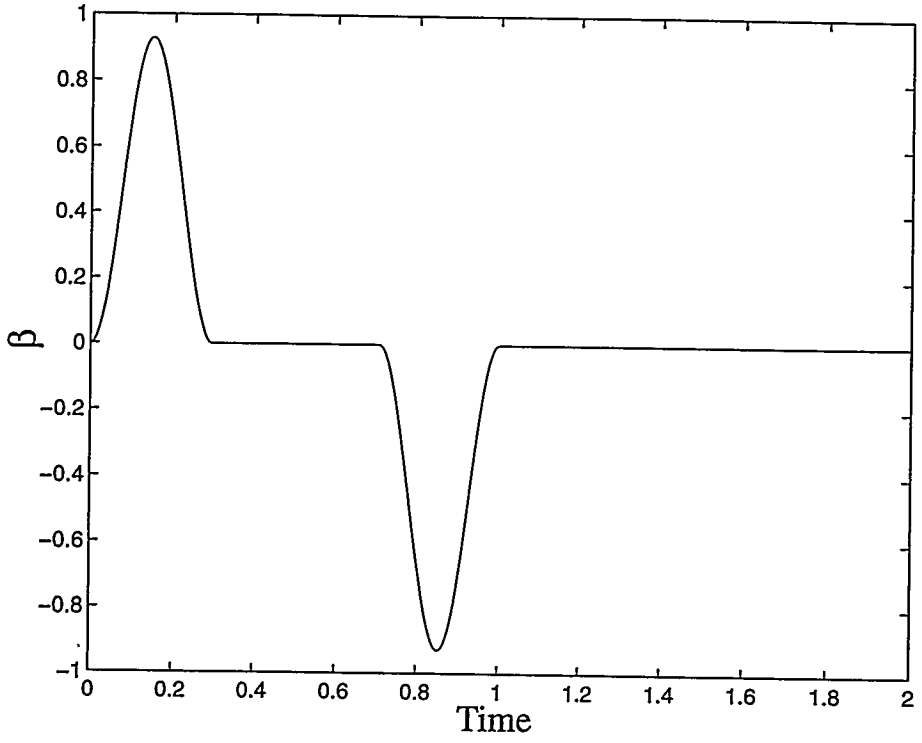

Figure 11 Time history of β for $\varepsilon = 1/2$

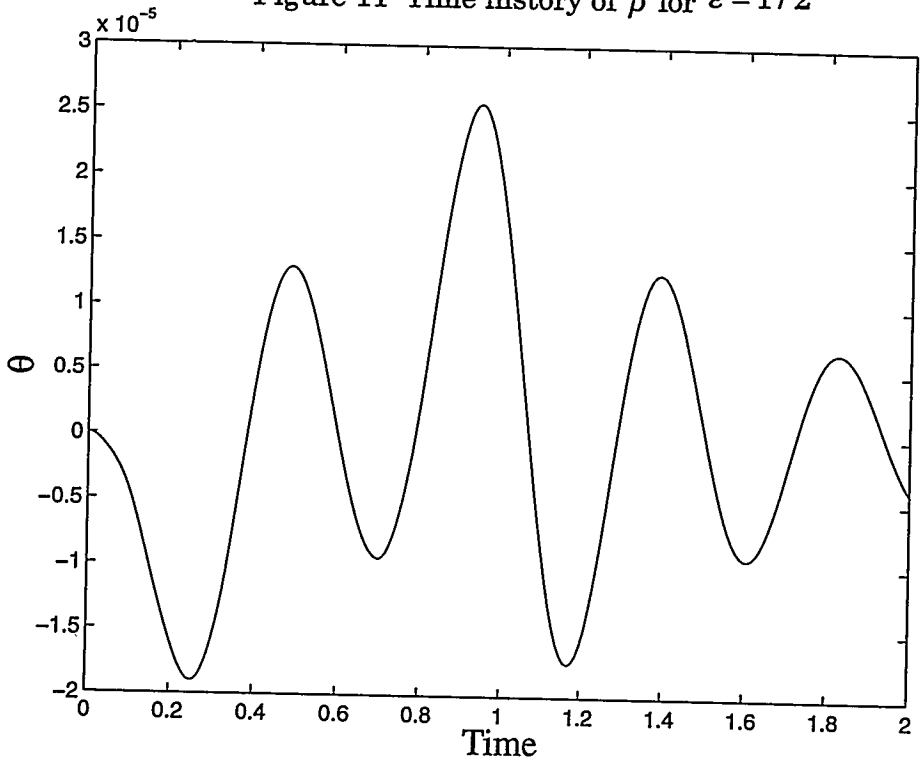

Figure 12 Time history of θ for $\varepsilon = 1/4$

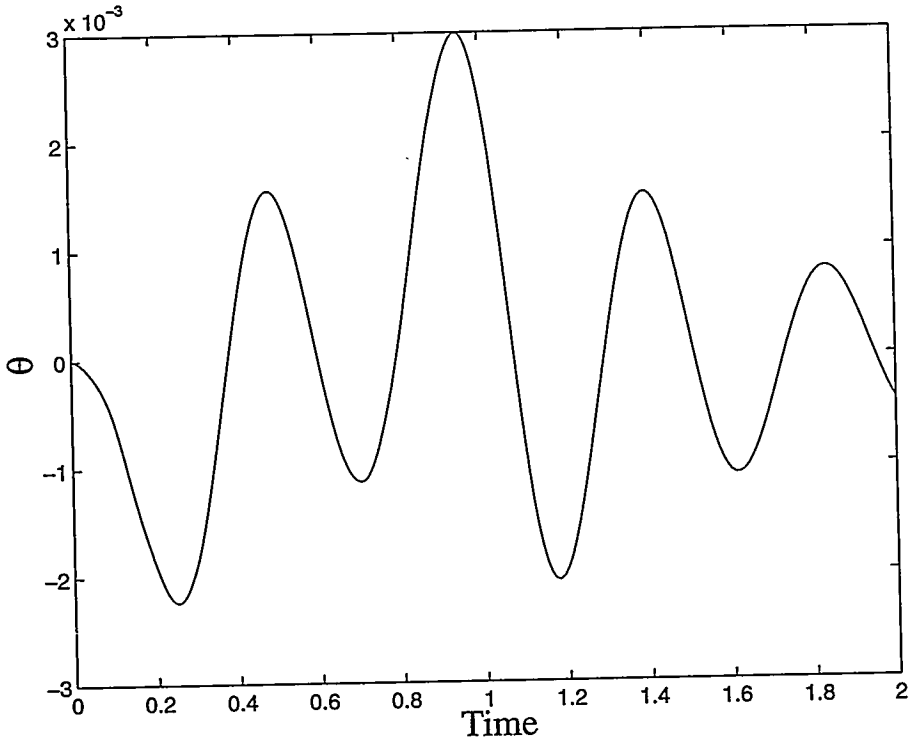

Figure 13 Time history of θ for $\varepsilon = 1/2$

4.0 EXPERIMENTAL RESULTS

The following subsections describe the experimental process used to verify the fluid and robot models. Details on experimental results of the control approaches are found in Appendix G.

4.1 Experimental Setup

Sandia National Laboratories has previously developed a unique capacitive sensing technology for non-contact sensing of objects. A liquid oscillation detection sensor based on this technology has been constructed to measure the oscillation of liquids in various shaped containers. The sensor is attached to the outside of a non-conductive container and can measure the movement of the liquid's surface relative to the container. Figure 14 shows a diagram of the sensor.

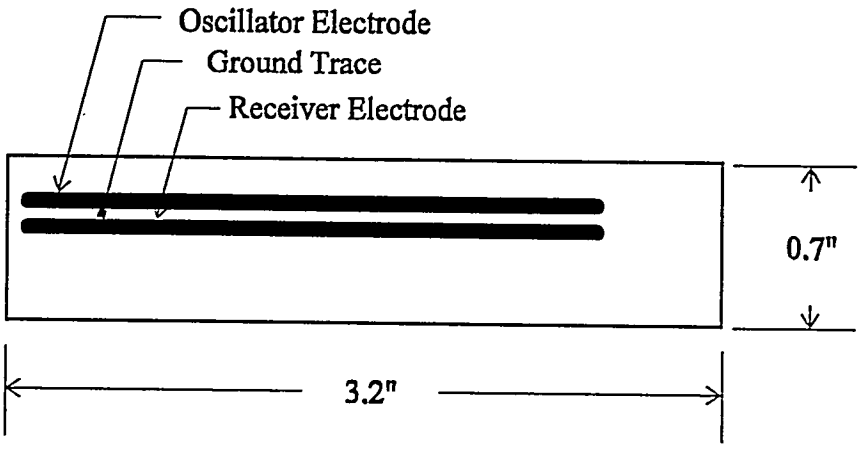

Figure 14 Liquid Oscillation Detection Sensor

The liquid oscillation detection sensor is fabricated from a flexible circuit board material and measures 3.2 by 0.7 inches. This size was specifically chosen for this application to conform to the container size and liquid oscillation levels expected. However, the sensors can be fabricated in many different shapes and sizes to fit a particular application. The sensor face consists of an oscillator electrode and a receiver electrode separated by a grounded trace. The arrangement of these electrodes creates an electric field that extends from the sensor surface in an approximately half-cylindrical shape. Figure 15 depicts the measurement setup with the sensor attached to the side of a typical container. The circular lines represent the electric fields which extend through the container walls and into the liquid. Sensor output is proportional to the volume of the electric field which is occupied by the liquid. These perturbations in the electric field are detected as

capacitance variations between the oscillator and receiver electrodes, and are converted to voltage changes by the signal conditioning system.

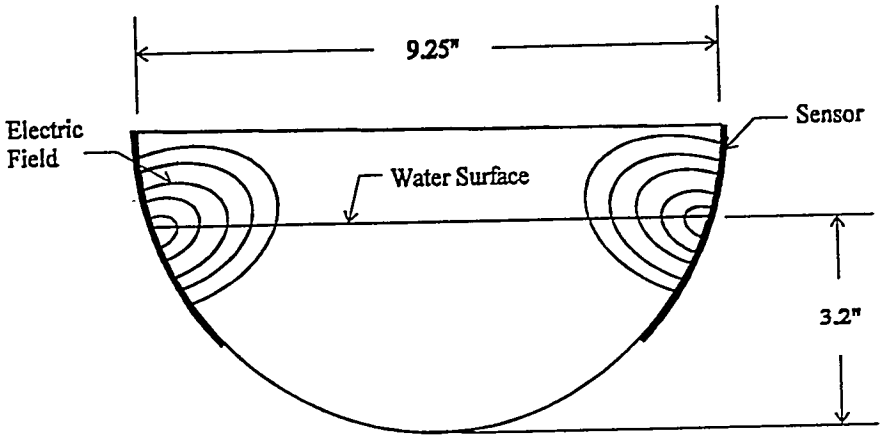

Figure 15 Hemispherical Container Instrumented for Liquid Oscillation Detection

The signal conditioning system is located remotely from the instrumented container. This circuitry provides the driving signals for multiple liquid oscillation detection sensors and processes the return signals to provide analog outputs to the data acquisition system. An oscillator board generates the driving frequencies and reference signals for each of the individual sensors. To avoid coupling between multiple sensors, distinct frequencies in the 100 KHz range are used to drive each sensor. Another circuit board contains synchronous detection circuitry to measure the amplitude of the return signal from each sensor. Because each sensor is driven with a unique frequency, each channel of this circuitry detects the signal of only one sensor, thereby rejecting any noise or signals from other sensors. The detection circuitry generates an extremely low noise signal output, which is amplified to provide a high-level (±10V) signal to the data acquisition system. The output signal level corresponds to position of the liquid surface with respect to the container.

4.2 Fluid Model Verification

The oscillation of water in two different shaped containers was measured utilizing the liquid oscillation detection sensor. The first container was trapezoidal in shape (Figure 16) and the second container was hemispherical in shape (Figure 15). The sensors were placed at equal spacing around the circumference of the containers. Motion trajectories were implemented which caused the water to oscillate in the container such that the maximum amplitude of the water's surface would be sensed by a pair of sensors 180 degrees apart.

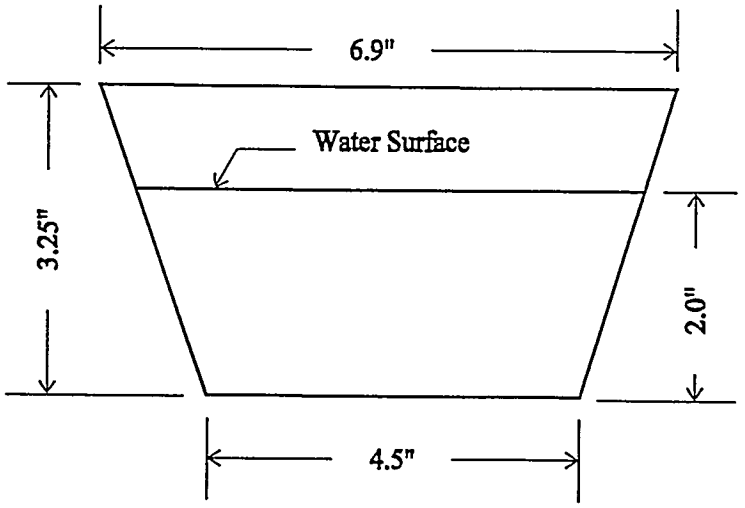

Figure 16 Trapezoidal Container

The trapezoidal shaped container was instrumented with four liquid oscillation detection sensors equally spaced at 90 degrees around the circumference of the container. Sensors 1 and 3 were positioned to measure the maximum amplitude of water oscillations. The container was filled to a depth of 2.0 inches. The water was caused to oscillate in the container with an input motion profile which smoothly accelerated to a constant velocity of 150 mm/sec for a total displacement of 250 mm. The sensors were each sampled at 28 milliseconds for a total time of 12.6 seconds (450 samples). Figures 17 through 20 show the output for each of the four sensors. Note from Figures 17 and 19 that the output of sensors 1 and 3 are saturated for the first few oscillations of the water's surface.

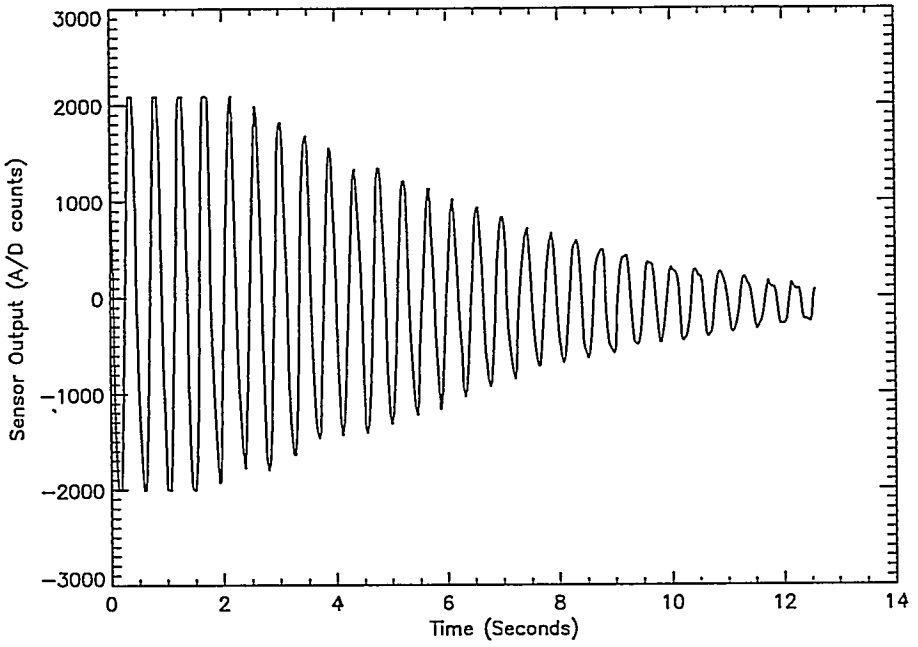

Figure 17 Measured Oscillation of Water in a Trapezoidal Shaped Container, Sensor 1.

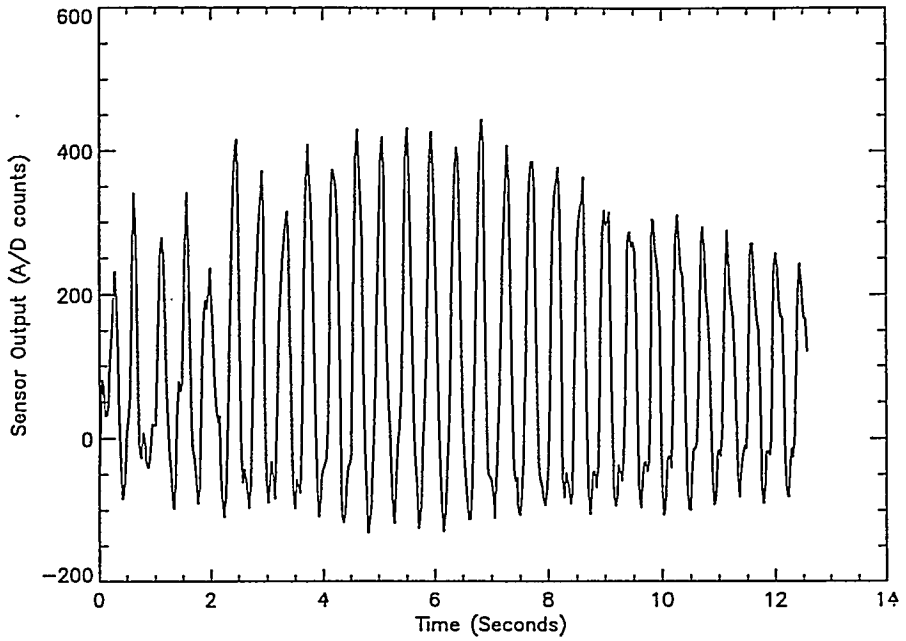

Figure 18 Measured Oscillation Of Water In A Trapezoidal Shaped Container, Sensor 2.

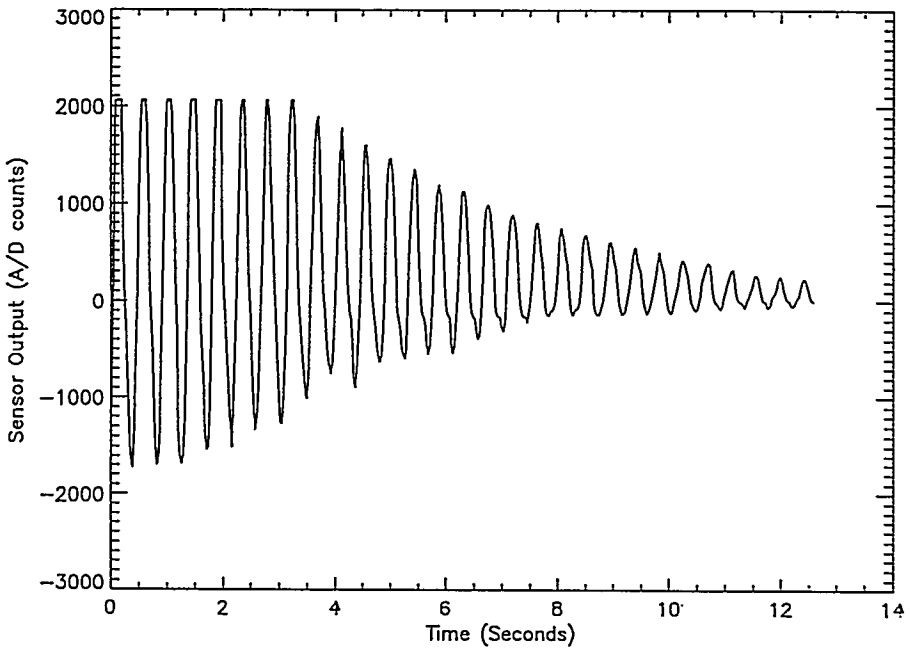

Figure 19 Measured Oscillation Of Water in a Trapezoidal Shaped Container, Sensor 3

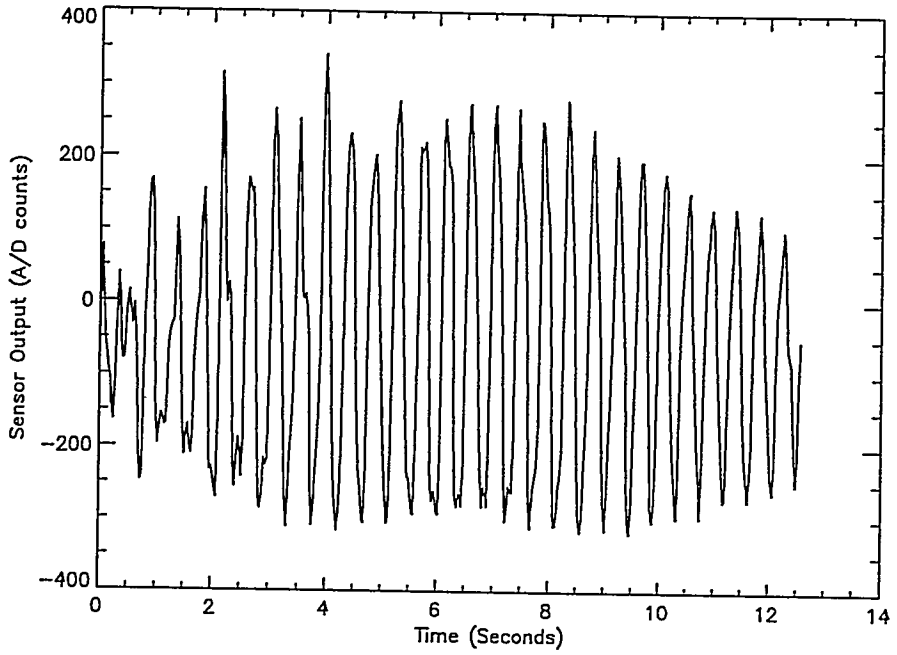

Figure 20 Measured oscillation of water in a trapezoidal shaped container, Sensor 4

Estimates of the natural frequency and damping ratio were made by performing a peak-to-peak analysis of sensor 1 output as shown in Figure 5. The natural frequency and damping ratio were calculated for 20 successive peaks, starting with the first peak amplitude which was not saturated. The following formulas were used to calculate these parameter

$$f_n = \frac{n-1}{t_n - t_1}$$

$$\zeta = \frac{1n\left(\frac{x_1}{x_n}\right)}{2\pi(n-1)} \qquad (24)$$

f_n = Natural Frequency, Hz
ζ = Damping ratio
x_1 = Magnitude at positive peak 1, A/D counts
t_1 = Time at positive peak 1, sec
x_n = Magnitude at positive peak n, A/D counts
t_n = Time at positive peak n, sec
n = Peak number

The analysis resulted in an average natural frequency of 2.30 Hz (standard deviation = 0.144 Hz) and an average damping ration of 0.0172 (standard deviation = 0.0074) over the 20 peaks.

The hemispherical shaped container was instrumented with two liquid oscillation detection sensors equally spaced at 180 degrees around the circumference of the container. These sensors (sensors 1 and 2) were positioned to measure the maximum amplitude of water oscillations. The container was filled to a depth of 3.2 inches.

Sensor calibration data was collected to provide a conversion to meaningful units with respect to the hemispherical container. Calibration data was collected by initially rotating the container +15 degrees so that the water's surface was near the lip of the container at one edge. The container was slowly rotated from this position through the level position and continued to the -15 degree position. The motion was then reversed from the -15 degree position back to the +15 degree position. Sensor data was recorded at each 0.5 degree increment. The point of rotation was defined to be the center of the sphere.

The data from sensors 1 and 2 is shown in Figure 21. This data shows that the sensors provide useful data over a range of approximately ±6 degrees. For rotations greater than this, the sensors are saturated. A small amount of hysteresis is also present. Previous testing had shown that surface tension between the water surface and the container surface accounts for the hysteresis. The surface of the container was treated with Rain-X to minimize this effect. As the response of the sensor is fairly linear with angular tilt, a linear calibration factor can be used for converting sensor readings to angular positions. This calibration factor is 407 counts/deg for Sensor 1 and 337 counts/deg for Sensor 2

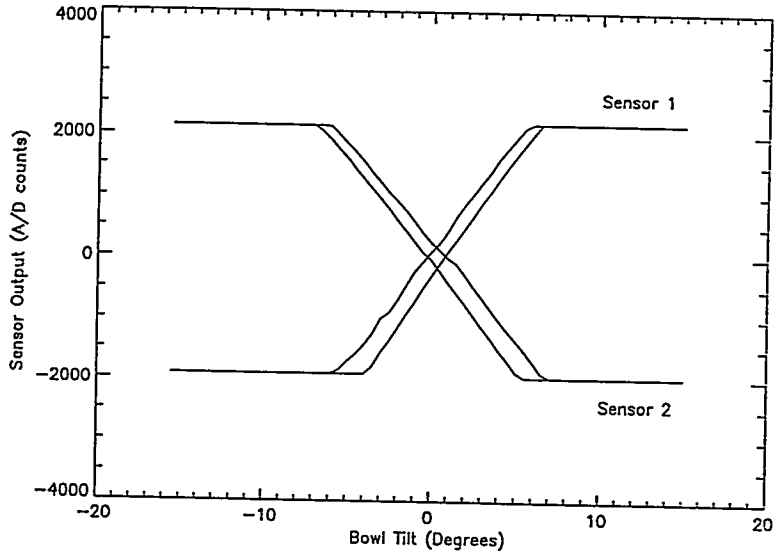

Figure 21 Sensor Calibration Data

The water was caused to oscillate in the hemispherical container by performing a short linear move at a constant height. The container was accelerated with a triangular-shaped acceleration to a constant velocity for a total displacement of 252 mm. Table 1 summarizes three motion trajectories which were implemented, and Figure 23 shows the acceleration profile for the most aggressive of these profiles (252 mm at 150 mm/sec). Data collection was initiated at 1 second before container motion. Each sensor was sampled at 500 Hz for a total time of 30 seconds (15000 samples).

Constant Velocity (mm/sec)	Displacement (mm)	Peak Acceleration (mm/sec^2)	Trajectory Time (sec)
75	252	382.65	3.752
100	252	510.20	2.912
150	252	765.31	2.072

Figure 22 - Table 1: Input Motion Trajectories

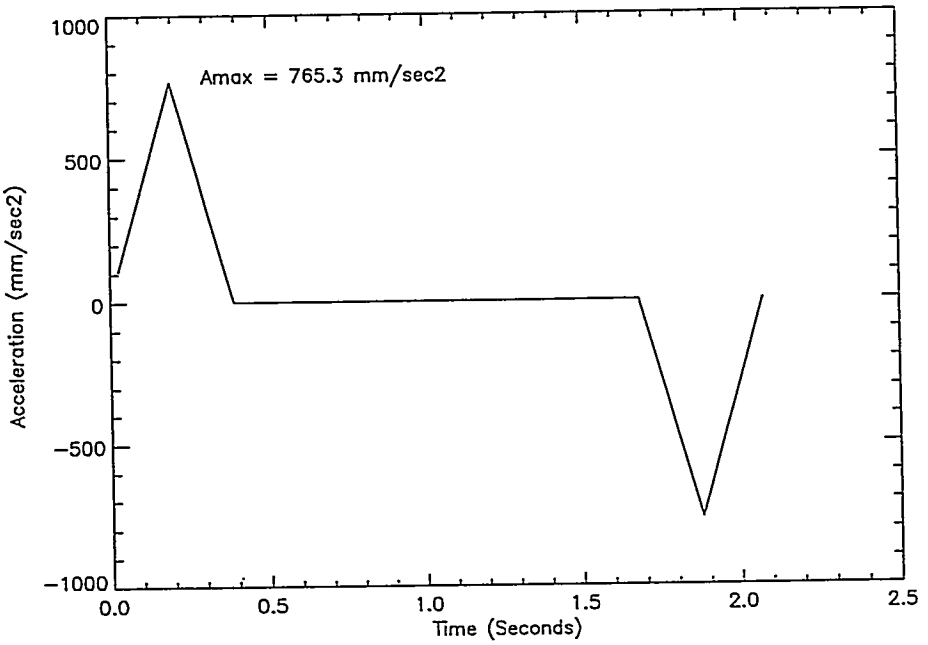

Figure 23 Hemispherical Container Acceleration Profile

Figures 24 and 25 show the output of sensors 1 and 2 during and following container motion for second trajectory shown in Table 1. The linear calibration factors have been applied such that the magnitudes are represented in degrees with respect to the container surface. The initial sensor output of zero (with some noise) occurs before the container is in motion. The initial non-zero sensor response is due to the induced water oscillation during container motion. The remaining sensor response shows the water oscillation once the container has been decelerated to rest.

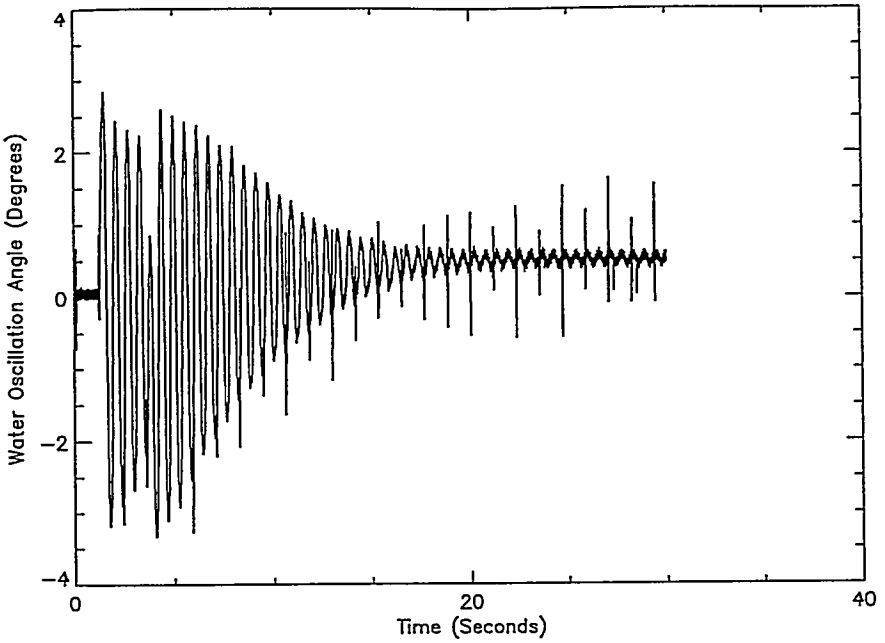

Figure 24 Measured Oscillation of Water in a Hemispherical Shaped Container, 100 mm/sec, Sensor 1

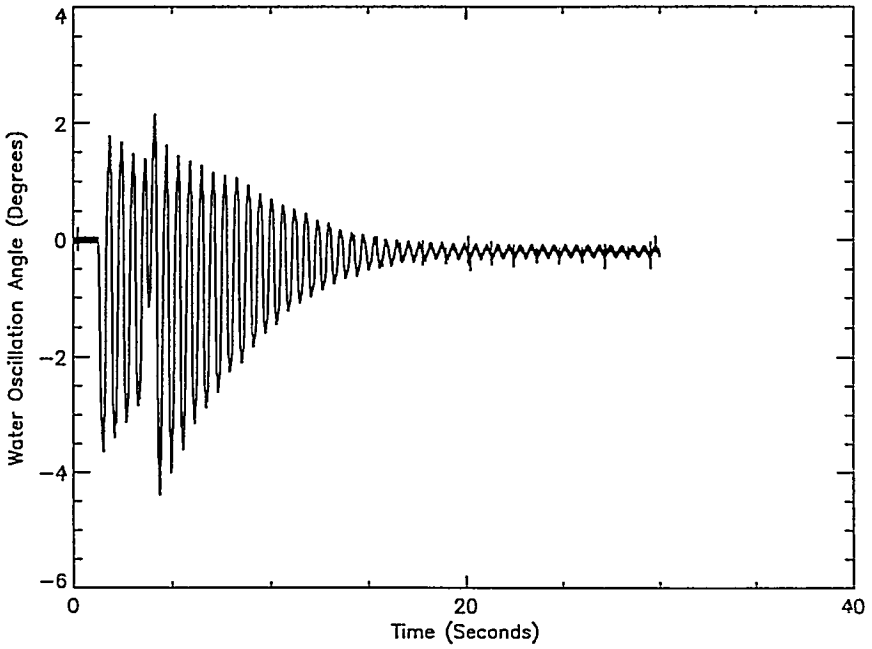

Figure 25 Measured Oscillation of Water in a Hemispherical Shaped Container, 100 mm/sec, Sensor 2

Estimates of the natural frequency and damping ratio were made for water oscillation in the hemispherical container. The estimates were made from the output of sensor channel 1 for the input motion trajectory of 252 mm displacement at 100 mm/sec as shown in Figure 23. The estimate was made by using equation 24 and averaging over the first and tenth oscillation peak after bowl motion had ceased. This analysis resulted in a natural frequency of 1.70 Hz and a damping ratio of 0.0093.

4.3 Robot Model Identification

This last section uses the procedure of Section 2.2.2 to estimate the linear transfer function of joint 1 of the Fanuc S-800 robot. A similar analysis was performed on joints 2 through 6. The next step would have been to perform the nonlinear BPT procedure and use these results to modify the robot's motion profiles to account for robot dynamic effects at higher speeds. Unfortunately, we ran out of time and funding to finish this task. Nevertheless, the following discussion gives a glimpse of how the identification is performed.

Three step response data sets are used to obtain a transfer function for joint 1 of the Fanuc S-800. The step responses are for input angle commands of 1. As mentioned previously, a significant nonlinear effect is observed in the angle response data for

large angle rate commands. These effects are of sufficient magnitude for the maneuver that modeling of the nonlinearity is required. Several nonlinear elements were examined to predict the observed behavior of the experimental data. The best match was obtained when a saturation-like element was inserted between the PD controller and the plant for the analytical model. The block diagram of Figure 3 is modified to reflect this change as shown in Figure 26.

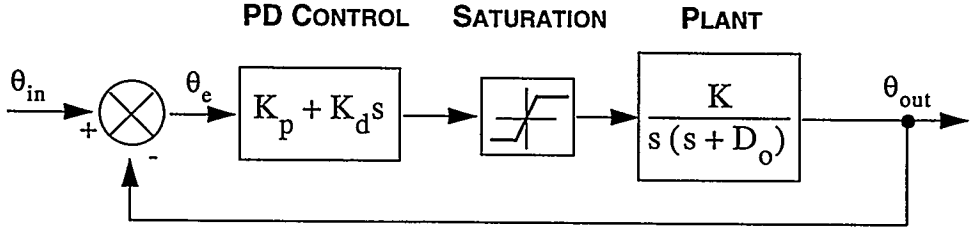

Figure 26 Block Diagram of Postulated Input/Output System for Determining the Input/Output Transfer Function, with Saturation.

Since the exact form of the saturation function is unknown, like the system dynamics, it, too, is parameterized with several quantities. The optimization procedure of Section 2.2.2 is carried out to find not only the values of K_p, K_d, K, D_0, but also the form of the saturation function. The resulting saturation function is shown in Figure 27, while the estimated model parameters are given in Table 2.

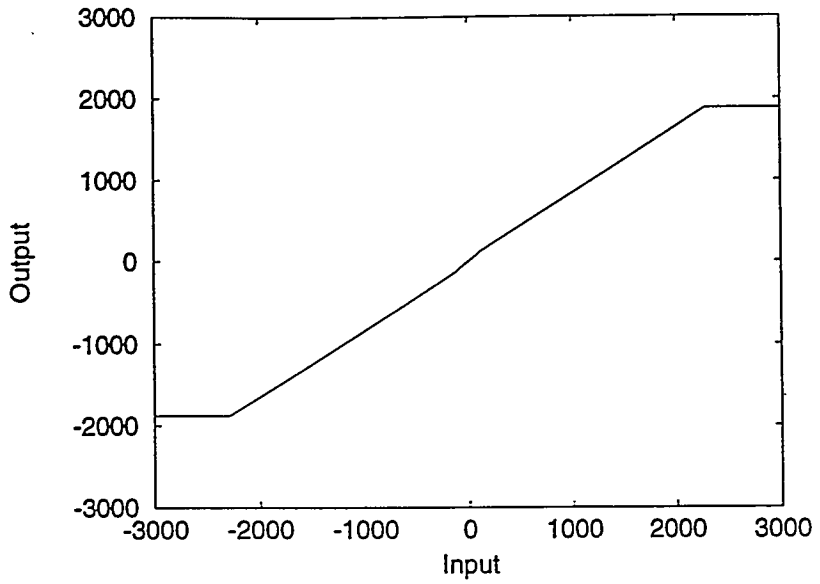

Figure 27 Saturation Function Profile

K_p	K_d	K	D_0
400	7.5	0.5	27.6

Figure 28 - Table 2 Estimated Parameters for Joint 1

Plots of measured joint angle responses along with responses using the estimated analytical model are shown in Figures 29 - 31, for the three data sets considered. The evident agreement between analytical and measured data is indicative of the accurate estimation achieved.

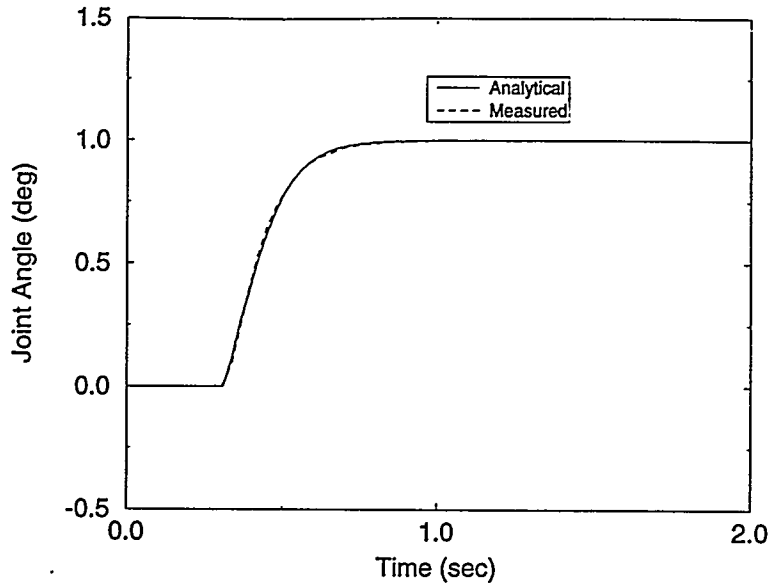

Figure 29 Comparison of Measured and Analytical Joint Angle Responses to a 1° Joint Angle Step Command.

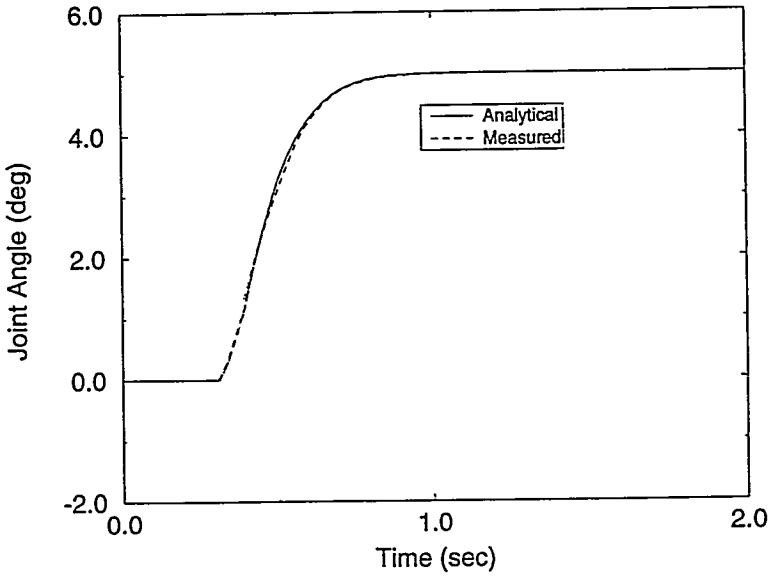

Figure 30 Comparison of Measured and Analytical Joint Angle Responses to a 5° Joint Angle Step Command.

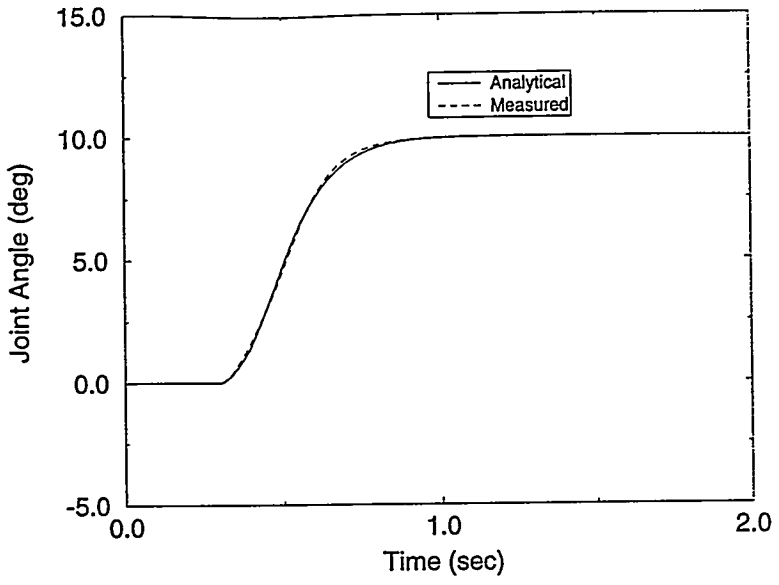

Figure 31 Comparison of Measured and Analytical Joint Angle Responses to a 10° Joint Angle Step Command.

5.0 CONCLUSIONS AND SUGGESTIONS

Through modeling and system identification, inverse dynamic controls, and experimental tests, the Sandia team was able to demonstrate that it is possible to control the motion of the robot to eliminate sloshing of a very low viscosity liquid such as water. Residual surface waves at the end of motion were reduced by over 95 percent, while in-motion surface waves were reduced by over 75 percent. For higher viscosity liquids, the ability of an industrial robot to alter the liquid's surface deformations was less dramatic. Calculations showed that for a 10000 poise liquid with a blob thickness of 5 cm, the blob would shift only 1mm when accelerated at 0.1G for 0.5 seconds. Experimental testing on the Fanuc S-800 robot exhibited immeasurable changes in surface deformations with liquids in the 1000 to 10000 poise range. Therefore, we must conclude that in order for the slosh-free technique to be useful to Corning, either a lower viscosity glass must become available, or a faster mechanism must be used for transport.

References

Feddema, J.T., "Digital Filter Control of Remotely Operated Flexible Robotic Structures," *Proc. 1993 American Control Conference*, San Francisco, California, June 2-4, 1993.

Lichtenberg, A.J. and Lieberman M.A., Regular and Stochastic Motion, *Applied Mathematical Sciences*, Vol. 38, Springer-Verlag, New York, 1983, pp. 66-68.

Appendix A

R.S. Baty

Sloshing Frequencies in Cylindrical Containers

Intentionally Left Blank

Sandia National Laboratories

Albuquerque, New Mexico 87185

date: June 3, 1994

to: R. D. Robinett, 9811, MS0314

Roy Baty

from: R. S. Baty, 1552, MS0833

subject: Sloshing Frequencies in Cylindrical Containers

Introduction

Recently, R. D. Robinett, 9811, requested that Department 1552 provide estimates of the sloshing frequencies in open right cylindrical containers partially filled with liquid. These frequency estimates have application to the development of a robotic control system to move open containers of liquid. The envisioned control system will have the capability to adjust the motion of liquid containers to damp undesirable free-surface motions. This memo outlines simple formulas to estimate the sloshing frequencies of surface waves in right cylindrical containers subject to simple accelerations. The results presented here are valid for linear, inviscid, irrotational surface waves in non-rotating circular cylindrical containers. The surface wave relationships derived in this note can be used to estimate the order of magnitude of free-surface sloshing frequencies in such containers.

Nomenclature

a	$\equiv$	cylindrical container radius.
a_ξ	$\equiv$	body acceleration in the ξ direction.
h	$\equiv$	height of free surface.
f	$\equiv$	Bernoulli constant.
$\overline{F}$	$\equiv$	body force.
g	$\equiv$	gravity constant.
k	$\equiv$	separation constant.
m	$\equiv$	angular mode number.

$\bar{n}$ ≡ normal vector.

p ≡ static pressure.

r ≡ container radial coordinate.

$\bar{r}$ ≡ container position vector.

$\bar{R}$ ≡ position of container origin.

$\bar{u}$ ≡ fluid velocity.

$\bar{V}$ ≡ relative fluid velocity.

z ≡ container vertical coordinate.

η ≡ shape of free-surface.

θ ≡ container angular coordinate.

υ ≡ kinematic viscosity.

ρ ≡ liquid density.

ϕ ≡ velocity potential.

ω ≡ surface wave oscillation frequency.

$\bar{\Omega}$ ≡ container angular velocity.

Theoretical Development

In this section an approximate model is developed to estimate surface wave oscillation frequencies in cylindrical containers subject to simple accelerations. The equations governing fluid mechanics are the Navier-Stokes equations which, in inertial coordinates, may be written:

$$\nabla \bullet \bar{u} = 0, \tag{1}$$

$$\frac{D\bar{u}}{Dt} = \frac{\bar{F}}{\rho} - \frac{\nabla p}{\rho} + \upsilon \Delta \bar{u}. \tag{2}$$

Equations (1) and (2) represent local conservation of mass and momentum respectively. The system of partial differential equations given by (1) and (2) can be derived from these fundamental conservation principles assuming that the fluid is incompressible and Newtonian and that the motion of the fluid is three-dimensional and time-dependent.

The first step in developing an approximate model to describe surface waves in an accelerating cylindrical container is to transform equation (2) into a non-inertial coordinate system. Figure 1 shows the inertial and non-inertial coordinates systems which will be used in the present discussion.

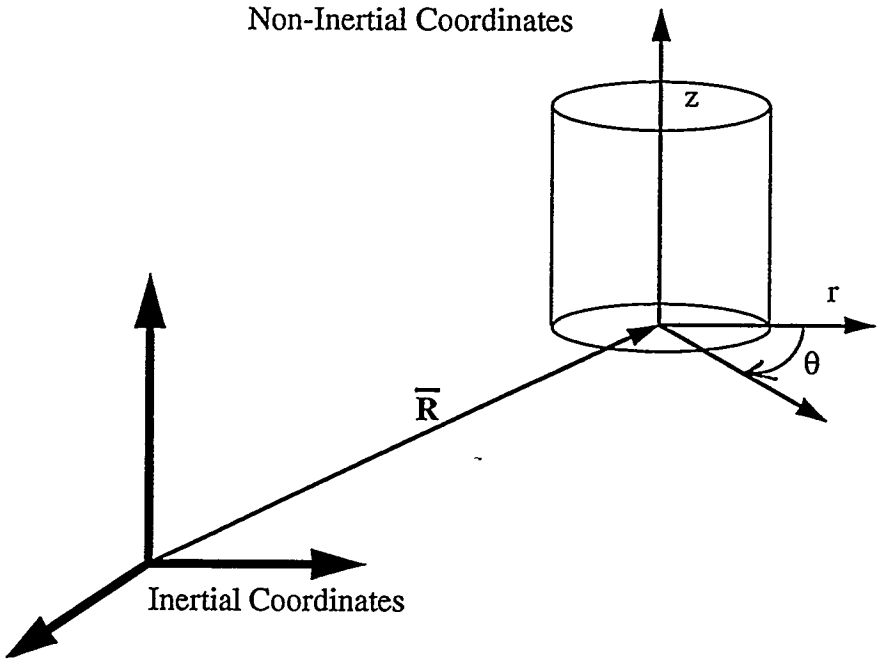

Figure 1 Inertial and non-inertial coordinate systems for a cylindrical container.

Following White [6], the fluid velocity in the non-inertial coordinate system can be related to the inertial system by the expression:

$$\bar{u} = \bar{V} + \frac{d\bar{R}}{dt} + \bar{\Omega} \times \bar{r}, \tag{3}$$

where the relative velocity $\bar{V}$, the angular velocity $\bar{\Omega}$, and the radial vector $\bar{r}$ are referenced from the origin of the non-inertial system. In the subsequent analysis it will be assumed that the container will experience little or no angular velocity in the non-inertial system, so that $\bar{\Omega} = 0$. Equation (3) then reduces to:

$$\bar{u} = \bar{V} + \frac{d\bar{R}}{dt}, \tag{4}$$

where $\frac{d\bar{R}}{dt}$ is assumed to be a function of time and not position.

Now, to simplify the Navier-Stokes equations (1) and (2) to the point that surface wave oscillation frequencies can be approximated, surface wave motions are assumed to be inviscid and irrotational ($\upsilon = 0$ and $\nabla \times \bar{V} = 0$). These addition physical assumptions admit a velocity potential function, ϕ, satisfying:

$$\bar{V} = \nabla \phi. \tag{5}$$

Then combining conservation of mass, equation (1), with equation (5) yields the basic differential equation modeling surface wave motion:

$$\Delta \phi = 0. \tag{6}$$

The next step in approximating surface wave motion is to determine the physical boundary conditions needed to specify a solution of equation (6).

Two types of boundary conditions are used in studying the motion of surface waves: wall conditions and free-surface conditions. Assuming that there is no fluid movement through the walls of the cylindrical container, the inviscid fluid wall boundary conditions become:

$$\bar{n} \bullet \bar{V} = 0. \tag{7}$$

Combining equations (5) and (7) then yields the two boundary conditions:

$$\frac{\partial \phi}{\partial r}(a, \theta, z, t) = 0, \tag{8}$$

and

$$\frac{\partial \phi}{\partial z}(r, \theta, 0, t) = 0, \tag{9}$$

where a is the radius of the cylindrical container. As shown in Figure 1, the origin of the non-inertial coordinates is located at the center of the bottom of the container. The second type of boundary condition describes the behavior of the free-surface. Two relations may be used on the surface: a kinematic condition and a pressure condition. The kinematic boundary condition is given by:

$$\frac{D(z-\eta)}{Dt} = 0, \tag{10}$$

where is η the shape of the free-surface a function of both position and time. This condition means physically that a particle of fluid on the surface will always stay on the surface, Lamb [3]. The pressure boundary condition is obtained by applying equations (4) and (5) to equation (2) and integrating the results for the conservative body force $\overline{F} = (0, 0, -g)$. This yields a time-dependent Bernoulli equation, which may be represented in cartesian coordinates as:

$$\frac{\partial \phi}{\partial t} + \frac{p}{\rho} + \frac{1}{2}\nabla\phi \bullet \nabla\phi + gz - (a_X x + a_Y y + a_Z z) = f, \tag{11}$$

where the acceleration terms (a_X, a_Y, a_Z) are defined by:

$$\frac{d^2\overline{R}}{dt^2} = (a_X, a_Y, a_Z). \tag{12}$$

The right-hand-side of (11) is the Bernoulli constant, which drops out in the present analysis.

The boundary conditions defined by equations (10) and (11) may be simplified further by linearizing and combining these equations. Linearizing equation (11) assumes that the nonlinear terms are small in comparison with the linear terms and may be neglected. This step is valid for surface waves which have small amplitudes from the undisturbed free-surface. Differentiating (11) and applying (10) removes the pressure term, since the pressure on the surface is assumed constant. Then, in cylindrical coordinates, the free-surface boundary condition for a constant acceleration (a_r, a_θ, a_z) becomes:

$$\frac{\partial^2 \phi}{\partial t \partial t} + (g - a_z)\frac{\partial \phi}{\partial z} - \left(a_r \frac{\partial \phi}{\partial r} + a_\theta \frac{1}{r}\frac{\partial \phi}{\partial \theta}\right) = 0. \tag{13}$$

The approximate model used to estimate surface wave oscillation frequencies is given by solutions of equation (6) subject to the boundary conditions defined by equations (8), (9) and (13).

Now, by separation of variables, the solution to equation (6) in cylindrical coordinates can be shown to be:

$$\phi = (A_{1m}\sin m\theta + A_{2m}\cos m\theta)\,(B_{1m}\sinh kz + B_{2m}\cosh kz)\,J_m(kr)\sin \omega t, \tag{14}$$

for each integer m. In equation (14), the A_m's and B_m's are constants and the J_m's are Bessel functions of the first kind. Applying boundary conditions (8) and (9) reduces (14) to

$$\phi = \sum (K_{1m}\sin m\theta + K_{2m}\cos m\theta)\cosh kz J_m(kr)\sin \omega t, \tag{15}$$

where the K_m's are constants. Nontrivial solutions result only for the case when the Bessel functions satisfy:

$$J'_m(ka) = 0. \tag{16}$$

The final boundary condition, the free-surface constraint, can now be applied to obtain determine an expression for the surface wave oscillation frequencies. Two special cases of this relation are developed in the next section.

Example Cases

Example 1: No acceleration of the cylindrical container. For this case, equation (12) becomes

$$\frac{d^2\overline{R}}{dt^2} = 0, \tag{17}$$

which reduces equation (13) to:

$$\frac{\partial^2\phi}{\partial t \partial t} + g\frac{\partial \phi}{\partial z} = 0. \tag{18}$$

Then substituting equation (15) into (18) yields the surface wave oscillation frequency as:

$$\omega^2 = gk\tanh kh, \tag{19}$$

where h is the unperturbed height of the free-surface measured from the bottom of the container. Equation (19) for the frequency is a classical result which can be found is elementary texts on fluid mechanics, such as in Currie [2]. Now, if $kh > 1$, the frequency may be approximated by:

$$\omega \approx \sqrt{gk}. \tag{20}$$

Example 2: Constant linear acceleration of the cylindrical container in the Y/Z plane. For this second case, equation (12) becomes:

$$\frac{d^2\overline{R}}{dt^2} = (0, a_Y, a_Z) \ , \tag{21}$$

a constant vector. Then substituting equation (15) into equation (13) produces the oscillation frequency:

$$\omega^2 = (g - a_z)\, k \tanh kh + a_\theta \frac{m}{r} F(\theta) - a_r \frac{J'_m(kr)}{J_m(kr)}, \tag{22}$$

where

$$F(\theta) = \frac{(K^1 \cos m\theta - K^2 \sin m\theta)}{(K^1 \sin m\theta + K^2 \cos m\theta)}. \tag{23}$$

By rewriting $K^1 \sin m\theta + K^2 \cos m\theta$ as $\hat{K} \cos(m\theta - \delta)$, where $\hat{K}$ and δ are functions of the K's, equation (23) may be expressed as:

$$F(\theta) = -\tan(m\theta - \delta). \tag{24}$$

In view of equations (16) and (24), equation (22) may be simplified by evaluating it at $r = a$. This yields an approximation for the surface wave oscillation frequency as:

$$\omega^2 = (g - a_z)\, k \tanh kh - a_\theta \frac{m}{a} \tan(m\theta - \delta) \ , \tag{25}$$

where m is an angular mode number.

Now, to further simplify equation (25), notice that the components of the acceleration vector given by equation (21) may be written in cylindrical coordinates as:

$$\begin{aligned} a_r &= a_Y \sin\theta, \\ a_\theta &= a_Y \cos\theta, \\ a_z &= a_Z. \end{aligned} \tag{26}$$

Substituting equations (26) into equation (25) for the special case of $m = 1$ and $\delta = 0$ produces:

$$\omega^2 = (g - a_z)\, k \tanh kh - \frac{a_Y}{a} \sin\theta. \tag{27}$$

For $kh > 1$, equation (27) implies that the surface wave oscillation frequency is bounded approximately by:

$$\sqrt{(g - a_z)\,k - \frac{a_Y}{a}} \le \omega \le \sqrt{(g - a_z)\,k + \frac{a_Y}{a}}. \tag{28}$$

Numerical Evaluation of the Oscillation Frequency

Numerical values of the surface wave oscillation frequency may be determined using equations (20) and (28) once the separation of variables constant, k, is known. Recall equation (16):

$$J'_m(ka) = 0. \tag{16}$$

For a fixed mode number m and a fixed container radius a, the roots of equation (16) yield values of k. Table 1 below, taken from reference [1], lists the first five roots for equation (16) as a function of the mode numbers, $m = 0, 1, 2, 3, 4$:

Root No.	m = 0	m = 1	m = 2	m = 3	m = 4
n = 1	0.000	1.841	3.054	4.201	5.318
n = 2	3.832	5.331	6.706	8.015	9.282
n = 3	7.016	8.536	9.969	11.346	12.682
n = 4	10.173	11.706	13.170	14.586	15.964
n = 5	13.324	14.864	16.348	17.789	19.196

Table 1: Values of ka, i.e., the first five roots of equation (16).

Conclusions and Recommendations

This memo has outlined simple formulas to estimate the sloshing frequencies of surface waves in right cylindrical containers subject to simple accelerations. The relationships presented here can be applied to estimate the order of magnitude of the oscillation frequencies for linear, inviscid, irrotational surface waves in non-rotating containers.

It is recommended that any future work on estimating the frequencies and motions of free-surface waves in moving cylindrical containers include a careful background study of the material properties of the liquids of interest. To determine surface wave oscillation frequencies accurately, the local constitutive and surface properties of the liquid must be known. The expected amplitude of the free-surface waves must also be estimated to

determine if a linear theory is applicable. If small amplitude waves are believed to result from the accelerations of the containers, and if the liquids are Newtonian fluids, a linear mathematical model can be developed to provide reasonable estimates of the free-surface frequencies.

A more general linear theoretical model can be developed to estimate surface wave sloshing frequencies for arbitrary container geometries and accelerations. Such a description, based on the work of Moiseev [4 and 5], would yield an eigenvalue problem in terms of integral equations. The resulting integrals could then be solved numerically to estimate the free-surface sloshing frequencies. This theoretical description represents the next level of sophistication in estimating the motion of surface waves for inviscid, irrotational liquids.

It is further recommended that any future work on estimating surface wave oscillation frequencies include a detailed experimental study of free-surface motions for the container geometries and liquids of interest. Experimental measurements could be used to determine the range of possible free-surface motions for given container motions. Such an experimental study could also reveal important physical behaviors neglected by the analysis.

References

1. Abramowitz, M. and Stegun, I. A., *Handbook of Mathematical Functions*, Dover, 1972.

2. Currie, I. G., *Fundamental Mechanics of Fluids*, McGraw Hill, 1974.

3. Lamb, H., *Hydrodynamics*, 6th Edition, Dover, 1945.

4. Moiseev, N. N., "Introduction to the Theory of Oscillations of Liquid-Containing Bodies," *Advances in Applied Mechanics*, Vol. 8, Academic Press, 1964.

5. Moiseev, N. N., "The Calculation of Free Oscillations of a Liquid in a Motionless Container," *Advances in Applied Mechanics*, Vol. 9, Academic Press, 1966.

6. White, F. M., *Fluid Mechanics*, McGraw Hill, 1979.

Distribution

MS0841 1500 D. J. McCloskey
MS0836 1501 C. W. Peterson
Route to: MS0834 (1512), MS0835 (1513)
MS0827 1502 P. J. Hommert
Route to: MS0825 (1554), MS0826 (1553), MS0827 (1511), MS0841 (1504)
MS0832 1551 W. P. Wolfe
MS0832 1551 J. K. Cole
MS0833 1552 C.E. Hailey
MS0833 1552 J. H. Strickland
MS0443 1561 H. S. Morgan
Route to: MS0437 (1562)
MS0833 1552 R. S. Baty

Copy to:
MS0833 1552 Day File

Appendix B

Vicente J. Romero

HSlosh

A Computer Code for Modeling Transient 2-D Sloshing of a Pseudo-Viscous Liquid in a Horizontally Oscillating Container

Intentionally Left Blank

___ J. T. Feddema MS-0949
(2111)

Sandia National Laboratories
Albuquerque, New Mexico 87185

date: November 6, 1994

to: Rush Robinett, 9811 (MS 0314)

Vicente Romero

from: Vicente J. Romero, 1513 (MS 0835)

subject: HSLOSH (a computer code for modeling transient 2-D sloshing of a pseudo-viscous liquid in a horizontally oscillating container)

Executive Summary

Robotic machines are increasingly being used to transport containers of liquid from one location to another. It is desired to attain the highest work speeds possible without inducing unacceptable sloshing, which could result in spillage and/or application of large unpredictable forces to the robot. Sandia is developing a formal optimization procedure to help prescribe robotic manipulations that strike the best balance between slosh inducement and work speed. To support this effort, the computer model HSLOSH has been developed to predict the sloshing of fluid in horizontally accelerated containers. This report describes the model, its operation, and a benchmark example problem. The model is being further developed to include provisions for vertical and angular pitching motions. Rayleigh damping is used to approximately account for the effects of viscosity in the potential-flow formulation. HSLOSH uses a boundary element approach to efficiently handle the changing fluid geometry and uses Lagrangian node movement to accommodate violent sloshing.

Introduction

Robotic machines are increasingly being used to transport containers of liquid from one location to another. Sandia is currently studying the problem of getting such containers from point A to point B as quickly as possible without inducing unacceptable sloshing in the liquid. For open containers this could mean preventing spillage, and for both open and closed containers this could mean preventing potentially large unpredictable forces from being imparted to the robot. The goal is to develop control algorithms for robotic movement that avoids the creation of undesirable fluid oscillations (free-surface motions) and/or actively damps such oscillations, thus permitting higher working speeds. It is envisioned that a fluid model can be used in an optimization context to help accomplish this goal.

As a first step in investigating the effect that container movement has on sloshing, a separation-of-variables solution has been used to report the sloshing frequencies for wave formation in an inviscid, irrotational fluid contained in a laterally accelerated right-circular cylinder (see Reference [1]). In this memo, fully transient nonlinear (high-amplitude) waves in a pseudo-viscous fluid in a rectangular container subjected to time-varying

horizontal accelerations are considered. The effects of viscosity are approximated by imparting Rayleigh damping to a potential-flow model of the fluid. The computer program HSLOSH uses a boundary element approach to efficiently handle the changing fluid geometry and allows for violent sloshing of the liquid.

Model Problem

The model problem of a rectangular container subjected to sinusoidal horizontal oscillation has been chosen for preliminary application of the numerical model (see Figure 1). Initially the container of width w is at rest and holdin a quiescent body of liquid of depth d (relative to the bottom of the container). The container displacement δ_c and velocity v_c from its initial position are given by

$$\delta_c = A\sin\omega t \tag{1}$$

and

$$v_c = A\omega\cos\omega t \tag{2}$$

where ω is the angular frequency of the oscillation. In terms of the period T_p of the oscillation, ω is given by

$$\omega = 2\pi/T_p \tag{3}$$

The container is assumed to extend into and out of the page far enough that end effects are negligible and a two-dimensional (2-D) treatment applies.

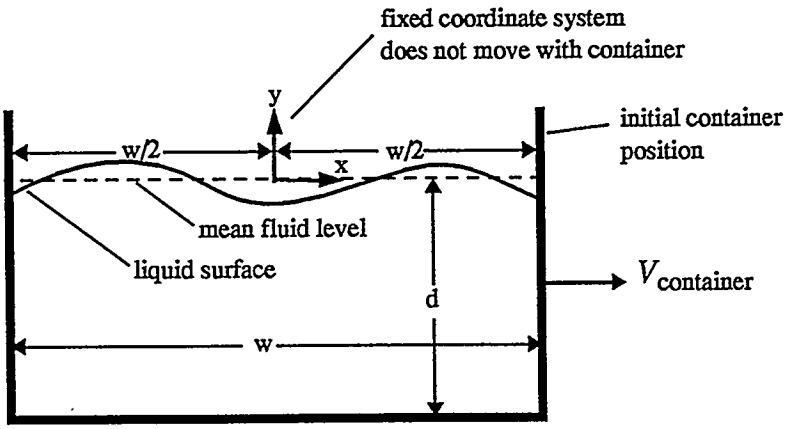

Figure 1: Model problem: a horizontally oscillating container holding fluid

Mathematical Nature of Free-Surface Potential Flows

Some Preliminaries

Free interfaces are found at the boundary between two immiscible fluids with different densities. If the interface is curved, a jump in the fluid pressures across the interface exists due to surface tension σ. For a 2-D problem, the difference in the pressures on the concave and convex sides of the interface is given by

$$p_{\text{concave}} - p_{\text{convex}} = \frac{\sigma}{R} \tag{4}$$

where R is the local radius of curvature of the surface. If the interface is an air/liquid interface, we call the interface a "free surface". If we employ no special device to manipulate the local air pressure at the free surface, we may assume that the pressure on the air side of the interface is equal to the atmospheric pressure p_a. We get, for the fluid pressure p,

$$p = p_a \pm \frac{\sigma}{R} \tag{5}$$

where the positive sign is used if the fluid is on the locally concave side of the interface and the negative sign is used when the fluid is on the convex side.

The free interface moves in a transient problem to establish mechanical equilibrium between the two fluids. To model the motion of the fluid, momentum conservation must be applied. The mathematical development in [1] uses a noninertial coordinate system moving with the container to solve the linearized sloshing problem. However, it is more convenient in solving the nonlinear problem to skip this transformation and work directly from the inertial fixed x-y coordinate system depicted in Figure 1. Assuming the fluid to be irrotational[1], *i.e.* the curl of the velocity is everywhere zero ($\nabla \times \vec{v}_{fluid} = 0$), a velocity potential $\phi\,(x, y, t)$ governs the flow field such that it's gradient represents the fluid velocity at any point:

$$\vec{v}_{fluid} = \nabla\phi \tag{6}$$

Assuming incompressibility, conservation of mass requires that the divergence of the velocity be zero everywhere within the fluid. This translates to the requirement that ϕ satisfy Laplace's equation in the domain:

$$\nabla \bullet \vec{v}_{fluid} = 0 \quad \Rightarrow \quad \nabla^2\phi = 0 \tag{7}$$

Under the additional assumption of negligible viscous effects (which completes the set of assumptions characterizing potential flow), the time-consistency of the problem is established by Kelvin's theorem (see [2]), which states that an inviscid and initially irrotational flow will always remain irrotational, and therefore that Laplace's equation will apply throughout time.

We may fully characterize the flow over the time span of interest by resolving the time-dependent velocity field within the domain. At any point in time, solution of Laplace's equation for the velocity potential ϕ with subsequent use of Equation (6) yields the velocity field. The

---

[1] This is a very good assumption at early times for initially quiescent sloshing flows.

boundary conditions (b.c.s) for the Laplace part of our problem are illustrated in Figure 2 for our example sloshing problem (we will arrive at these through the considerations below). We note that Laplace's equation is a linear elliptic equation. Nonlinearity and time dependence are introduced through the boundary conditions to the Laplace problem and through the time-changing geometry of the domain due to the movement of the free surface and of other boundaries (such as the container boundaries) whose motion may be prescribed as a function of time.

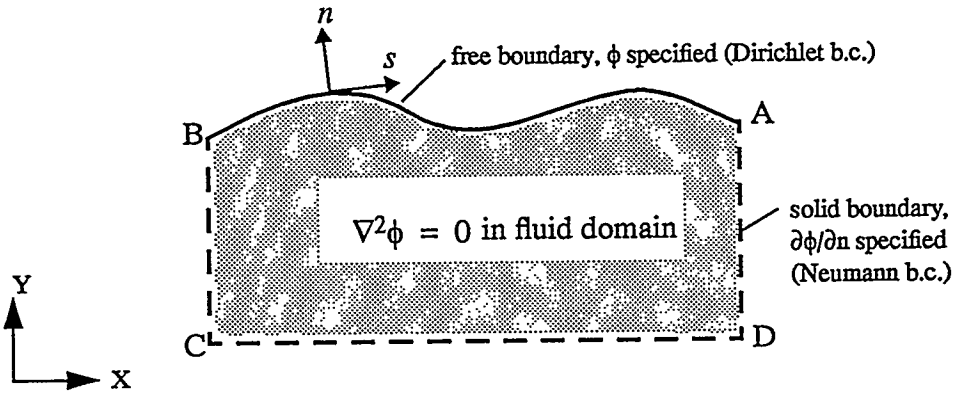

Figure 2: Laplace problem associated with the example sloshing problem

The Kinematic Condition and Evolution of Free-Surface Geometry

One of the characteristic difficulties of solving free-surface problems arises from the fact that the geometry of the problem changes over time in a manner not known *a priori*. The evolution of the fluid domain is coupled into the problem and must be solved for. We must move our mathematical representation of the free boundary according to physical considerations of the fluid motion. The "kinematic condition", which applies all along the fluid boundary, provides the link between physical and mathematical considerations of boundary movement. The general statement of the kinematic condition is

$$\hat{n} \bullet \vec{v}_{point} = \hat{n} \bullet \vec{v}_{fluid} \tag{8}$$

where $\vec{v}_{point}$ is the velocity of some point on the mathematical boundary and $\hat{n}$ is a unit vector locally perpendicular to the boundary, pointing outward from the fluid domain.

The kinematic condition reflects the fact that for points on the mathematical boundary to track the fluid surface their velocities relative to the fluid at the surface must be either wholly tangential or zero [3]. If the relative velocity is zero, then the point moves as though it were a fluid particle at the free surface, satisfying the kinematic equation identically (substitute $\vec{v}_{point}=\vec{v}_{fluid}$ into

Equation (8)). We will adopt this convention to move our computational nodes on the free surface in a physically realistic manner. Though other conventions exist that satisfy Equation (8), "Lagrangian" movement has unique properties that would appear to make it well suited for simulation of sloshing flows. Though apparently not yet applied to sloshing problems *per se*, Lagrangian node movement has been very successfully used to model highly nonlinear, impulsive, and violent flows such as those generated by piston wavemakers or oscillating floating bodies, with waves eventually crashing (overturning) or impacting tilted or vertical walls ([4]-[7]). Accordingly, we set

$$\vec{v}_{node} = \vec{v}_{fluid} = \nabla\phi \tag{9}$$

Considering that $\vec{v}_{node}$ is the time derivative of nodal position $\vec{r}_{node}$ $(= x_{node}\hat{i} + y_{node}\hat{j})$, we have

$$\vec{v}_{node} = \frac{d}{dt}(\vec{r}_{node}) = \frac{d}{dt}(x_{node})\hat{i} + \frac{d}{dt}(y_{node})\hat{j} \tag{10}$$

from which we may form ordinary differential equations (ODEs) for Cartesian position of free-surface nodes:

$$\frac{d}{dt}(x_{node}) = \hat{i} \bullet \vec{v}_{node} = \frac{\partial\phi}{\partial x} \tag{11}$$

and

$$\frac{d}{dt}(y_{node}) = \hat{j} \bullet \vec{v}_{node} = \frac{\partial\phi}{\partial y} \tag{12}$$

In the above we have used Equation (9) and written $\nabla\phi$ in terms of its x and y components, whence

$$\nabla\phi = \frac{\partial\phi}{\partial x}\hat{i} + \frac{\partial\phi}{\partial y}\hat{j} \tag{13}$$

In the discretized problem, numerical determination of the spatial derivatives of $\nabla\phi$ on the right-hand sides (RHSs) of equations (11) and (12) involves a solution of Laplace's equation, which depends in part upon the quantities x_{node} and y_{node} themselves. Thus, (11) and (12) constitute a set of coupled, nonlinear ODEs. In general, one such set exists at each computational node on the free surface. All the sets taken together constitute a 2N set of globally coupled nonlinear ODEs governing the time evolution of free-surface geometry (where N is the number of nodes on the free surface).

The Kinematic Condition for Neumann Boundary Conditions at Solid Boundaries

We have seen that at free boundaries the kinematic condition and the solution to Laplace's equation are used to achieve physically consistent movement of the mathematical boundary. Conversely, we will see here that at solid boundaries (either moving or fixed) in the physical problem, the kinematic condition is used to provide Neumann boundary conditions for the associated Laplace problem.

Our fluid conforms to solid boundaries. For our mathematical representation of the fluid boundary to reflect this conformance it is necessary for any point on the mathematical boundary to assume a velocity normal to the body that is dictated by the body's motion in that direction. Thus,

$$\hat{n} \bullet \vec{v}_{point} = \hat{n} \bullet \vec{v}_{body}. \tag{14}$$

Using equations (6) and (14) in (8) we obtain a Neumann condition for the Laplace problem at physical boundaries:

$$\frac{\partial \phi}{\partial n} = \hat{n} \bullet \vec{v}_{body} \tag{15}$$

For our model problem we have

$$\vec{v}_{body} = \vec{v}_{container} = v_c \hat{i} + 0\hat{j} \tag{16}$$

Noting from Figure 2 that $\hat{n}$ equals $-\hat{i}$, $-\hat{j}$, and $\hat{i}$ for the left, bottom, and right walls of the container, we obtain

$$\left.\frac{\partial \phi}{\partial n}\right|_{left} = -v_c \tag{17}$$

$$\left.\frac{\partial \phi}{\partial n}\right|_{bottom} = 0 \tag{18}$$

$$\left.\frac{\partial \phi}{\partial n}\right|_{right} = v_c \tag{19}$$

The Dynamic Condition and Evolution of the Dirichlet Boundary Condition at the Free Surface

Above we have obtained Neumann boundary conditions for the Laplace problem where the fluid meets solid boundaries. The Laplace-problem boundary condition at the free surface is obtained from the unsteady Bernoulli equation, which applies within and on the boundary of the fluid. A derivation of this equation, which proceeds from consideration of momentum conservation along a flow streamline, may be found in [2], where the additional assumption of conservative body forces (e.g. gravity) is invoked. Reference [8] indicates how a simplifying mechanism to account for the major effects of viscosity[2] may be included in the momentum equation according to a device originally proposed by Lord Rayleigh. Such "Rayleigh damping" acts to dissipate momentum by opposing fluid motion with a force proportional to the local gradient of fluid velocity. The constant of proportionality or "viscosity coefficient" μ changes with the flow regime

---

[2] It is not clear whether addition of this false viscosity invalidates the time-invariance of vorticity (here, irrotationality) concluded from Kelvin's theorem. However, we will proceed on the assumption that Kelvin's theorem still applies.

and is best set by comparison with experiments or computer analyses solving the full Navier-Stokes fluid-flow equations (see e.g. [9]).

Applied at the free surface, the damping-modified unsteady Bernoulli equation becomes

$$\frac{\partial \phi}{\partial t} = -\left[\frac{v^2}{2} + \frac{\pm\frac{\sigma}{R}}{\rho} + gy + \mu\phi\right] \tag{20}$$

where y is the vertical coordinate (height of the free surface relative to the x axis), ρ is the fluid density, g is the magnitude of gravitational acceleration, v is the fluid speed (magnitude of the local velocity vector $\vec{v}_{fluid}$), and Equation (5) has been used to write the fluid-side pressure at the free interface with atmospheric pressure p_a assumed to be spatially uniform on the gas side of the interface.

When Bernoulli's equation is applied at the free surface it is known as the "dynamic condition" in free-surface potential-flow nomenclature. We employ it to update the velocity potential ϕ on the free surface as the simulation progresses in time. This provides a Dirichlet boundary condition at the free surface that is used in solving Laplace's equation.

Equation (20) is a nonlinear partial differential equation (PDE) boundary condition, and may be more explicitly seen to be so in a form obtained by replacing v^2 by $\nabla\phi \bullet \nabla\phi$ in view of Equation (6):

$$\frac{\partial \phi}{\partial t} = -\left[\frac{1}{2}\frac{\partial \phi}{\partial x}\frac{\partial (\ )}{\partial x} + \frac{1}{2}\frac{\partial \phi}{\partial y}\frac{\partial (\ )}{\partial y} + \mu(\phi)\right]\phi - \frac{\pm\frac{\sigma}{R}}{\rho} - gy \tag{21}$$

The operator in brackets is clearly a function of ϕ, making the PDE nonlinear. Thus, this free-surface boundary condition imparts nonlinearity and time dependence to the problem, as do the evolution equations (11) and (12) for the location of the free surface.

We note that Equation (21) pertains to the partial or "Eulerian" time derivative of the velocity potential $\phi(x, y, t)$, taken while holding x-y position fixed. However, we must use the total time-derivative[3] in updating ϕ on the **moving** free surface. For a moving node the total time-rate-of-change of its velocity potential is given by[4]

$$\frac{d}{dt}(\phi_{node}) = \frac{\partial}{\partial t}\phi(x, y, t) + \vec{v}_{node} \bullet \nabla\phi(x, y, t) \tag{22}$$

Substituting equations (20) and (9) into (22) and neglecting surface tension in our model[5], we obtain the ODE consistent with Lagrangian node movement that governs the time evolution of nodal velocity potential (thus the Dirichlet boundary condition) at the free surface:

---

[3] Reference [10] quite nicely catalogues and illustrates the differences between partial, total, and substantial or material time-derivatives.

[4] Among other simplifications, the linearized version of the free-surface potential-flow problem does not account for fluid motion in the differential equation for ϕ at the free surface. Thus, $\vec{v}_{node}$ in Equation (22) is taken to be zero.

[5] though it would be fairly easy to implement (*cf* [11])

$$\frac{d}{dt}(\phi_{node}) = \frac{1}{2}(\nabla\phi \bullet \nabla\phi) - gy - \mu\phi \tag{23}$$

For the discretized problem, numerical approximations for the spatial derivatives in $\nabla\phi$ at node *i* typically involve the nodal quantity ϕ_i. Therefore, higher-order products of ϕ_i are contained in the quantity $\nabla\phi \bullet \nabla\phi$, making the ODE (23) nonlinear[6]. Furthermore, since these numerical approximations involve the values of ϕ at other free-surface nodes, the set of ODEs formed by applying Equation (23) at all the free-surface nodes constitutes a globally coupled set of N nonlinear ODEs.

Identification as an Initial/Boundary-Value Problem

It is further remarked that Equation (23) is coupled to the nonlinear ODEs (11) and (12) for updating the position of the free surface. All together, we have a set of 3N coupled, nonlinear ordinary differential equations that must be time-integrated. In an interdependent manner, solution of the nodal ODEs at the free boundary requires the solution of Laplace's equation over the domain with subsequent determination of the gradient terms that appear in the right-hand sides of equations (11), (12), and (23). Simultaneously, solution of Laplace's equation requires (among other things) the solution to equations (11), (12), and (23) to update the domain geometry and provide a Dirichlet b.c. on the free boundary.

To summarize, we have an elliptic boundary-value problem for ϕ within the fluid (we must satisfy Laplace's equation over the domain), and initial-value problems in free-surface geometry and velocity potential. We must solve the coupled nonlinear initial-value problems while simultaneously satisfying Laplace's equation over the domain. Assuming we have time-specified Neumann b.c.s on the nonfree portions of the boundary, we start from initial conditions of specified geometry and velocity potential. We choose a method of node movement that satisfies the kinematic condition (Lagrangian movement in this model). We select a method for solution of Laplace's equation and discretize the problem accordingly. We solve the Laplace problem and calculate the components of $\nabla\phi$ on the free boundary, inserting them into the RHSs of equations (11), (12), and (23) as appropriate. We may then use established time marching techniques to advance the solution in time. At the completion of each time step we have the new locations of free-surface nodes and their new velocity potentials. This, along with the time-prescribed information in the problem, allows us to solve Laplace's equation in preparation for taking the next time step.

We remark that the Lagrangian time derivatives $d(\phi_{node})/dt$, $d(x_{node})/dt$, and $d(y_{node})/dt$ are expressed in terms of the only derivatives directly available to us —Eulerian temporal and spatial derivatives of $\phi(x, y, t)$. Since we solve for (*i.e.* time march) nodal quantities that are Lagrangian in the sense that they reflect our motion as we follow fluid particles on the free surface, and since we must appeal to spatial and temporal derivatives of Eulerian-based quantities in order to evaluate the Lagrangian time-derivatives, the formulation is often referred to as a mixed Eulerian/ Lagrangian one.

---

6. Accordingly, the term $\nabla\phi \bullet \nabla\phi$ in equation (23) is dropped completely in the linearized version of the problem.

Outline of Numerical Solution Procedures

Solution Method for Laplace's Equation and the Gradient of the Velocity Potential

Although domain methods[7] have been employed in solving free-surface potential-flow problems, boundary integral techniques ([16], [17]) appear to offer superior performance for this type of problem (*cf* [18], [19]). The direct boundary element method (DBEM, [20]) is particularly accurate and efficient at solving Laplace's equation and, since it transforms the problem from one of solving a PDE over the domain to one of solving an integral equation over the boundary of the domain, reduces by one the dimensionality of the problem. This is particularly beneficial for problems where the domain geometry changes in time; for 2-D problems it is much easier to adaptively discretize a closed curve than an arbitrary 2-D area, and for 3-D problems it is vastly easier to discretize a surface than an arbitrary 3-D volume.

For our example problem we use the DBEM to solve the following Fredholm boundary integral equation (BIE):

$$\alpha(\underset{\sim}{p})\,\phi(\underset{\sim}{p}) = \int_{\Gamma}\left[\phi(\underset{\sim}{\xi})\frac{\partial}{\partial n}\ln r(\underset{\sim}{\xi},\underset{\sim}{p}) - \ln r(\underset{\sim}{\xi},\underset{\sim}{p})\frac{\partial\phi}{\partial n}(\underset{\sim}{\xi})\right]d\Gamma(\underset{\sim}{\xi}) \tag{24}$$

where $\phi(\underset{\sim}{p})$ is the velocity potential at a particular point p on the boundary, $\alpha(\underset{\sim}{p})$ is the internal angle of the boundary contour there (see Figure 3), $\ln r$ is the value at $\underset{\sim}{\xi}$ of 2π times the 2-D free-space Green's function centered at $\underset{\sim}{p}$ and $r = |\underset{\sim}{\xi} - \underset{\sim}{p}|$. The operator $\tilde{\partial}(\ )/\partial n$ finds the rate of change of the operated quantity in the direction normal to the boundary and pointing away from the interior of the domain. A very readable and concise derivation of Equation (24) based on Green's second identity can be found in [21].

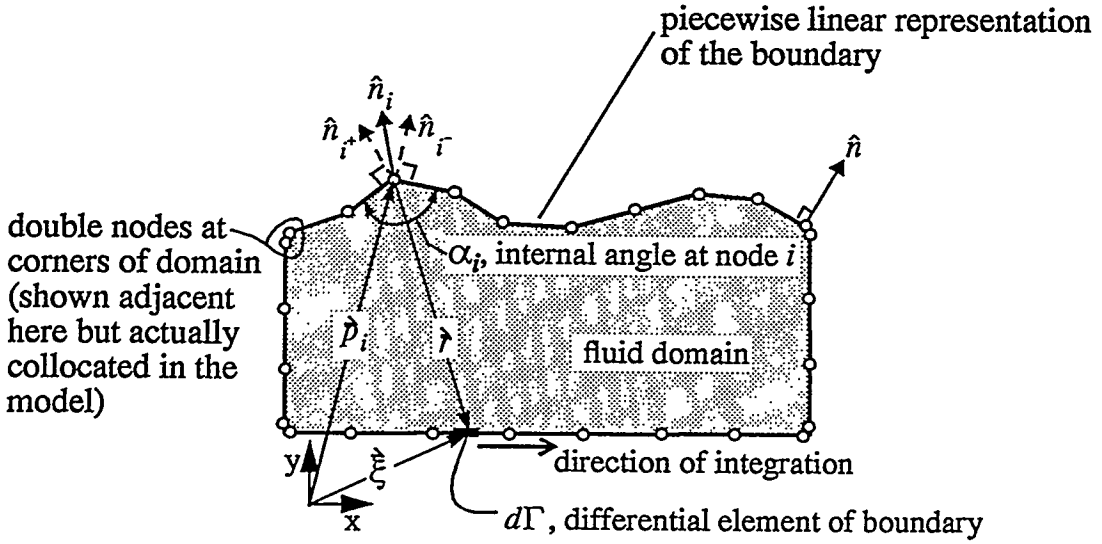

Figure 3: Boundary element model of fluid domain

[7] finite element/difference/volume methods, e.g. [12]-[15]

When Equation (24) is used to solve for the potential at a point p on the boundary given the normal flux (Neumann b.c.) there and known fluxes or potentials on the remainder of the boundary, it is known as a Fredholm boundary integral equation of the second kind. When the potential is known at p and the normal flux is to be solved for, Equation (24) becomes a Fredholm boundary integral equation of the first kind. In our example problem, Neumann boundary conditions are given on some portions of the boundary and Dirichlet conditions are given on the other portions. Therefore, we use Equation (24) in both a first- and second- kind capacity and our formulation becomes a mixed Fredholm one. Other formulations exist which are exclusively first-kind [22] or second-kind [23]. These have advantages in some respects, but are usually limited in applicability or less stable numerically (see [24] for a discussion).

Using the principle of collocation, Equation (24) is written at all nodes on the domain boundary. Using standard discretization techniques these BIE are represented in discrete form and assembled into a set of globally coupled linear algebraic equations that can be solved by Gaussian elimination. The present formulation uses a piecewise linear approximation to the domain boundary. Linear isoparametric boundary elements are employed which allow exact analytic integrations (see [25]) of Green's function and its normal derivative over the elements. Other types of boundary elements and integration methods have been used in free-surface problems with good success (*cf* [7], [8], [26]-[29]). A double-node technique is used to address the double-valuedness[8] of the normal direction at the four vertices of the domain, denoted A, B, C, and D in Figure 2. Two computational nodes are placed at each vertex, one associated with each of the adjoining boundary segments, and BIEs are written at the nodes and assembled into the set of discretized equations according as the boundary condition prescribed on the adjoining segment is Neumann or Dirichlet. (This approach is slightly simpler to code than inserting a constraint equation for continuity of potential at the collocated nodes as suggested in [4], [7], [29], and [30] and yields the same result.)

Solution of the complete set of discretized BIEs yields the velocity potential ϕ at nodes where a Neumann condition was specified, and the normal derivative of the velocity potential, $\partial\phi/\partial n$, at nodes where Dirichlet boundary conditions were supplied. Thus, on the free surface where ϕ is known from time integrating Equation (23), the value of $\partial\phi/\partial n$ at the node "pops out" of the solution of the BIEs.

It is natural, then, to seek the tangential derivative of the velocity potential $\partial\phi/\partial s$ that complements the normal derivative in forming the gradient

$$\nabla_n \phi = \frac{\partial \phi}{\partial n}\hat{n} + \frac{\partial \phi}{\partial s}\hat{s} \tag{25}$$

($\hat{s}$ is the unit vector tangent to the fluid boundary as shown in Figure 2).

Equation (25) is the form of the gradient most conveniently used in (23). Likewise, the following transformations are used for the spatial derivatives in equations (11) and (12):

$$\frac{\partial \phi}{\partial x} = -\sin\beta\frac{\partial \phi}{\partial n} + \cos\beta\frac{\partial \phi}{\partial s} \tag{26}$$

---

8. $\hat{n}$ has a jump discontinuity at the vertices; in traversing the boundary its value changes abruptly at these points

$$\frac{\partial \phi}{\partial y} = \cos\beta \frac{\partial \phi}{\partial n} + \sin\beta \frac{\partial \phi}{\partial s} \tag{27}$$

where, as shown in Figure 4, β is the angle between the horizontal and the tangent vector $\hat{s}$ at the fluid boundary. As Figure 3 shows, the nodes on the ends of the piecewise-linear approximation to the free surface have unambiguous tangent directions, but the other free-surface nodes do not. In the present model the average of the tangent directions of the elements on either side of the nodes is used. The nodal normals $\hat{n}_i$ are obtained by rotating the so-obtained nodal tangents $\hat{s}_i$ 90 degrees counter-clockwise.

Although a more elegant method (the tangent-derivative BEM [31]) exists to determine $\partial\phi/\partial s$ at the free surface, numerical differencing is used in the present model. Following Liu & Liggett [32], a central difference approximation for $\partial\phi/\partial s$ that accounts for the (in general) different lengths of adjacent free-surface elements is used.

At the "contact points" A and B in Figure 2 where the free surface meets a solid boundary, constraint equations are used in preference to numerical differencing to determine $\partial\phi/\partial s$. By virtue of equations (17), (19), and (26), we obtain at these contact points

$$\frac{\partial \phi}{\partial x} = v_c \tag{28}$$

where β is taken to be $\pi/2$ and $-\pi/2$ along the left and right sides of the container, respectively.

Manipulating Equation (26) and substituting the above we get[9]

$$\frac{\partial \phi}{\partial s} = \frac{v_c}{\cos\beta} + \tan\beta \frac{\partial \phi}{\partial n} \tag{29}$$

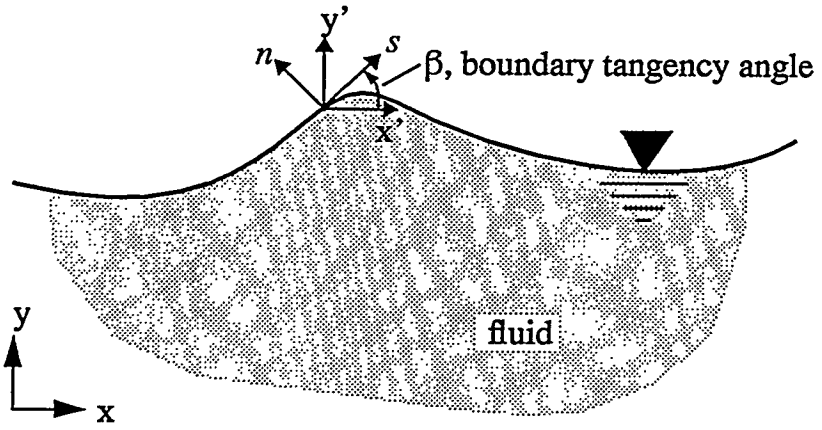

Figure 4: Boundary tangency angle β

[9] This differs from the result published in [29], but in nonetheless believed correct.

After solution of the BIEs, all quantities on the RHS of Equation (29) are known, and so, $\partial\phi/\partial s$ can be calculated directly. Note that impulsive wall motions (v_c discontinuous in time[10]) will generate a singularity at the contact point [33]. Though more exotic elements and integration techniques exist to resolve these singularities (see e.g. [29]), the numerical procedures used here will be adequate if motions are not "too" impulsive, which would appear to be the case for robotic systems configured to minimize sloshing.

Time-Marching Method

The temporal character of our initial/boundary-value problem is captured by the coupled nonlinear ordinary differential equations (11), (12), and (23) written at the free-surface nodes. Since the spatial derivatives on the RHSs of these ODEs are obtained from the solution to Laplace's equation, and this solution (via the DBEM) depends in part upon the nodal values of ϕ at the free surface and on the x and y coordinates of the nodes, the ODEs have the functional form:

$$\dot{\phi}_i = \frac{d\phi_i}{dt} = f_i\Big(\{\phi_i\}, \{x_i\}, \{y_i\}, t \Big) \tag{30}$$

$$\dot{x}_i = \frac{dx_i}{dt} = g_i\Big(\{\phi_i\}, \{x_i\}, \{y_i\}, t \Big) \tag{31}$$

$$\dot{y}_i = \frac{dy_i}{dt} = h_i\Big(\{\phi_i\}, \{x_i\}, \{y_i\}, t \Big) \tag{32}$$

where $\{\phi_i\}$ denotes an array (list) of the velocity potentials of the free-surface nodes (and analogously for $\{x_i\}$ and $\{y_i\}$), and f_i denotes a functional relationship between the ensuing arguments that is particular to free-surface node i and of characteristic type f (the explicit form of which is given by the RHS of Equation (23)), and analogously for g_i and h_i.

We may append the lists $\{\phi_i\}$, $\{x_i\}$, and $\{y_i\}$ into a larger array $\{w_k\}$ and conceptualize[11] the complete ODE set in standard ODE matrix notation:

$$\{\dot{w}_k\} = \Big[A(\{w_k\}, t)\Big]\{w_k\} + \{F_k(t)\} \tag{33}$$

where it has been emphasized that the coefficient matrix [A] is a function of $\{w_k\}$ for a set of nonlinear ODEs and can have an explicit dependence upon time where prescribed changes in geometry and Neumann conditions on solid boundaries occur. Other independent (uncoupled)

---

[10] This includes the case of an initially prescribed v_c that is inconsistent with initial conditions on the fluid, such as the case of an initially still body of liquid impulsively started from rest (this occurs in the validation test problem considered later).

[11] Because the partial derivatives on the RHSs of the ODEs are obtained via integral (BIE) methods, instead of explicitly via differencing, the ODE set cannot be explicitly written in the suggested form. However, a whole body of theory associated with various linear multistep time-marching methods (e.g. [35]]) is predicated upon this form, and we can think of our equations set as having this form implicitly and therefore freely apply the *explicit* time-marching methods developed for it.

factors in the problem, such as a prescribed spatially varying pressure distribution p_a applied at the free surface, are contained in the $\{F_k\}$ vector of known functions of time.

Standard explicit time-marching methods (see e.g. [34]) can be applied to Equation (33) to advance the solution in time. Variants of the present model have been used to model other (non-sloshing) free-surface flows, during which implicit Generalized Trapezoidal and explicit Taylor Series, Runge-Kutta, and Adams-Bashforth time-integrators have been tried. Experience has shown that the variable-step 4th-5th order Runge-Kutta integrator DERK45 [37] from the Sandia SLATEC library [36] advances the nonstiff set of ODEs with a good balance of accuracy, economy, stability, and easy of implementation. Accordingly, this integrator has been used in the sloshing model.

Model Validation

The algorithm described above has been written into a FORTRAN computer code called **HSLOSH**. The code has been applied to the test problem described above and the results are here compared to results published in the literature.

Reference [8] describes a previously developed computer model for the example sloshing problem. Other, perhaps more sophisticated computer models employing finite elements ([12], [13]) and boundary elements [38] have been applied to this problem, but in these works the problem has been set up in transformed coordinates convenient for solving the linear problem (see [1]), and there is good reason to believe that the nonlinear problem has not been posed correctly in the transformed coordinates. Thus, the results in [8] provide the only viable standard for comparison. Briefly, Faltinsen's model employs a fixed-step "central difference"[12] time-marching method with constant boundary elements in an indirect boundary element formulation for solving Laplace's equation. Due to constraints on node movement the formulation breaks down when the absolute value of β on the free surface approaches large angles, like when large and violent free-surface motions are involved.

The governing parameters for the validation problem are (refer to Figure 1 and pp. 2):

$w = 1$ meter [m]

$d = 0.5$ m

$A = 0.025$m

$T_p = 1.3$ seconds [s]

$g = 9.8$ m/s^2

$\mu = 0.05\mu_{crit}$

where, following [8], an estimate of the critical damping coefficient μ_{crit} is given by

---

[12] The expression "central difference" is sometimes used to connote the 2nd order method more commonly known as the "midpoint rule", "trapezoidal method", or "centered theta method". However, no mention is given of how the ODEs are linearized and iterated to accomplish the implicit time steps that such a method would imply. Since this would be a nontrivial aspect of the model (see e.g. [11] for a linearization with the implicit theta method), the author would not likely omit mention of it if the time-marching was indeed implicit. Thus, it is inconclusive whether the trapezoidal method was indeed the method used.

$$\mu_{crit} = 2\sqrt{\frac{g\pi}{w}\tanh\left(\frac{d\pi}{w}\right)} \tag{34}$$

Faltinsen's model has 10 elements on the free surface and, though not explicitly stated, there are indications that the bottom and lateral boundaries are also divided into 10 elements each. The author indicated that the number of elements used was probably inadequate (but necessarily so because of limited computing resources) to resolve the finer subtleties of the fluid motion, but that the discretization was probably sufficient to allow an examination of its gross motion.

In the current model the boundary of the domain is divided into: 60 elements on the free surface, 30 elements on the bottom boundary, and 20 on either side. For the example problem this is probably more than sufficient to capture the local details of the fluid motion. (No attempt was made to duplicate the number of elements used in [x] in an effort to verify the current model by exact duplication of the published results because of the confounding effects of other algorithmic differences.) The elements on the side and bottom boundaries are always equally spaced, even though the lengths of the side elements change as the fluid rides up and down the container walls. The lengths of the free-surface elements are not constrained in any way, but Lagrangian node movement tends to concentrate nodes in highly curved regions of the free surface wherever jets of liquid are formed [22]. This is in some ways desirable because of the natural increase in resolution at precisely the locations on the free surface where "the action is". However, when nodes are too close together, special numerical procedures may be required, depending upon the type of elements used and method of integration, to accurately solve the BIEs (see e.g. [29]). Additionally, the clustering of nodes may decrease the stability of the system, requiring smaller time steps to be taken or periodic regridding of the free surface to be done [7]. None of these special measures have been implemented in HSLOSH, but can be later if necessary.

The ODE integrator DERK45 requires as input the relative[13] and absolute error tolerancing parameters RTOL and ATOL, respectively. The results below were obtained with values of ATOL=10^{-5} and RTOL=10^{-4} to provide good stability and accuracy properties. These are probably more stringent than necessary in some cases, but allowed running the model over a large range of container oscillation amplitudes and frequencies. As the discussion below will reveal, instabilities[14] did arise in some simulations. In these cases, loosening the error tolerances caused instabilities to arise sooner, while tightening the parameters allowed the calculations to proceed longer, as expected. Since computation time is relatively sensitive to RTOL and ATOL, these parameters should be as loose as possible while still meeting the accuracy requirements and allowing a far enough progression in time.

Figure 5 shows the present model's prediction of fluid response as measured by deviation in surface height from the mean fluid level. Free-surface dispacement at a distance 0.05m from the left wall of the container (i.e. the absolute location of the measurement point changes in time following the motion of the container) and at a fixed coordinate location x = -0.45m are plotted vs.

---

13. as a fraction of the magnitudes of the time-marched variables, here velocity potential and x and y Cartesian coordinates

14. Numerical instabilities and methods to suppress or circumvent them have received much attention in the literature on computational free-surface potential flows (e.g. [7], [22]-[24], [39]). The present model incorporates no special measures to delay the onset of instability except for controlling the sizes of the time steps by appropriate selection of the error tolerancing parameters.

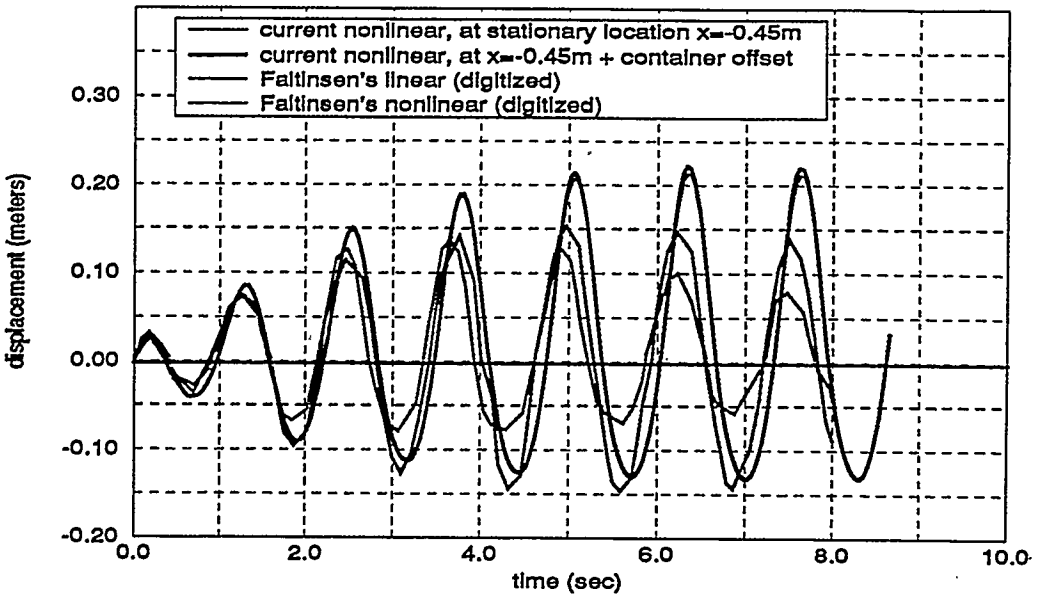

Figure 5: Free-surface displacement from rest level at a distance 0.05 m from left side of container. Container oscillation period = T_p = 1.3 sec.

time. Nonlinear and linear predictions digitized from [8] are also shown for comparison. Though not explicitly stated, it is likely from the different ways in which the linear and nonlinear problems were posed and solved that the nonlinear solution corresponds to a fixed location x = -0.45m, while the linear solution corresponds to a location fixed relative to the container 0.05m from the left wall. As the results of the current model show, the distinction in this case is unimportant because the responses for these two locations are very nearly the same. The nonlinear solutions from the present model are quite different from Faltinsen's solution. All the nonlinear solutions are notably different from the linear solution, which probably does not apply very well for this very nonlinear flow (note that the amplitudes of up to 22 cm are of the same order of magnitude as both the depth and the width of the domain). Though the amplitudes of the solutions are considerably different, the phases all agree reasonably well. The nonlinear results produced by both Faltinsen's and the current model exhibit the characteristic trait of crests with substantially greater amplitude than troughs. This physically observed characteristic of nonlinear waves is not predicted by linear models. The amplitudes of the crests are usually of most interest in sloshing flows because of their association with liquid spillage and higher pressures (thus forces) on container walls. Nonlinear computations using approaches substantially different from the current one have predicted higher crests than linear theory predicts under other types of forcing conditions such as applied spatially varying pressure distributions [32], objects moving just beneath the fluid surface [14], and piston wave-makers [4]. Their results have been replicated with variants of the current model, which here also predicts higher crests than the linear solution indicates (about 50% higher in some cases). The nonlinear model of Faltinsen, however, predicts substantially lower crests than linear theory predicts. This provides an indication that the current model may be more accurate than Faultisen's nonlinear model.

Further evidence that the current model is more accurate than Faltinsen's is shown in Figure 6, which plots the predicted responses when the simulation is rerun with an oscillation period of T_p = 1.6 seconds. The response is much less regular, presumably because the oscillation frequency is further from the predicted linear resonance frequency of 1.18 seconds. For this much more linear problem (maximum amplitudes about 7 cm), the present model much more closely conforms to the linear predictions than does the nonlinear model of Faltinsen. We can expect that as the behavior becomes less and less nonlinear, the nonlinear solution should converge to the linear solution. The present model appears to possess this property much more so than Faltinsen's. To establish convergence, however, requires more data than that published in [8]. Therefore, Roy Baty of 1515 is in the process of programming Faultisen's analytic solution. This will allow better verification of the nonlinear code in linear flow regimes, thereby lending more credence to the results that it produces in nonlinear regimes.

For an oscillation period of T_p = 1.2 seconds, Figure 7 shows the shape of the free surface when the container approaches its center of oscillatory motion at succeeding multiples of the oscillation period. A period of 1.2 seconds was determined by numerical experiment to excite the fluid motion in a most resonance-like condition (cause fastest amplitude growth). The calculation had to be suspended at t = 4.4 seconds because of an instability that erupted shortly thereafter. At periods of 1.18 seconds and 1.3 seconds such instabilities did not errupt until slightly later, and at a period of 1.6 seconds, far away from the resonance condition, the calculation was run to 14 seconds with no hint of impending instability. A typical run took about 2 hours of CPU time on a SUN workstation (50mhz SPARCstation20). A possible explanation for the instabilities in this Lagrangian-type code may be increasing node congregation at the crests of the fluid as the calculation proceeds in time. Sometimes special measures must be implemented to account for this,

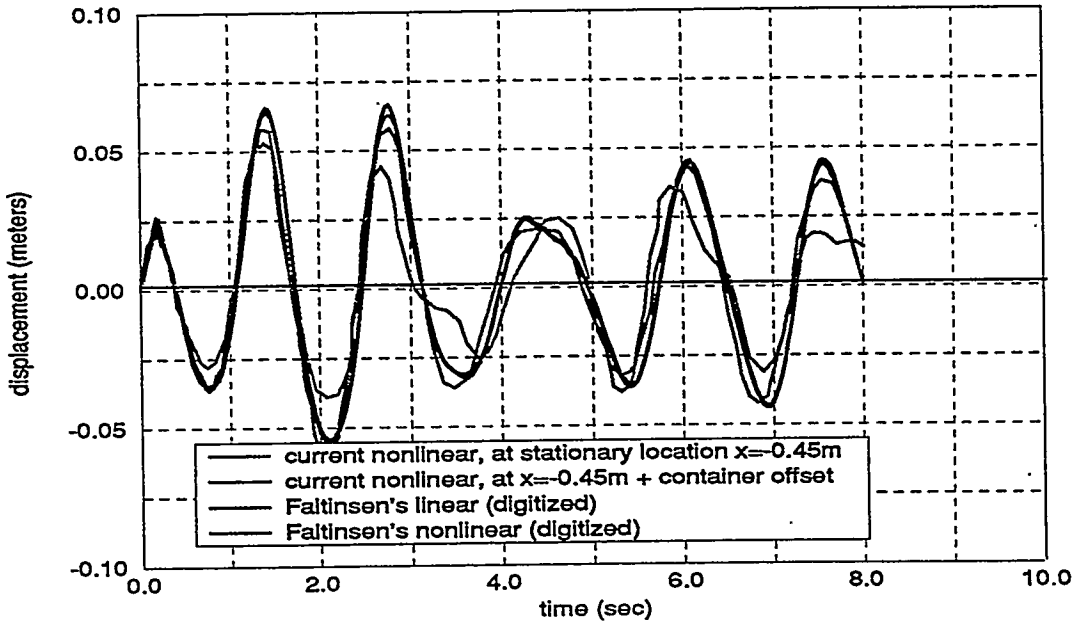

Figure 6: Free-surface displacement from rest level at a distance 0.05 m from left side of container. Container oscillation period = T_p = 1.6 sec.

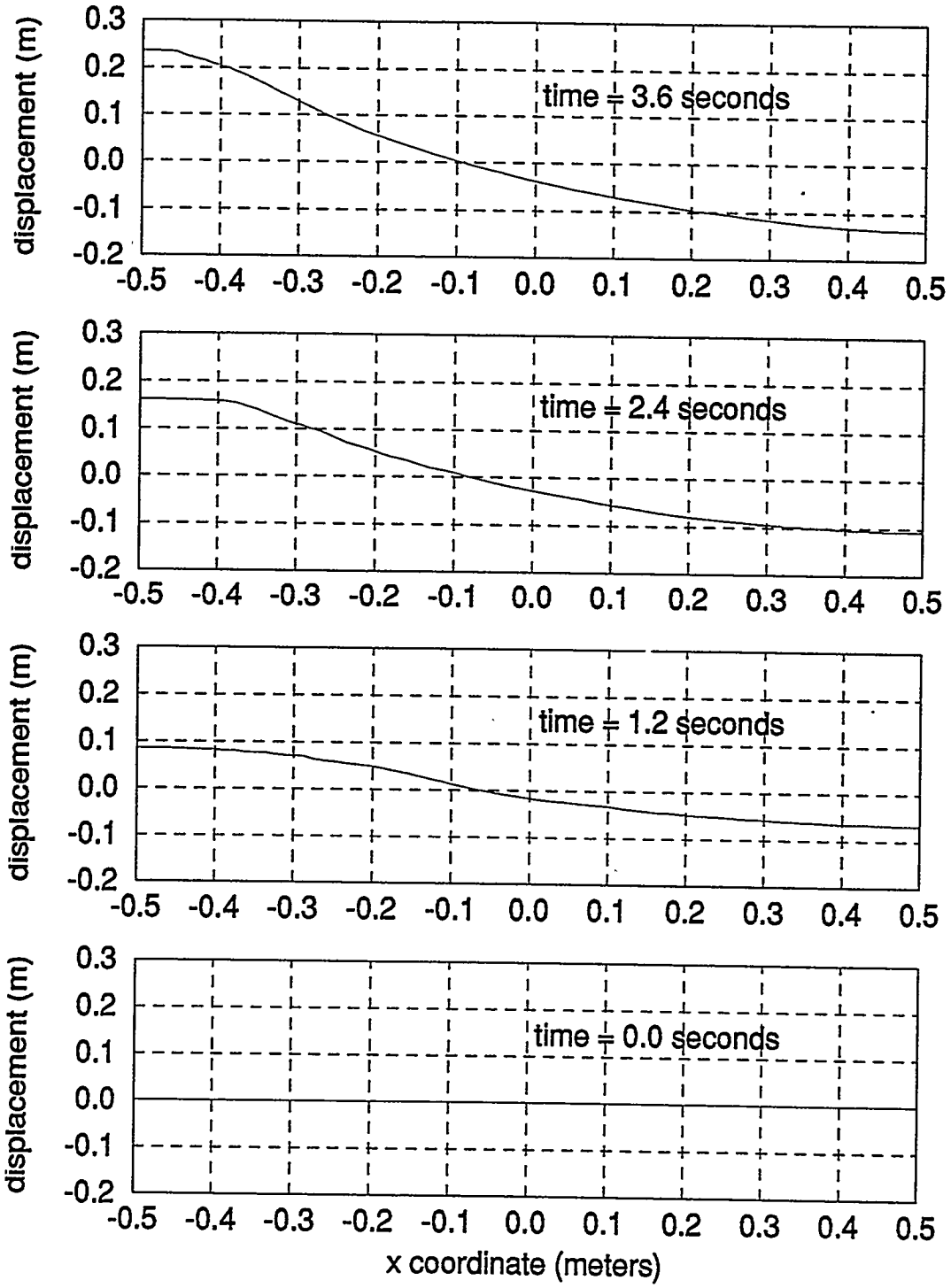

Figure 7: Evolution of free surface shown at multiples of the container oscillation period T_p = 1.2 sec. (near natural frequency of the liquid)

and none have been instituted here in the initial development of the code. However, the robotic tasks that HSLOSH will be associated with will typically be executed on much shorter time scales than 4 seconds. Nonetheless, if instability does interfere with the usefulness of the current model, many established procedures can be easily implemented to circumvent or suppress them (see Footnote 14).

Conclusions and Recommendations

HSLOSH appears to correctly model the behavior of an incompressible, damped, initially irrotational fluid within a container subjected to forced horizontal oscillation, although more validation is necessary. Determination of an appropriate damping coefficient for a particular liquid and forcing condition must be made in order for the model to be correctly applied. As it stands now, the model can accomodate arbitrary container shapes and horizontal motions, but user input is presently cumbersome except for a rectangular container experiencing horizontal harmonic motion. Future work will involve implementing provisions for vertical and angular pitching motions and validation against benchmark problems in the literature, e.g. [40]-[42]. In addition, several ways to significantly increase code efficiency have been identified and will be implemented. To treat arbitrary container rotations or containers with length-to-width ratios less than about 5, the model must be made three-dimensional, which would require significant but straightforward modifications to the existing model.

References

[1] Memo from R. S. Baty, 1552, to R. D. Robinett, 9811, dated June 3, 1994, subject: Sloshing frequencies in cylindrical containers.

[2] Currie, I.G., *Fundamental Mechanics of Fluids,* McGraw-Hill Book Co., 1974.

[3] Lamb, H., *Hydrodynamics*, 6th. ed., Dover Publications, New York, 1945.

[4] Nakayama, T., "A computational method for simulating transient motions of an incompressible inviscid fluid with a free surface," Int. J. for Num. Mthds. in Engr. (1990), vol. 10, pp. 683-695.

[5] Faltinsen, O.M., "Numerical solutions of transient nonlinear free-surface motion outside or inside moving bodies," *Proceedings of the Second International Conference on Numerical Ship Hydrodynamics,* University of California at Berkeley, September 1977, pp. 347-357.

[6] Grilli, S.T., Skourup, J., and Svendsen, I.A., "An efficient boundary element method for nonlinear water waves," Engr. Analysis with Boundary Elements (1989), vol. 6, no. 2, pp. 97-107.

[7] Dommermuth, D.G., and Yue, D.K., "Numerical simulations of nonlinear axisymmetric flows with a free surface," J. Fluid Mech. (1987), vol. 178, pp. 195-219.

[8] Faltinsen, O.M., "A nonlinear theory of sloshing in rectangular tanks," J. Ship Research (1974), vol. 18, pp. 224-241.

[9] Case, K.M., and Parkinson, W.C., "Damping of surface waves in an incompressible liquid," J. Fluid Mechanics (1957), vol. 2, part 2, pp. 172-184.

[10] Bird, R.B., Stewart, W.E., and Lightfoot, E.N., *Transport Phenomena*, John Wiley & Sons, 1960.

[11] Medina, D.E., and Liggett, J.A., "A consistent boundary element method for free surface hydrodymanic calculations," Int. J. for Num. Mthds. in Engr. (1991), vol. 12, pp. 835-857.

[12] Ikegawa, M., "Finite element analysis of fluid motion in a container," in *Finite Element Methods in Flow Problems*, eds. J.T. Oden, O.C. Zienkiewicz, R.H. Gallagher, and C. Taylor, UAH Press, Huntsville, 1974, pp. 737-738.

[13] Washizu, K., Nakayama, T., and Ikegawa, M., "Application of the finite element method to some free surface fluid problems," in *Finite Elements in Water Resources*, eds. W.G. Gray, G.F. Pinder, and C.A. Brebbia, Pentech Press, London, 1978, pp. 4.247-4.266.

[14] Haussling, H.J., and Coleman, R.M., "Finite-difference computations using boundary-fitted co-ordinates for free-surface potential flows generated by submerged bodies," *Proceedings of the Second International Conference on Numerical Ship Hydrodynamics*, University of California at Berkeley, September 1977, pp. 221-233.

[15] Welch, J.E., Harlow, F.H., Shannon, J.P., Daly, B.J., "The MAC (Marker-and-Cell) Method: A computing technique for solving viscous, incompressible, transient fluid-flow problems involving free surfaces," Los Alamos Scientific Laboratory Report LA-3425, University of California, Los Alamos, NM, 1966.

[16] Kellogg, O.D., *Foundations of Potential Theory*, Dover, New York, 1953.

[17] Jaswon, M.A., and Symm, G.T., *Integral Equation Methods in Potential Theory and Elastostatics*, Academic Press, London, 1977.

[18] Nakayama, T., "Boundary element analysis of nonlinear water wave problems," Int. J. for Num. Mthds. in Engr. (1983), vol. 19, pp. 953-970.

[19] Grilli, S., "Application of the Boundary Element Method to some elliptic fluid mechanics problems," in *Proceedings of the First Intl. Conf. on Computer Methods and Water Resources*, Rabat, Morocco, 1988, vol. 4 (eds. D. Ouazar and C.A. Brebbia), Computational Mechanics Publications, Springer-Verlag, Berlin, pp. 97-113.

[20] Brebbia, C.A., *The Boundary Element Method for Engineers*, Halsted Press, John Wiley & Sons, copyright 1978 by Pentech Press.

[21] Liggett, J.A., and Liu, P.L-F., *The Boundary Integral Equation Method for Porous Media Flow*, George Allen & Unwin, London, 1983.

[22] Longuet-Higgins, M.S., and Cokelet, E.D., "The deformation of steep surface waves on water: I. A numerical method of computation," Proc. R. Soc. Lond., Ser. A (1976), vol. 350, pp. 1-26.

[23] Baker, G.R., Meiron, D.I., and Orszag, S.A., "Generalized vortex methods for free-surface flow problems," J. Fluid Mech. (1982), vol. 123, pp. 477-501.

[24] Pelekasis, N.A., Tsamopoulos, J.A., and Manolis, G.D, "A hybrid finite-boundary element method for inviscid flows with free surfaces," J. Comp. Phys. (1992, August), vol. 101, pp. 231-251.

[25] Banerjee, G.R., and Butterfield, R., *Boundary Element Method in Engineering Science*, McGraw-Hill, U.K., 1981.

[26] Liggett, J.A., and Salmon, J.R., "Cubic spline boundary elements," Int. J. for Num. Mthds. in Engr. (1981), vol. 17, pp. 543-556.

[27] Cabral, J.J.S.P., and Wrobel, L.C., "Application of B-spline boundary elements to groundwater flow problems," in *Proceedings of Computational Modeling of Free and Moving Boundary Problems, Vol. 1 Fluid Flow*, First Int'l. Conf., July 2-4, 1991, Southampton, U.K., eds. L.C. Wrobel and C.A. Brebbia, copublished by Computational Mechanics Publications and Walter de Gruyter, 1991, pp. 20-36.

[28] Ortiz, J.C., and Douglass, S.L., "Overhauser boundary elements solution for periodic water waves in the physical plane," Engr. Anal. with Boundary Elements (1993), vol. 11, pp. 47-54.

[29] Grilli, S.T., and Svendsen, I.A., "Corner problems and global accuracy in the boundary element solution of nonlinear wave flows," Engr. Analysis with Boundary Elements (1990), Vol. 7, No. 4, pp. 178-195.

[30] Mitra, A.K., and Ingber, M.S., "A multiple-node method to resove the difficulties in the boundary integral equation method caused by corners and discontinuous boundary conditions," Int'l. J. for Num. Mthds. in Engr. (1993), vol. 36, pp. 1735-1746.

[31] Muci-Kuchler, K.H., and Rudolphi, T.J., "Application of tangent derivative boundary integral equations to the solution of elastostatics problems," *Boundary Element Technology VII*, eds. C.A. Brebbia and M.S. Ingber, proceedings of BETECH '92, U. of New Mexico, USA, Computational Mechanics Publications copublished with Elsevier Applieed Science, 1992, pp. 757-774.

[32] Liu, P.L-F., and Liggett, J.A., "Boundary element formulations and solutions for some nonlinear water wave problems," Chapter 7 of *Developments in Boundary Element Methods - 3*, P.K. Banerjee and S. Murkerjee, eds., Elsevier Applied Science Publishers, 1984, pp. 171-190.

[33] Cointe, R., "Remarks on the numerical treatment of the intersection point between a rigid body and a free surface," in *Proc. 3rd Int'l. Workshop on Water Waves and Floating Bodies*, Woods Hole, MA, USA, 1988.

[34] Ferziger, J.H., *Numerical Methods for Engineering Application*, John Wiley & Sons, 1981.

[35] Gear, C.W., *Numerical Initial Value Problems in Ordinary Differential Equations*, Prentice-Hall, Englewood Cliffs, N.J., 1971.

[36] Shampine, L.F., and Watts, H.A., "DEPAC--Design of a User Oriented Package of ODE Solvers," Sandia National Labs (Albuquerque, New Mexico, 87185) report SAND79-2374, printed September 1980.

[37] Haskell, K.H., Vandevender, W.H., and Walton, E.L., "The SLATEC Comon Mathematical Subprogram Library: SNLA Implementation," Sandia National Labs (Albuquerque, New Mexico, 87185) report SAND80-2792.

[38] Nakayama, T., and Washizu, K., "The boundary element method applied to the analysis of two-dimensional nonlinear sloshing problems," Int. J. for Num. Mthds. in Engr. (1981), vol. 17, pp. 1631-1646.

[39] Dold, J.W., "An efficient surface-integral algorithm applied to unsteady gravity waves," J. Comp. Phys. (1992), vol. 103, pp. 90-115.

[40] Taylor, G.I., "An experimental study of standing waves," Proc. Roy. Soc. London, Series A (1946), vol. 218, pp. 44-59.

[41] Benjamin, T.B., and Ursell, F., "The stability of the plane free surface of a liquid in vertical periodic motion," Proc. Roy. Soc. London, Series A (1954), vol. 225, pp. 505-515.

[42] Nakayama, T., and Washizu, K., "Nonlinear analysis of liquid motion in a container subjected to forced pitching oscillation," Int'l. J. Num. Mthds. in Engr. (1980), vol. 15, pp. 1207-1220.

KEYWORDS: Robotics, sloshing fluids, boundary element method (BEM), code development, case 4199.100

Copy to:

MS0949	2111	J. T. Feddema
MS0841	1500	D. J. McCloskey
MS0828	1502	P. J. Hommert (route to 1511)
MS0441	1503	J. H. Biffle (route to: 1517, 1518)
MS0828	1504	E. D. Gorham (route to: 1514, 1515)
MS0834	1512	A. C. Ratzel (route to 1516)
MS0835	1513	R. D. Skocypec
MS0835	1513	V. J. Romero
MS0835	1513	Day File
MS0833	1515	R. S. Baty

Intentionally Left Blank

Appendix C

Roy S. Baty

Model Surface Wave Problem

Intentionally Left Blank

Sandia National Laboratories

Albuquerque, New Mexico 87185-1515

date: November 18, 1994

to: V. J. Romero, MS0835/1513

Roy Baty

from: R. S. Baty, MS0825/1515

subject: Model Surface Wave Problem

Introduction

Early in 1994, R. D. Robinett, 9816, requested that the Engineering Sciences Center 1500 provide estimates of the sloshing frequencies in open containers partially filled with liquid. These frequency estimates have application to the development of a robotic control system to move open containers of liquid. The envisioned control system will have the capability to adjust the motion of liquid containers to damp undesirable free-surface motions. An overview of this surface wave slosh problem with simple analytical estimates of the sloshing frequencies was presented in Baty [1]. Romero [2] then extended this introductory study with numerical simulations of surface wave motion in two-dimensional rectangular tanks, using a boundary element method (BEM). The present memo outlines the analytical solution of a linear surface wave problem and compares this solution against the solution generated using the boundary element method. The problem studied here represents a two-dimensional, open, rectangular tank containing a viscous liquid which is subject to a small horizontal oscillation. The viscosity of the liquid is approximated with a damping term. The model problem and its solution are developed from the work of Faltinsen [3].

Nomenclature

A := forced oscillation amplitude.

a := half-width of tank (0.5m).

g := gravity constant.

h := height of liquid in tank (0.5m).

x, y := coordinate directions.

ξ := free-surface shape.

ξ_f := free-surface shape of forced oscillation.

ϕ := velocity potential.

ϕ_u := unforced potential.

ϕ_f := forced potential.

μ := damping coefficient.

ω := frequency of forced oscillation.

Linear Surface Wave Problem

Consider a two-dimensional, rectangular, open tank containing a liquid as shown in Figure 1. Assume the tank is forced to oscillate harmonically in the x-direction with a circular frequency of ω and a small amplitude of A. The free-surface shape of the liquid associated with the forced oscillation of the container will then take the form:

$$\xi_f(x, t) = (A \sin \omega t)\, x. \tag{1}$$

The first goal of the present memo is to outline a linear, analytical approximation of the free-surface motion resulting from the simple horizontal oscillation of the tank. This approximation will include a linear damping of the free-surface motion so that both transient and steady state wave motions may be studied.

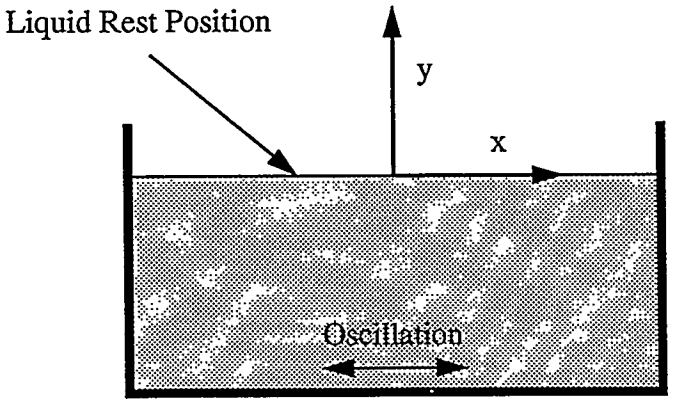

Figure 1. The model rectangular tank geometry and coordinate system. The tank is forced to oscillation in the horizontal direction.

The analytical approximation is developed by deriving a potential function, ϕ, for the liquid in the tank. Once the potential function has been determined, the motion of the free-surface may be approximated using the linearized kinematic free-surface boundary condition:

$$\frac{\partial \xi}{\partial t} = \frac{\partial \phi}{\partial y}. \tag{2}$$

Equation (2) may then be integrated to solve for ξ, yielding:

$$\xi = \int \frac{\partial \phi}{\partial y} dt. \tag{3}$$

The potential function required in equation (3) is derived from an initial-boundary value problem. This function is assumed to be of the form

$$\phi = \phi_u + \phi_f, \tag{4}$$

where ϕ_u is the unforced potential and ϕ_f is the forced potential. In view of equation (1), the forced potential is given by:

$$\phi_f = (A \cos \omega t)\, x. \tag{5}$$

To determine the unforced potential, Laplace's equation

$$\Delta \phi_u = 0, \tag{6}$$

must be solved subject to the boundary conditions:

$$\frac{\partial^2}{\partial t^2}(\phi_u) + \mu \frac{\partial}{\partial t}(\phi_u) + g \frac{\partial}{\partial y}(\phi_u)$$

$$= \left(\omega^2 A \cos \omega t + \mu \omega A \sin \omega t \right) x \text{ on } y = 0, \tag{7}$$

and

$$\frac{\partial \phi_u}{\partial n} = 0 \text{ on the tank boundaries.} \tag{8}$$

In addition to the boundary conditions, initial conditions must be specified to determine a potential function satisfying equations (4), (5), and (6). The initial conditions for the linear free-surface problem are given by:

$$\phi(x, y, 0) = 0, \tag{9}$$

and

$$\frac{\partial \phi}{\partial t}(x, y, 0) = 0. \tag{10}$$

The initial-boundary value problem for the unforced potential is then given by solving equation (6) subject to equations (7) through (10).

Analytical Solution

Applying separation of variables to equation (6), it can be shown that a general solution for the unforced potential may be written in the form:

$$\phi_u = \sum_{n=0}^{\infty} T_n(t) \sin\left(\frac{(2n+1)\pi}{2a}x\right)\cosh\left(\frac{(2n+1)\pi}{2a}(y+h)\right) \tag{11}$$

where the T_n are unknown functions of time. Equation (11) satisfies the boundary condition (8) as discussed in Currie [4]. Now, to simplify the development, notice that the x dependence in equations (5) and (7) may be expressed as a Fourier series:

$$x = \frac{2}{a}\sum_{n=0}^{\infty}\left(\frac{2a}{(2n+1)\pi}\right)^2 (-1)^n \sin\left(\frac{(2n+1)\pi}{2a}x\right) \tag{12}$$

representing a straight line. Details of the development of a Fourier series for a linear function are given in Kreyszig [5].

Now, substituting equations (11) and (12) into equation (7) yields

$$T_n''(t) + \mu T_n'(t) + \omega_n^2 T_n(t) = (\omega\cos\omega t + \mu\sin\omega t) K_n \text{ for } n = 0, 1, 2, \ldots, \tag{13}$$

where

$$\omega_n^2 = g\left(\frac{(2n+1)\pi}{2a}\right)\tanh\left(\frac{(2n+1)\pi}{2a}h\right), \tag{14}$$

and

$$K_n = \frac{\omega A}{\cosh\left(\frac{(2n+1)\pi h}{2a}\right)}\frac{2}{a}\left(\frac{2a}{(2n+1)\pi}\right)^2 (-1)^n. \tag{15}$$

A solution of equation (13) is then given by

$$T_n(t) = \exp\left((-\mu/2)\,t\right)\left(A_n\cos\sigma t + B_n\sin\sigma t\right) + C_n\cos\omega t + D_n\sin\omega t, \tag{16}$$

where

$$\sigma = \sqrt{\omega_n^2 - \frac{\mu^2}{4}}, \tag{17}$$

$$C_n = \frac{\omega K_n\left(\omega_n^2 - \omega^2\right) - \mu^2\omega K_n}{\left(\omega_n^2 - \omega^2\right)^2 + \mu^2\omega^2}, \tag{18}$$

and

$$D_n = \frac{\left(\omega_n^2 - \omega^2\right)\mu K_n + \mu\omega^2 K_n}{\left(\omega_n^2 - \omega^2\right)^2 + \mu^2\omega^2}. \tag{19}$$

Next, combining equations (4) and (5) with (11), (12), and (16), a solution for the boundary value problem defined by equations (4) through (8) becomes:

$$\phi = \sum_{n=0}^{\infty} \sin\left(\frac{(2n+1)\,\pi}{2a}x\right)\left(A\cos\omega t\left(\frac{2}{a}\right)\left(\frac{2a}{(2n+1)\,\pi}\right)^2(-1)^n\right)$$

$$+ \sum_{n=0}^{\infty} \sin\left(\frac{(2n+1)\,\pi}{2a}x\right)\cosh\left(\frac{(2n+1)\,\pi}{2a}(y+h)\right)$$

$$\times\left(\exp\left((-\mu/2)\,t\right)\left(A_n\cos\sigma t + B_n\sin\sigma t\right) + C_n\cos\omega t + D_n\sin\omega t\right). \tag{20}$$

The next step is to apply the initial values from equations (9) and (10) to determine the coefficients A_n and B_n in equation (20). The initial conditions then yield:

$$A_n = -C_n - \frac{K_n}{\omega}, \tag{21}$$

and

$$B_n = \frac{1}{\sigma}\left(\frac{\mu}{2}A_n - \omega D_n\right), \tag{22}$$

where σ is defined by equation (17). The complete solution for the velocity potential for the free-surface motion in the oscillating tank is given by equation (17) through (22).

The shape of the free-surface can then be determined by substituting equation (20) into equation (3). Differentiating equation (20) with respect to y and then integrating with respect to time produces the free-surface shape as a function of position and time:

$$\xi = \sum_{n=0}^{\infty} \left(\frac{(2n+1)\pi}{2a} \right) \sinh\left(\left(\frac{(2n+1)\pi}{2a} \right) (y+h) \right)$$

$$\times \left(\exp\left((-\mu/2)\, t \right) \left(\frac{A_n}{\omega_n^2} \left(\sigma \sin \sigma t - \frac{\mu}{2} \cos \sigma t \right) - \frac{B_n}{\omega_n^2} \left(\frac{\mu}{2} \sin \sigma t + \sigma \cos \sigma t \right) \right) \right.$$

$$\left. + \frac{C_n}{\omega} \sin \omega t - \frac{D_n}{\omega} \cos \omega t \right). \qquad (23)$$

Figures 2 and 3 show the normalized values of equation (23) plotted as a function of time for the circular frequencies $\omega = 3.9270, 5.7120$, respectively. Only the zero terms, $n = 0$, are shown; the terms corresponding to $n \geq 1$ are small and may be neglected. In figures 2 and 3, the free-surface shape function ξ assumes the damping coefficient $\mu = 0.5314$ and the coordinate values $x = -0.45$ and $y = 0.0$. Figure 4 then compares equation (23) with the boundary element method results of Romero [2] for the case of $\omega = 3.9270$ and $\mu = 0.5314$. This figure demonstrates that the BEM solution provides an accurate prediction of the shape and frequencies for the linear, model surface wave problem.

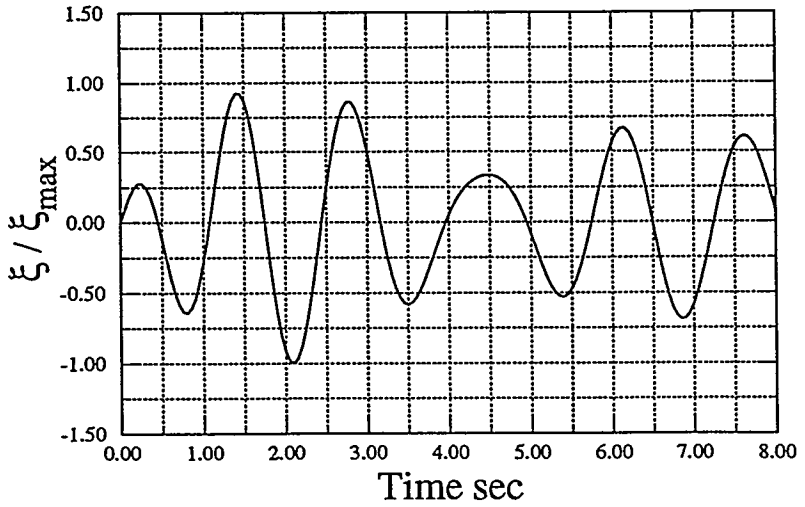

Figure 2. Normalized linear solution of the model surface wave problem as a function of time for $\omega = 3.9270$, $\mu = 0.5314$, $x = -0.45$, and $y = 0.0$.

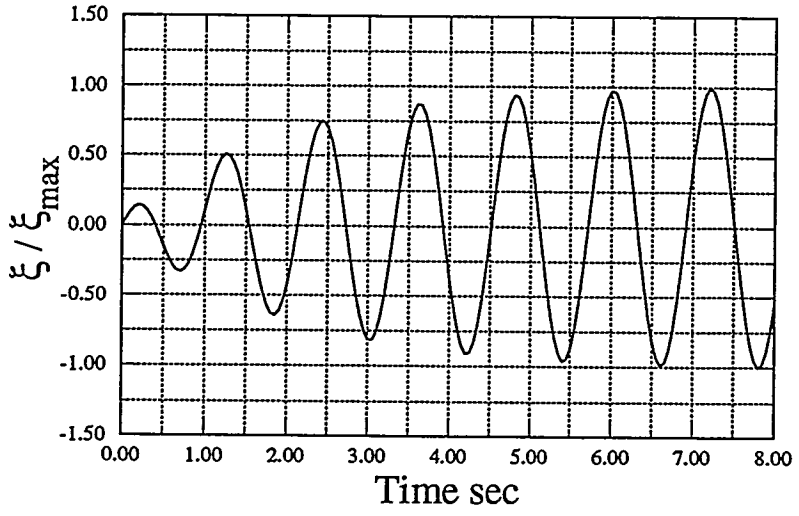

Figure 3. Normalized linear solution of the model surface wave problem as a function of time for $\omega = 5.7120$, $\mu = 0.5314$, $x = -0.45$, and $y = 0.0$.

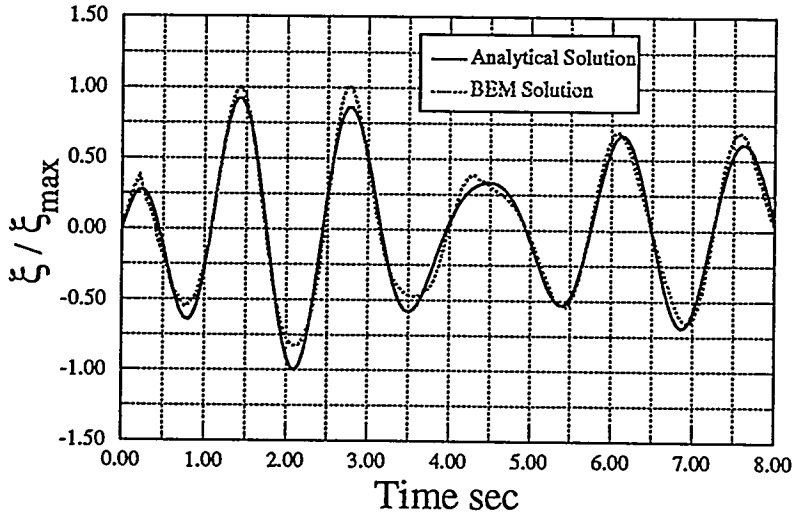

Figure 4. Comparison of the normalized analytical and BEM solutions to the model surface wave problem as a function of time for $\omega = 3.9270$, $\mu = 0.5314$, $x = -0.45$, and $y = 0.0$.

References

1. Baty, R. S., "Sloshing Frequencies in Cylindrical Containers," Memo to R. D. Robinett, 9816, Sand National Laboratories, June, 1994.

2. Romero, V. J., "HSLOSH: A Computer Code for Modeling Transient 2-D Sloshing of a Pseudo-Viscous Liquid in a Horizontally Oscillating Container," Memo to R. D. Robinett, 9816, Sandia National Laboratories, November, 1994.

3. Faltinsen, O. M., 1978, *A Numerical Nonlinear Method of Sloshing in Tanks with Two-Dimensional Flow*, Journal of Ship Research, 22, No. 3, pp. 193-202.

4. Currie, I. G., 1974, **Fundamental Mechanics of Fluids**, McGraw-Hill, Inc.

5. Kreyszig, E., 1979, **Advanced Engineering Mathematics, 4th Ed.**, John Wiley & Sons.

Distribution

MS 0835	1513	R. D. Skocypec
MS 0825	1515	W. H. Rutledge
MS 0825	1515	R. S. Baty
MS 0949	2111	J. T. Feddema
MS 0310	9816	R. D. Robinett

Appendix D

Vicente J. Romero

Experimental Validation of HVPSlosh An Extension of HSLOSH for Modeling Sloshing of a Pseudo-Viscous Liquid in Containers Experiencing Horizontal, Vertical, and Pitching Motions

Intentionally Left Blank

Sandia National Laboratories
Albuquerque, New Mexico 87185

date: September 7, 1995

to: John T. Feddema, 2111 (MS 0949)

from: Vicente J. Romero, 1513 (MS 0835)

subject: Experimental validation of HVPSLOSH (an extension of HSLOSH for modeling sloshing of pseudo-viscous liquids in containers experiencing horizontal, vertical, and pitching motions)

EXECUTIVE SUMMARY

It is desirable to model the action of fluids in robotically moved containers to help prescribe robotic manipulations that minimize sloshing and maximize work speed. A previous memo [1] described a mathematical model for simulating the 2-D sloshing of pseudo-viscous liquids in horizontally moving rectangular containers and presented results of a nonlinear test problem that lent credibility to the model. The model has recently been extended for application to arbitrarily shaped containers experiencing essentially arbitrary combinations of horizontal, vertical, and angular pitching motions in the modeling plane. In this memo the results of several 2-D simulations are compared against experimentally generated 3-D data in an effort to validate the model.

The model appears to predict sloshing frequency quite well for any type of bowl motion or geometry. The initial amplitudes resulting from forced bowl maneuvers are considerably overpredicted by the model, the predictions generally getting worst as the maneuver becomes more extreme. As a partial remedy, adding surface tension to the model would have a correcting effect on these errors while not impacting sloshing frequency appreciably. A Rayleigh damping coefficient of μ=0.55/sec. results in significantly greater damping rates than experimental data exhibits, though this can be easily corrected to large measure (without significantly altering the other characteristics of the fluid response) by decreasing μ. Finally, appreciable uncertainty exists in the experimental data due to the substantial drift errors and hysteresis effects evident in the sensor responses. Though considerable differences sometimes exist between simulation and experiment, the results here are still encouraging considering that the 2-D model is being used to estimate 3-D sloshing behavior and large potential exists to better reconcile measurements with predictions by adding, changing, and correcting factors in the model and experiments.

BACKGROUND

Reference [1] describes a computer model for simulating the transient fully nonlinear behavior of pseudo-viscous fluids residing in 2-D horizontally moving rectangular containers. The effects of viscosity are approximated by imparting Rayleigh damping to a potential-flow model of the fluid. A boundary element approach is used to efficiently handle

the changing fluid geometry, and Lagrangian node movement at the free surface allows for violent sloshing of the liquid. In [1] the model problem of a horizontally oscillating rectangular container was simulated and compared against other numerical simulations in the literature and appeared to be more accurate. In [2] the simulation results of a more linear problem (having only small amplitude waves on the free surface) were compared against an exact linear solution with very favorable results. Since then, several experiments have been performed ([3]-[6]) in which the nonlinear 3-D sloshing of water in various shaped bowls has been measured. I here compare simulation results from the 2-D numerical model against the 3-D experimental data to establish a quantitative characterization of the predictive capability of the 2-D model in 3-D settings.

MODEL VALIDATION AGAINST EXPERIMENTAL DATA

1. Comparison Against Hemispherical Bowl Slosh Data

Reference [5] describes the tests undertaken to characterize the sloshing of water in a hemispherical bowl subjected to three different horizontal acceleration profiles. Briefly, a 9.25 inch diameter hemispherical bowl filled with water to a resting depth of 3.2 inches was accelerated horizontally from rest to a constant translational velocity and then decelerated to a stop. In all three cases the straight-line maneuvers covered a distance of 0.252 meters and had a similar character, but the times of the maneuvers varied from 3.752 seconds to 2.912 seconds to 2.072 seconds, so that accelerations and velocities were successively higher for each maneuver. Water displacement data (slosh data) was recorded through about 30 seconds after the completion of the maneuvers so that the settling behavior of the liquid could also be characterized. More details about the maneuvers and experimental setup and procedures can be found in [5].

Slosh data for the hemispherical bowl is measured in terms of displacement angles as indicated in Figure 1. We note that the positive sense of the displacement angles in the figure is an intuitive convention in that, at either side of the container, water rising up the side of the bowl from the rest

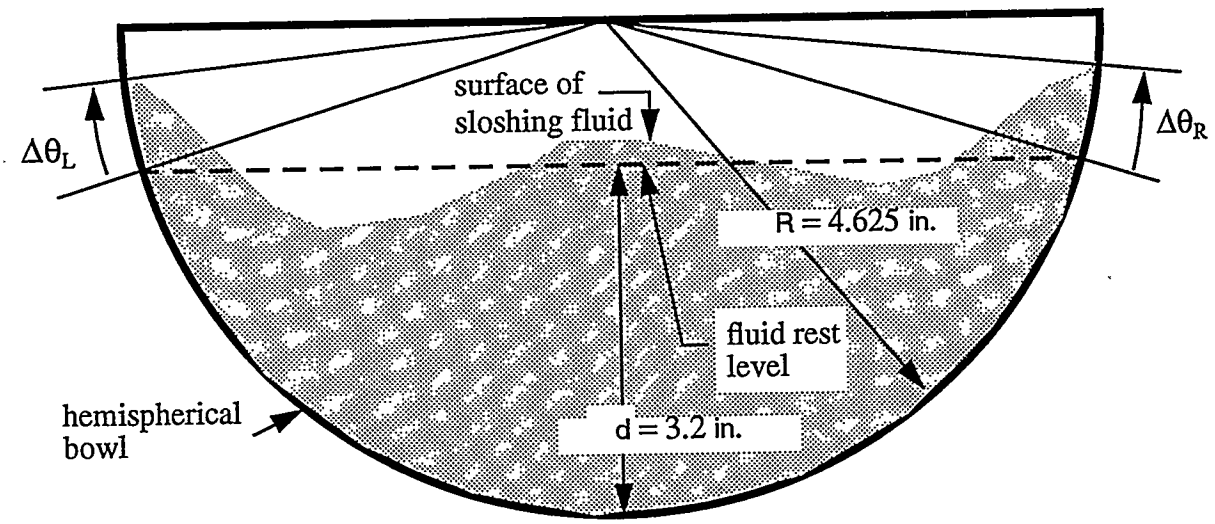

Figure 1: Geometry and conventions for hemispherical bowl sloshing simulations

position produces a positive displacement angle and water falling below the rest position implies a negative displacement angle. Thus, the displacement angle at the left side of the container is measured positive clockwise and the displacement angle at the right side of the container is measured positive counter-clockwise. This convention is opposite to that of the experimental data. Therefore, in the following, the experimental data has been reconciled with the above convention by transforming the displacement angles to the negative of their original values.

It is important to keep in mind that in the following we are comparing 2-D simulation results for sloshing in an infinitely long cylindrical trough against 3-D sloshing in a spherical bowl. Thus, we immediately expect that large discrepancies might exist, but nevertheless we seek a quantitative characterization of the discrepancies between the idealized 2-D model and actual 3-D behavior.

It will be noticed that the following simulations all terminate around 13 seconds after initiation of the maneuvers. In all cases the adaptive Runge-Kutta time-marching package terminated the simulations with a message that the governing system of ODEs had become too stiff to be cost effectively time-marched with the R-K integrator. Rather than looking further into the issue (this is probably due to the fact that the free surface was essentially devoid of motion everywhere but at the edges where it meets the bowl) or switching to a stiff ODE solver, it was determined that the simulations were of ample duration to allow valid comparisons to be made. The 13 second simulations each took about 50 minutes of CPU time on a SUNSparc20/60mhz workstation.

1.1 Trajectory 1 (3.752 sec. maneuver)

Figure 2 shows for Maneuver 1 the experimental and predicted angular displacement histories of the fluid at the trailing edge of the vessel. Figure 3 shows analogous data at the leading edge. A Rayleigh damping coefficient of μ=0.55/sec was used in the simulations. (The Rayleigh damping coefficient is the only adjustable parameter in the model except for numerical/computational parameters such as the number of boundary elements used and the time-step size.) Comparing the top two plots in each figure, it is immediately apparent that the model qualitatively matches the experimental data quite well. More quantitative comparisons can be made by viewing the comparison plots at the bottom of the figures.

Sloshing Amplitudes

Accounting for the drift in the experimental data (updrift for trailing edge data and downdrift for leading edge data), it is estimated that the predicted amplitudes exceed the experimental ones by up to 30%, but are generally only 5% to 15% larger.

Another measure of the applicability of the model is the predicted decay rate of the fluid motion. Decay rate can be roughly quantified in terms of a "damping ratio" as defined in [3]. The calculated damping ratio for the simulated "settling" response over the time span from the completion of bowl motion at 3.752 seconds to the end of the simulation at 13.248 seconds is calculated as follows for data at the trailing edge:

$$\zeta_{troughs} = \frac{\ln\left(\frac{\Delta\theta|_{trough\,\#a}}{\Delta\theta|_{trough\,\#b}}\right)}{2\pi\,(b - a)} = \frac{\ln\left(\frac{-2.965}{-0.533}\right)}{2\pi\,(14)} = 0.0195.$$

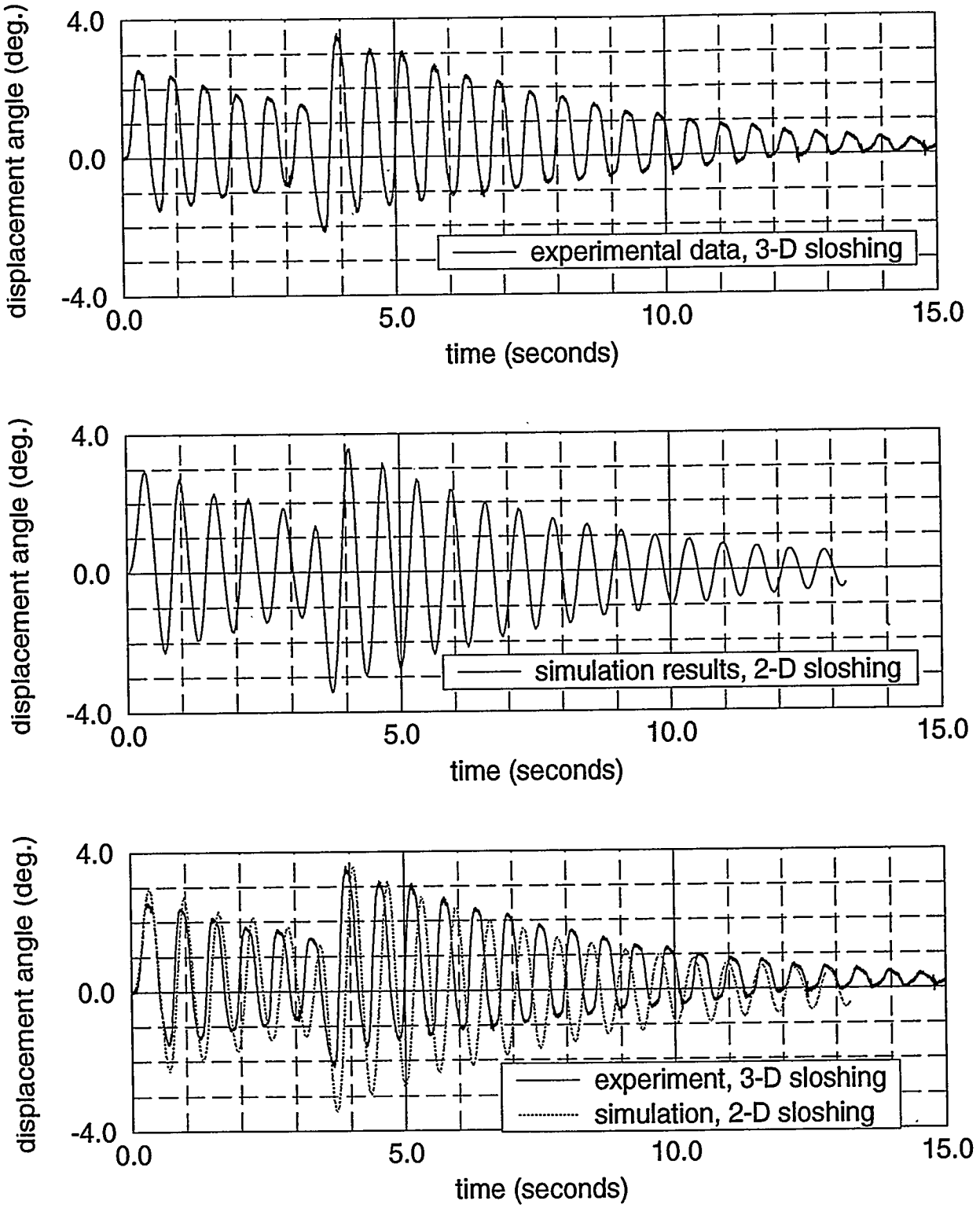

Figure 2: Experimental and predicted angular displacement histories at the trailing edge of the hemispherical bowl for Trajectory 1

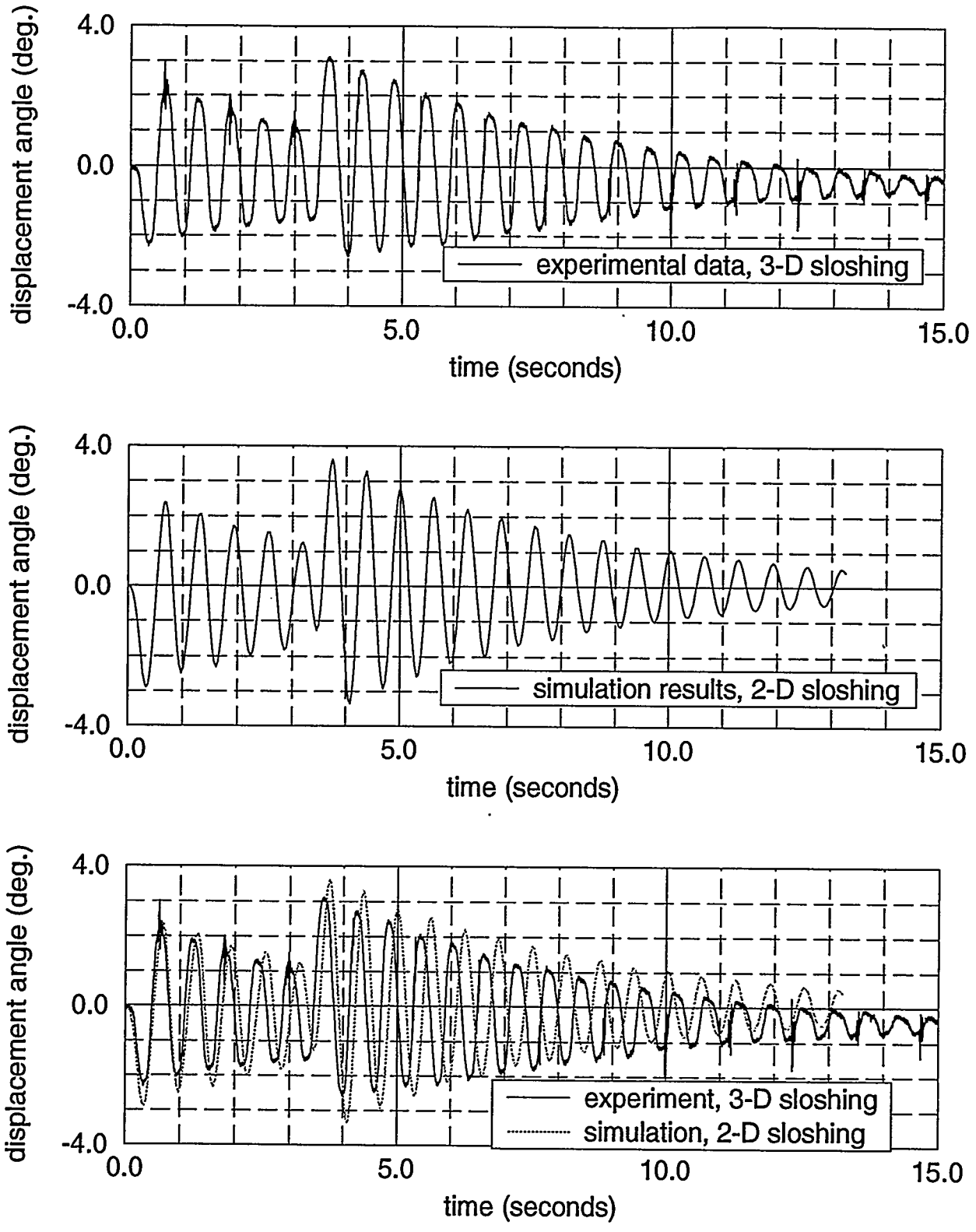

Figure 3: Experimental and predicted angular displacement histories at the leading edge of the hemispherical bowl for Trajectory 1

This value roughly coincides with the experimentally derived values given in [3] of 0.0084 for the first 15 seconds after completion of the maneuver and 0.0132 for the 10-25 sec. time-window after maneuver completion.

Similarly, for simulation data at the leading edge,

$$\zeta_{troughs} = \frac{\ln\left(\frac{-3.339}{-0.517}\right)}{2\pi\,(14)} = 0.0212$$

This value compares with the experimentally derived values given in [3] of 0.0083 for the first 15 seconds after completion of the maneuver and 0.0145 for the 10-25 sec. window.

Though the agreement between predicted and experimentally obtained damping ratios is not particularly good, it is also not so bad that it invalidates the model: It will be shown later that decreasing the Rayleigh damping coefficient in the simulations decreases the predicted damping ratios significantly while only marginally increasing initial amplitudes. Moreover, the experimental damping ratios derived in [3] are themselves uncertain, as they arose from one of the first experiments performed, and several improvements were made in the experimental methodology thereafter. In addition, the time window over which the damping ratio is computed has a substantial impact on the ultimate value. Better standards to compare against would come from processing the experimental data in Figures 2 and 3 to remove the drift and anomalous spikes and oscillations and calculating damping ratios over the same time windows as used in the calculations above.

For completeness, the damping ratio for the peaks during simulated settling are

$$\zeta_{peaks} = \frac{\ln\left(\frac{\Delta\theta|_{peak\,\#a}}{\Delta\theta|_{peak\,\#b}}\right)}{2\pi\,(b-a)} = \frac{\ln\left(\frac{3.56}{0.534}\right)}{2\pi\,(14)} = 0.0216\text{, trailing edge,}$$

and

$$\zeta_{peaks} = \frac{\ln\left(\frac{3.276}{0.536}\right)}{2\pi\,(14)} = 0.0206\text{, leading edge.}$$

These numbers are close to the damping ratios calculated for troughs.

In iterating to find a reasonable value of μ, the 0.55/sec. value seems to yield a good compromise between initial amplitude size and decay within the resolution of the unconditioned experimental data. However, a better value could be obtained in the following manner after conditioning the data as described above. Ratios of successive amplitudes can be plotted as a function of time. The plot is then matched as closely as possible (the initial amplitude and the frequency are relatively insensitive to μ as will be seen later, so don't have to be considered) by iterating over the damping coefficient or even constructing an appropriate profile for varying the coefficient over time.

Sloshing Frequency

Sloshing frequency is another metric of model applicability. Figures 2 and 3 show that sloshing frequency appears to be fairly steady in time for both experimental and model-generated data. Figures 4 and 5 plot the peak-to-peak and trough-to-trough time periods vs. peak pair and trough pair for the simulated sloshing. It is seen in all cases that the sloshing period is relatively steady with time, no overall upward or downward trends being evident in the data. For data at the leading edge of the bowl the mean period measured in the troughs is 0.626 sec. with a standard deviation of 2.33% (as a percentage of the corresponding mean value). The mean period measured in the peaks is 0.625 sec. with a standard deviation of 4.13%. For data at the trailing edge the mean trough period is 0.625 sec. with a standard deviation of 4.65% and the mean peak period is 0.626 sec. with a standard deviation of 2.33%. Thus, not only are there no discernable tendencies for the sloshing frequency to increase or decrease over time, there is also very little scatter in the frequencies. Therefore, it is appropriate to speak of a single average characteristic "natural" sloshing period for the situation at hand, which our model suggests is 0.625 seconds. The corresponding natural frequency is 1.6 Hz. (For confirmation, a simulation was run involving the same geometry and depth of fluid with the free surface initially linearly displaced 4 degrees from the horizontal and the fluid allowed to settle in the stationary bowl. The average natural frequency for this numerical experiment was 1.59 Hz [with a time-averaged damping ratio of 0.0206]).

The comparison plots at the bottom of Figures 2 and 3 show that the actual fluid sloshes once more than does the simulated fluid in the first 12.54 seconds (the leading edge peaks and trailing edge troughs for the experimental and simulated data come in phase at t=12.54 seconds). During this time the actual fluid experiences 21 full cycles whereas the simulated fluid experiences 20 full cycles. Multiplying the simulated frequency of 1.6 Hz by this ratio we compute the average actual sloshing frequency to be 1.68 Hz, with a corresponding actual period of 0.595 seconds. The simulated sloshing frequency is 4.8% less than the experimental frequency and 4.2% less than the experimental value of 1.67 Hz reported in [3]. However, despite the close agreement in sloshing frequency, phase accuracy can be soon lost in the simulation as is evident in the comparison plots at the bottom of Figures 2 and 3..

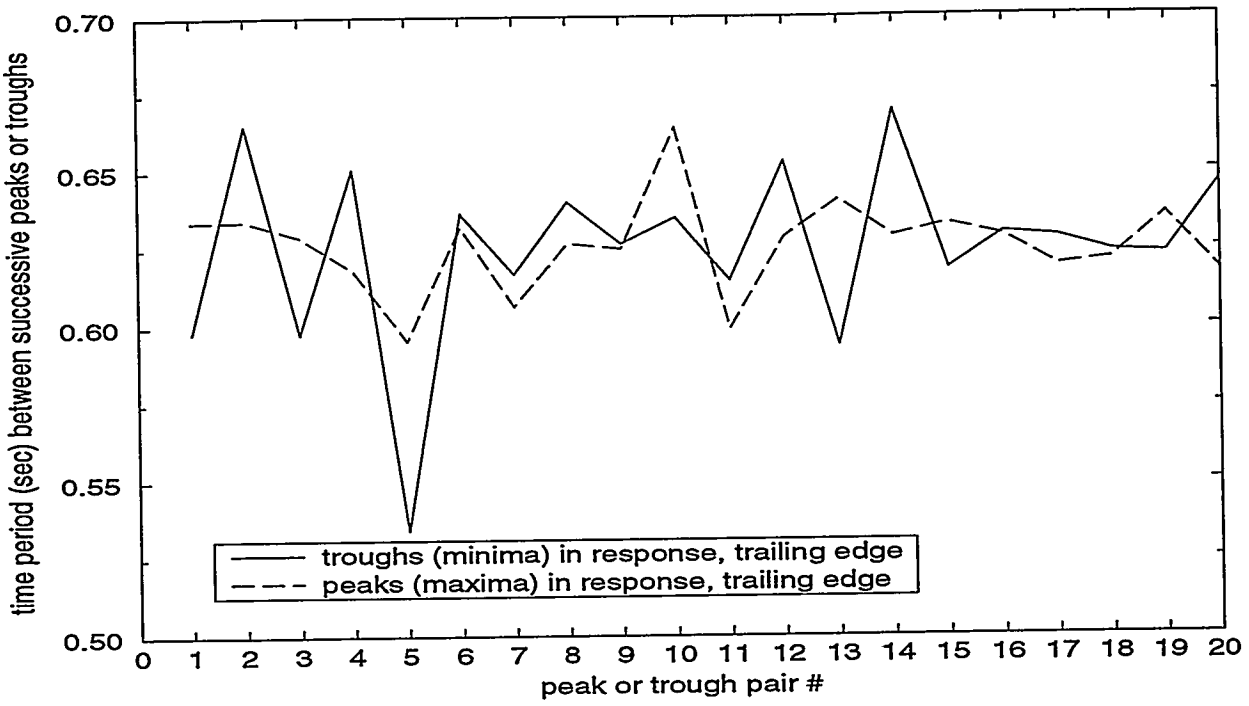

Figure 4: Variation in undulation period over time at trailing edge of hemispherical bowl for Trajectory 1

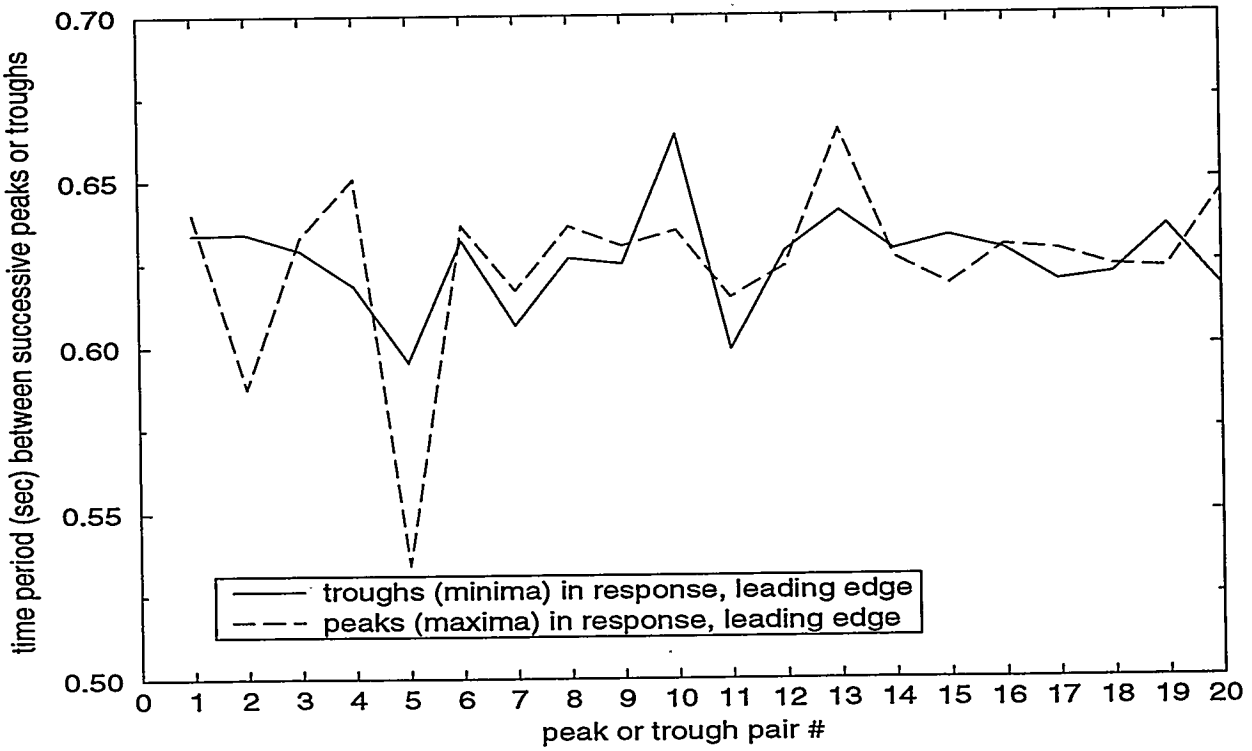

Figure 5: Variation in undulation period over time at leading edge of hemispherical bowl for Trajectory 1

Sensitivity of Results to Damping Coefficient

Given that we are trying to match 3-D behavior with a 2-D model, the results thus far have been fairly encouraging. As mentioned above, measures may be taken to improve on the approximation by obtaining a more representative value for μ or by using a time-varying value. A simple sensitivity study was run to determine the effect of μ on sloshing frequency, initial amplitude, and decay rate. Figure 6 plots a baseline response indicator for $\mu_b = 0.55$/sec. against results for 1/3 higher ($4\mu_b/3$) and 1/3 lower ($2\mu_b/3$) damping coefficients. It is seen that, in the neighborhood of $\mu = 0.55$/sec., the Rayleigh coefficient has very little effect on frequency and initial amplitude. This may also true for the rate of amplitude decay, but the compounding effect of the decay rate makes amplitudes increasingly sensitive to this value as time increases. Moreover, it appears that the coefficient has a highly nonlinear effect on decay rate, as the amplitude deviations from the baseline are significantly greater when the coefficient is 1/3 lower than μ_b vs. when the coefficient is 1/3 higher. Thus, the adjustable parameter μ has most effect on the long-time amplitudes of the sloshing.

Assessment

Given our findings and the experimental data in Figures 2 and 3, an optimal damping coefficient probably exists somewhere in between the extremes of μ_b and $4\mu_b/3$. However, the experimental data would have to be properly conditioned before it would make sense to expend any more work in optimizing μ. It suffices here to say that the fairly good agreement in Figures 2 and 3 can be made better (in terms of closer amplitudes at longer times) with a bit more effort. Quantitatively, significant differences do exist, but in view of the level of approximation involved, principally the approximation of 3-D behavior with a 2-D model, the results are still quite encouraging for this relatively gentle horizontal maneuver.

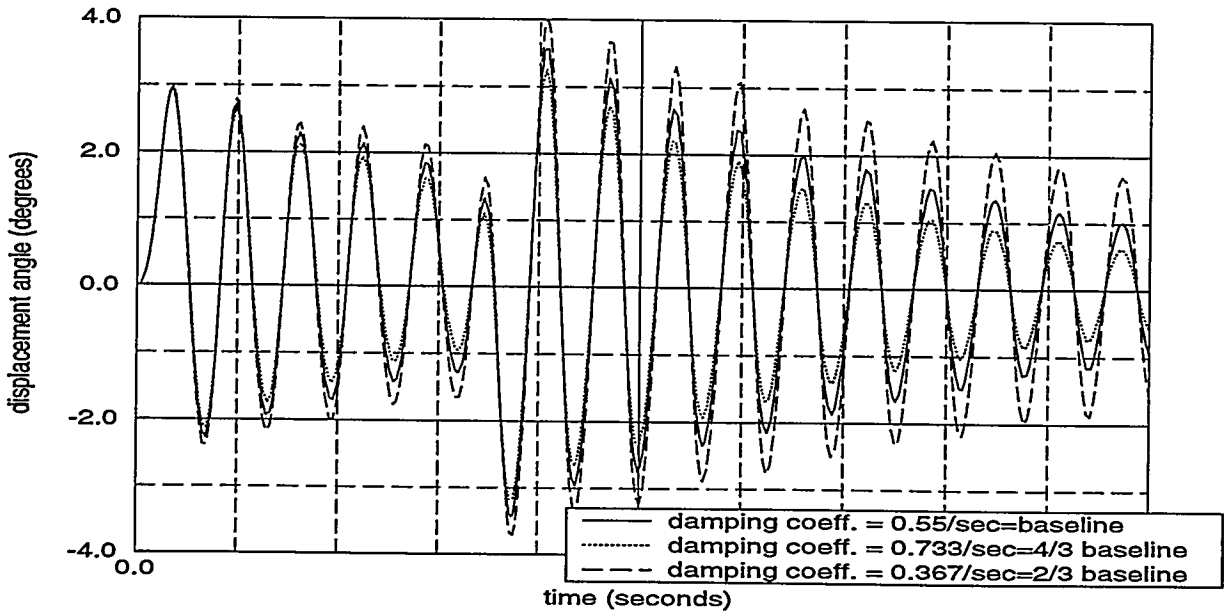

Figure 6: Effect of Rayleigh damping coefficient μ on sloshing response at trailing edge of hemispherical bowl for Trajectory 1

1.2 Trajectory 2 (2.912 sec. maneuver)

Analysis

Figures 7 and 8 show for Maneuver 2 the experimental and predicted angular displacement histories of the fluid at respectively the trailing and leading edges of the vessel. For the most part the model duplicates the experimental data reasonably well in both frequency and amplitude during the first ~5/6 of the maneuver. During this time, amplitude errors seem to be only slightly larger than for Maneuver 1. Near the conclusion of the maneuver, however, the model exhibits an anomolous sloshing mode beginning at approximately t=2.6 seconds that causes the amplitudes of the predicted response to depart dramatically (as much as ~ 400% in one place) thereafter from the experimental data. This corresponds to a strange predicted frequency disturbance, in which the prevailing predicted frequency seems to either increase or decrease by about 1/2 during the approximately 2.6 sec. - 3.2 sec. time window and then return to its previous value thereafter: where [as occurs in the experiment] a single complete slosh cycle would normally occur in this time (the prevailing predicted period being a fairly steady ~ 0.6 sec. before and after this time window), the model produces what can be construed either as a slightly disturbed half cycle or $1\frac{1}{2}$ weakly distinguishable cycles. The cause of the disturbance seems to be precipitated by the beginning of the deceleration process, which starts at about t=2.5 seconds, and apparently initiates some type of resonant interaction due to a coincidence in the time-phasing of the fluid and container motions. The way to test this hypothesis is to rerun the simulation with shifted starting times for the decelaration process to see if the anomolous behavior is "real", *i.e.* stable with respect to small perturbations in the initiation of deceleration, or is indeed the result of a coincidence.

Assessment

If the anomolous behavior is coincidental, then the model might in general be much more suitable than Figures 7 and 8 seem to indicate. If not a coincidence, then the differences between 2-D and 3-D behavior might be showing up in a more pronounced way for this more extreme (than Trajectory 1) maneuver, and whether this is the explanation or not, the range of applicability of the model would seem to be limited to fairly gentle maneuvers.

1.3 Trajectory 3 (2.072 sec. maneuver)

Analysis

Figures 9 and 10 show for Maneuver 3 the experimental and predicted angular displacement histories of the fluid at respectively the trailing and leading edges of the vessel. Early amplitude errors are greater than for maneuvers 1 and 2, at times reaching differences upwards of 200% at the trailing edge, though some of the error appears to be due to sensor drift, and generally errors are much less, especially at the leading edge. In any case, the predicted amplitudes at late times match the experimental data very well. The frequency prediction, as for Maneuver 1, is quite good. Figure 11 shows the time variation in sloshing period as measured by peak-to-peak and trough-to-trough time intervals at both leading and trailing edges of the container. A slight downward trend is evident in sloshing period during container motion, with subsequent leveling off of the trend after motion stops. Oscillations about the average period of 0.632 sec. (avg. frequency = 1.58 Hz) over the 13.5 second simulation are relatively small, with the most variation occuring for trough periods at the leading edge where a standard deviation of 5.7% from the mean exists. By counting

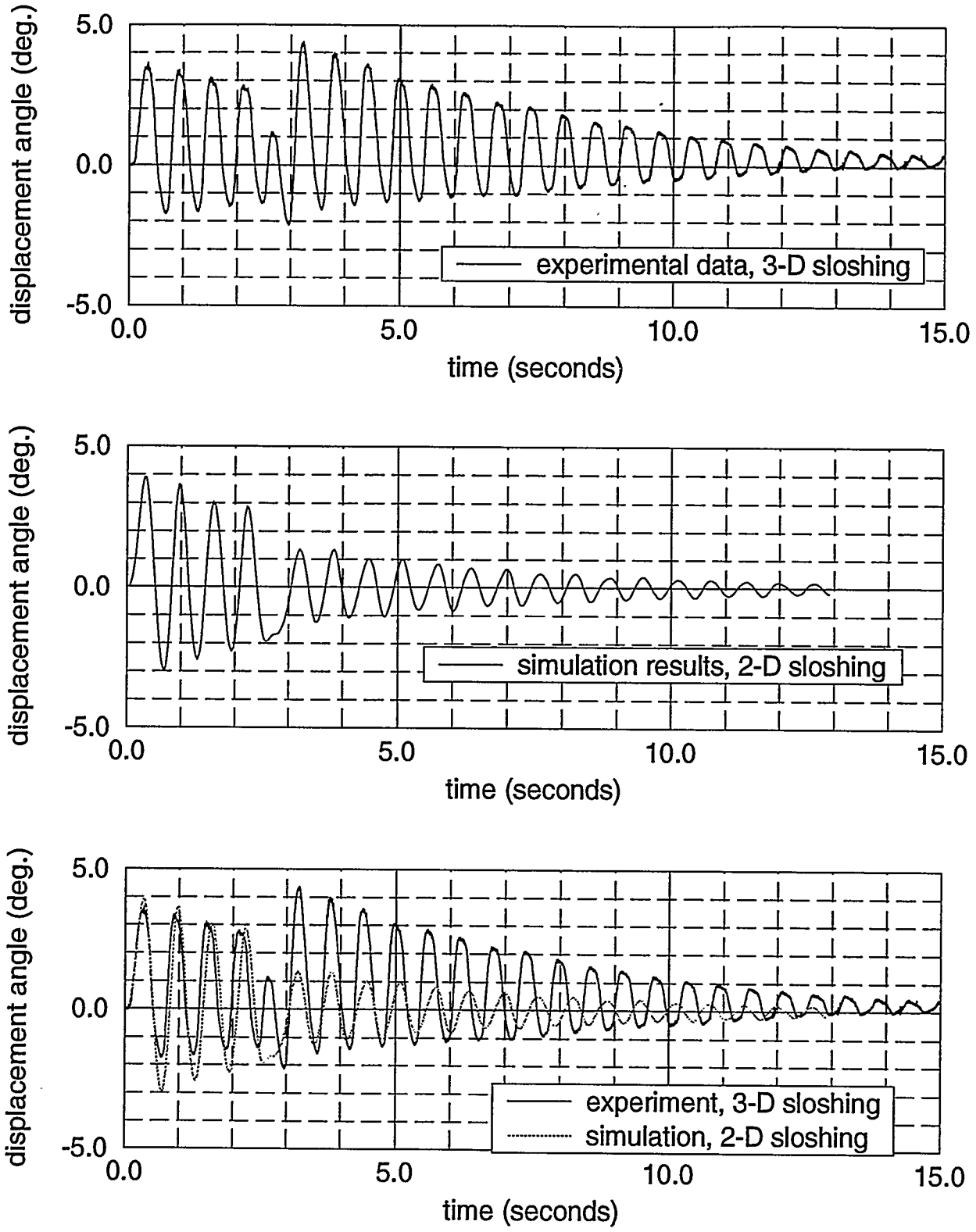

Figure 7: Experimental and predicted angular displacement histories at the trailing edge of the hemispherical bowl for Trajectory 2

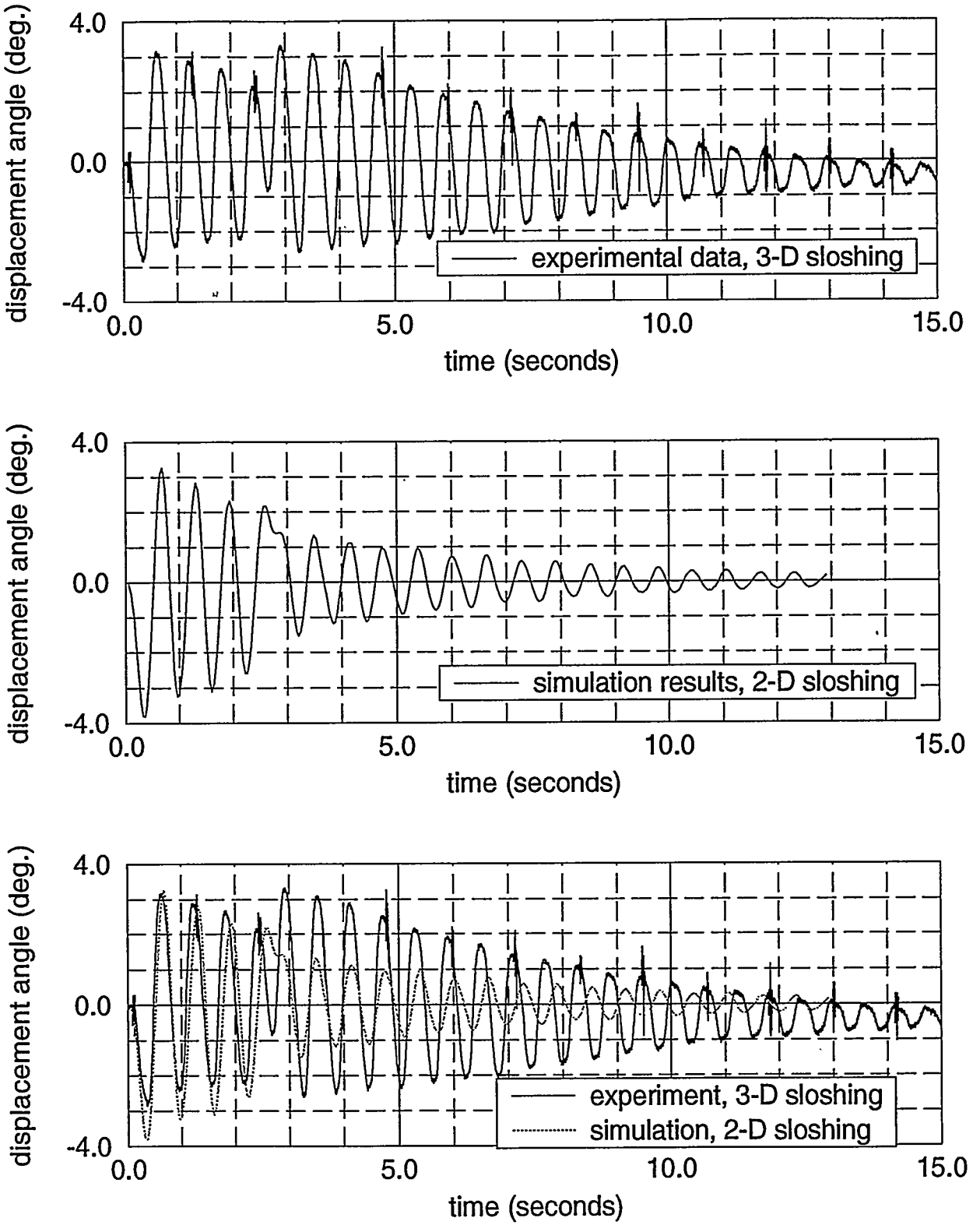

Figure 8: Experimental and predicted angular displacement histories at the leading edge of the hemispherical bowl for Trajectory 2

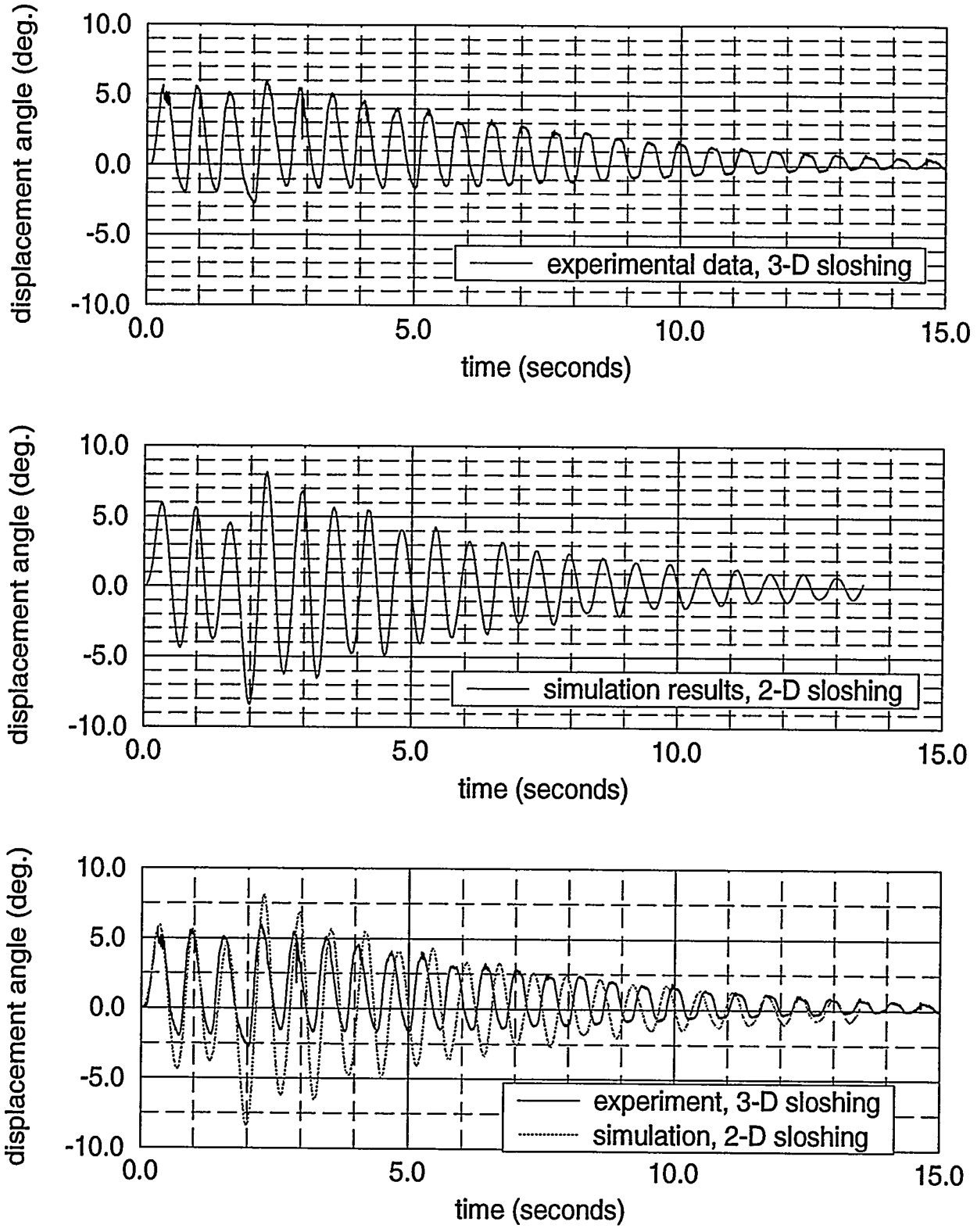

Figure 9: Experimental and predicted angular displacement histories at the trailing edge of the hemispherical bowl for Trajectory 3

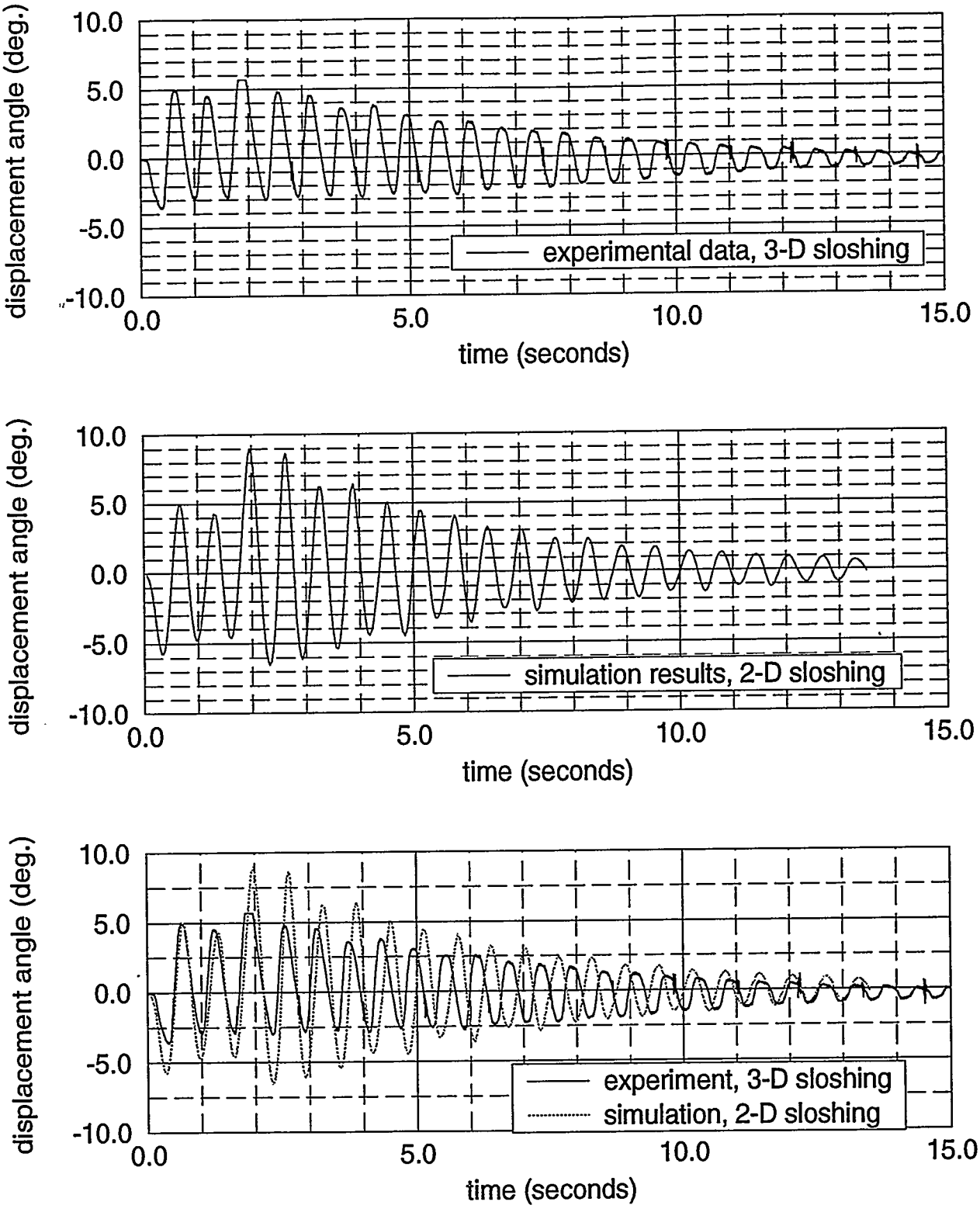

Figure 10: Experimental and predicted angular displacement histories at the leading edge of the hemispherical bowl for Trajectory 3

the number of experimental and simulated periods between the bounding early and late times where the phases match up, the average experimental frequency is calculated to be 19/18 to 20/19 of the average simulation frequency. This turns out to be a mean experimental frequency of about 1.66 Hz. Thus, as expected, predicted and experimental sloshing frequencies for this maneuver are essentially the same as for Maneuver 1, especially during settling when no forcing motion exists.

Assessment

Unlike for the second maneuver, the simulation results for Maneuver 3 are characteristic of the actual data. This is the case even though Maneuver 3 is more "extreme" (faster, producing larger sloshing amplitudes) than Maneuver 2. This supports the proposition that some type of phase interaction is taking place in the Maneuver 2 simulation, rather than a general incompatability arising between 3-D behavior and the 2-D model as the maneuver intensifies. Still, significant degradation of the approximation does occur for amplitude prediction as the maneuver intensifies, and though frequency prediction does not degrade, even small errors soon compound to destroy absolute phase accuracy.

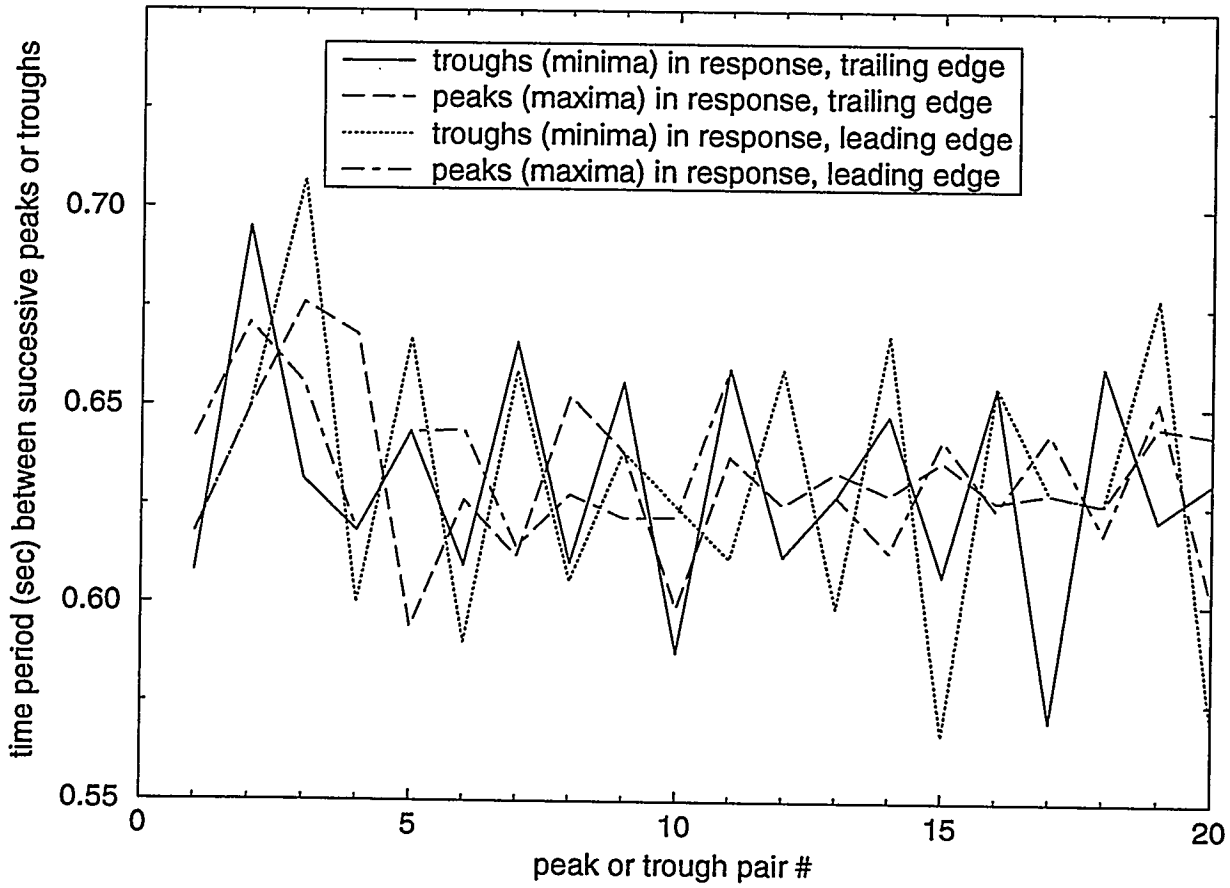

Figure 11: Variation in undulation period over time at edges of hemispherical bowl for Trajectory 3

2. Comparison Against Experimental Slosh Frequency for "Trapezoidal" Bowl

Figure 12 shows a diametral cross section of a circular bowl that was used in a horizontal translation experiment like above for the spherical bowl. The bowl was filled with water to the indicated depth. The model approximates the axisymmetric bowl as a 2-D trapezoidal trough of infinitely long extent having the cross section shown in the figure. Reference [6] documents the details of the experiment. Data is only available during the settling of the water after completion of bowl translation. Reference [6] derives two metrics of the slosh motion from the ~ 10 seconds of useful data collected by sensor 1 at the leading (right) edge of the bowl: an average sloshing period of 0.435 seconds[1] and an average damping ratio of 0.0172 for the peaks of the fluid motion. Because the exact trajectory used in the experiment is not available for input to the model and these metrics are based upon slosh motion during settling (unforced) motion of the liquid, comparable model data can be generated by displacing the surface from its rest position and allowing the fluid to settle in the stationary trough. Accordingly, a numerical simulation was run in which the initial condition was a straight free surface displaced 0.5 cm. down from rest position at left side of the trough and 0.5 cm up at the right side. The results of the simulation are shown in Figure 13. The average peak-to-peak and trough-to-trough period over the 18 full periods of the 10 second simulation is 0.510 sec. at the leading or right end of the trough. This value is about 17% longer than in the experiment. The average damping ratio for the troughs of the fluid motion at the right end of the container is 0.020, which is about 16% greater than the experimental ratio.

The simulated fluid response does not agree with the experimentally measured response for the trapezoidal bowl as well as it does for the spherical bowl. This could be principally caused by

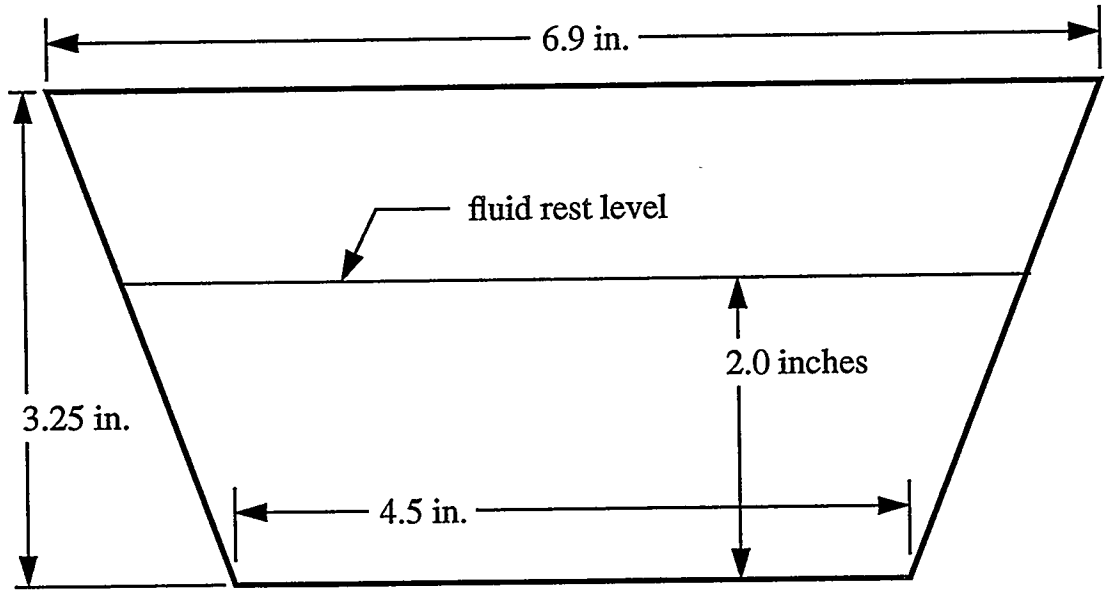

Figure 12: Approximated diametral cross section of "trapezoidal" bowl

1. This number reflects a correction to [6] from the stated formula for frequency, $\omega = \frac{2\pi}{\Delta time}$, to the correct formula $\omega = \frac{1}{\Delta time}$.

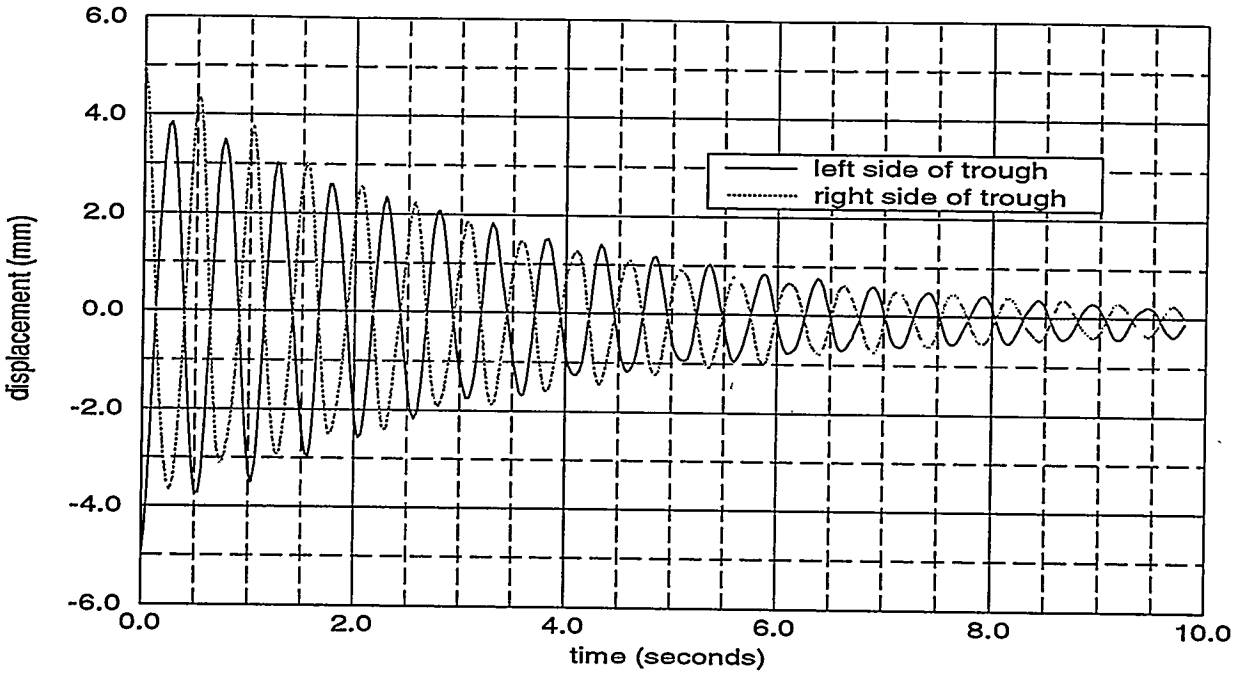

Figure 13: Predicted free-surface displacement from rest level at right and left sides of trapezoidal bowl for initial linear displacment of free surface

the 2-D/3-D discrepancy already mentioned and by geometric approximations, as the trough does not reflect the well rounded corners and slightly curved sides of the actual bowl cross section. Though the agreement here is certainly not spectacular, it is still reasonable given the approximations involved and the uncertainty in the experimental data itself in this first experiment. Additionally, a Rayleigh damping coefficient of μ=0.55/sec. was used in the simulation, which is a good estimate for the actual best coefficient for the spherical bowl, but may not be as appropriate for the trapezoidal bowl. In any case, some improvement, especially in the agreement between the damping ratios, can undoubtedly be obtained by adjusting μ.

SUMMARY AND CONCLUSIONS

HVPSLOSH is an extension of HSLOSH [1] for modeling incompressible, irrotational, pseudo-viscous free-surface fluids being transported in arbitrarily shaped containers subjected to essentially arbitrary motions in the plane of the 2-D model. The approach taken for model validation against experiments has been to arrive via *ad hoc* iterative means to a close-to-optimal Rayleigh damping coefficient for one set of experimental data, and then to assess the performance of the model against other data sets using this same damping value. Though an optimal coefficient could be obtained with the use of formal optimization on better conditioned experimental data, and the coefficient could be allowed to change over time and with each different container and maneuver, the model is most usable if not inordinately dependendent on a "correct" value for this parameter. Thus, the approach taken investigates the robustness of the model as well as its potential to match experimental data under a given set of conditions.

With a damping coefficient of μ=0.55/sec. the model matched experimental results of Trajectory 1 (the slowest maneuver) with the hemispherical bowl to within 5% for average sloshing frequency, to within 30% for initial sloshing amplitude, and to within 48% for average damping rate. A quick sensitivity study revealed that only the damping rate is sensitive to μ, which indicates that the damping rate can be brought much closer to the experimental one without degrading the other characteristics of the predicted response. For Trajectory 2 an anomolous frequency and amplitude disturbance occurs in the simulation, but not in the experiment. The onset of the disturbance seems to be triggered by a coincidence in time-phasing between initiation of deceleration of the bowl and the fluid motion (which has a significantly different phase than the experimental data at that time). The origin of the disturbance, which causes a poor match between prediction and experiment after this time, must be investigated more closely before conclusions can be made regarding the effectiveness of the model under Trajectory 2 conditions. For Trajectory 3 (the fastest maneuver) the model matches sloshing frequency within 5% but produces amplitude errors upwards of 200% at one point in time, though generally much less at other times, as the late-time amplitudes agree very well with experimental data. For the trapezoidal bowl fairly good concurrence exists between simulation and experiment, as the model predicts a sloshing period approximately 17% longer and an average damping ratio about 16% greater than experimental data exhibits.

Considering that the 2-D model is being used to estimate 3-D sloshing behavior, the model appears to predict sloshing frequency quite well for any type of bowl motion or geometry. However, even small errors quickly compound to destroy absolute phase accuracy after early times in the simulations. The initial amplitudes resulting from forced bowl maneuvers are considerably overpredicted by the model, the predictions generally getting worst as the maneuver becomes more extreme. As a partial remedy, adding surface tension to the model would decrease initial amplitudes while not impacting sloshing frequency appreciably. A Rayleigh damping coefficient of μ=0.55/sec. results in significantly greater damping rates than experimental data exhibits, though this can be easily corrected to large measure (without significantly altering the other characteristics of the fluid response) by decreasing μ. Finally, it should be mentioned that appreciable uncertainty exists in the experimental data due to the substantial drift errors and hysteresis effects evident in the sensor responses. These errors very probably also contribute to the discrepancies between model and experiment.

Though some very significant differences exist between simulation and experiment, the results here are still encouraging given the level of approximation involved and the large potential to better reconcile measurements with predictions by adding, changing, and correcting factors in the model and experiments.

REFERENCES

[1] Memo from V. J. Romero, 1513, to R. D. Robinett, 9811, subject: HSLOSH (a computer code for modeling transient 2-D sloshing of a pseudo-viscous liquid in a horizontally oscillating container), dated November 6, 1994.

[2] Memo from R. S. Baty, 1515, to V. J. Romero, 1513, subject: Model surface wave problem, dated November 18, 1994.

[3] Memo from D. J. Schmitt, 2111, to V. J. Romero, 1513, subject: Water slosh data, dated March 14, 1995.

[4] Memo from D. J. Schmitt, 2111, to V. J. Romero, 1513, subject: Additional water slosh data, dated April 21, 1995.

[5] Memo from D. J. Schmitt, 2111, to V. J. Romero, 1513, subject: Even more water slosh data, dated June 27, 1995.

[6] Memo from D. J. Schmitt, 2111, to V. J. Romero, 1513, subject: Slosh data for trapezoidal bowl, dated Aug. 23, 1995.

KEYWORDS: Robotics, sloshing fluids, boundary element method (BEM), code development, code validation, case 4199.100

Copy to:

MS0841	1500	P. J. Hommert
MS0828	1502	R. D. Skocypec (route to 1511)
MS0441	1503	J. H. Biffle (route to: 1517, 1518)
MS0828	1504	E. D. Gorham (route to: 1514, 1515)
MS0834	1512	A. C. Ratzel (route to 1516)
MS0835	1513	R. D. Skocypec, acting
MS0835	1513	V. J. Romero
MS0835	1513	Day File
MS0833	1515	R. S. Baty
MS0949	2111	D. J. Schmitt
MS0314	9811	R. D. Robinett

Intentionally Left Blank

Appendix E

R.C. Dykhuizen

Scaling Analysis for Molten Glass Flow (Corning CRADA)

Intentionally Left Blank

Sandia National Laboratories

Albuquerque, New Mexico 87185

date: January 11, 1995

to: John Feddema, Org. 2111, MS-0949

from: R. C. Dykhuizen, 1513

subject: Scaling analysis for molten glass flow (Corning CRADA)

Introduction and summary

Department 1513 was asked to determine the proper scaling parameters that would apply to the flow of molten glass during and after impact with the mold. This would enable estimates of how process changes would affect the glass casting. In particular, I was asked to examine how changes in the impact kinetic energy would alter the spreading of the glass on the mold. In addition, I examined how the changes in the gravitational field would alter the spreading. This would simulate the acceleration of the mold upward after the impact process.

Impact model

The conversion of the kinetic energy of impact to the spreading of a liquid drop has been studied in a number of fields. This process has applications in the following processes:

Ink jet printing
Steam turbine blade erosion by entrained water droplets
Rain erosion of terrestrial or aerodynamic surfaces
Powder production via impact atomization
Thermal spraying (impact of molten materials onto a cold substrate).

A review article will soon be available (R. C. Dykhuizen, Journal of Thermal Spray, December 1994) that covers the physics of this process. Three mechanisms limit the spreading of the liquid splat created from the impact of the liquid drop:

Surface tension
Solidification
Viscous dissipation

In almost all applications, the viscous dissipation of the droplet kinetic energy dominates, and this process limits the growth of the splat. In applications using glass, this mechanism is found to be even more dominant. Often, the work of Madejski (International Journal of Heat and Mass Transfer, 19, pp 1009-1013, 1976) is cited to define the various mechanisms.

Madejski's full mode includes all three mechanisms. His result is the splat size as a function of three dimensionless parameters that determine the relative importance of the above three processes. The Reynolds number is used to scale the viscous dissipation of the inertial forces, the Weber number is used for scaling of transformation of the kinetic energy to surface energy, and a modified Peclet number is used for scaling solidification rates.

Madejski's full model results in a complex integral-differential equation which does not have an analytic solution. Therefore, Madejski presents results in the form of numerical fits. For ex-

ample, his most quoted result is for the case where the dominant mechanism during impact is the decay of kinetic energy via viscous dissipation:

$$\frac{D}{d} = 1.2941\,(Re + 0.9517)^{0.2} \qquad Re = \frac{\rho U d}{\mu}. \tag{1}$$

The nomenclature is defined at the end of this memo along with the nominal glass property values used.

Other modelers obtain the same result, but with slightly different values for the constant. For simplicity, I will use the following:

$$\frac{D}{d} = (1 + Re)^{0.2}. \tag{2}$$

Since the impact velocity scales with the drop height, one can write the expected splat diameter as a function of the drop height. This shows that significant increases in the drop height are required to alter the splat diameter:

$$\frac{D}{d} = \left(1 + \frac{\rho d\sqrt{2gx}}{\mu}\right)^{0.2}. \tag{3}$$

Using equation 3, it is found that the splat diameter is approximately 1.2 times the drop diameter when the glass drop falls 2 meters. This increases only to a ratio of 1.3 when the drop height is doubled. The values of the parameters used are given in the Nomenclature section at the end of this memo.

A second mechanism that can limit the growth of a splat is the conversion of kinetic energy to surface energy. When this mechanism dominates, Madejski presents the following fit to his numerical results that is limited to large values of the Weber number (but still sufficiently small Weber numbers so that solidification and viscous effects are negligible):

$$\frac{D}{d} = \sqrt{We/3} \qquad We = \rho U^2 d/\sigma. \tag{4}$$

From the above equation, it is shown that a diameter ratio of 100 is predicted. This is a much larger ratio then predicted from equation 3. Thus, viscous dissipation must be more limiting than surface tension effects.

Madejski's third mechanism concerns the solidification of the splat. The formulation of this model in Madejski's paper is very complex, even though he considered materials with distinct phase changes. Trapaga and Szekely (Metall. Trans., 22B pp 901-914, 1991) have shown that the time scale of the impact process can be given as:

$$t_i = \frac{2d}{3U} Re^{0.2}. \tag{5}$$

If we accept this time scale, we find that the glass impact event is approximately 10 milliseconds in duration. In that time the thermal wave penetrates 0.1 mm into the glass from the following equation typically used to estimate conduction transients (e.g. Incropera and DeWitt, Fundamentals of Heat and Mass Transfer, 2nd. Ed., John Wiley and Sons, P 204):

$$\delta \approx \sqrt{\frac{Kt_i}{\rho C}}. \tag{6}$$

Thus, I will ignore the solidification effect on the spread of the molten glass splat during the impact process.

Further Spreading After the Impact Event

After the kinetic energy of the impact is dissipated via viscous flow, the glass splat may still flow outward by converting potential energy. Figure 1 shows how a reduction in the potential energy can be used to drive the flow.

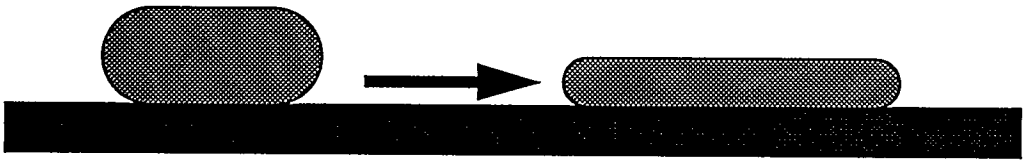

Figure 1: Conversion of potential energy to drive splat spreading

If we again assume that the solidification and surface tension effects are small, the following equation equates the rate of change of potential energy to the viscous dissipation:

$$-\left(\frac{\pi D^2 H}{4}\right)\left(\frac{\rho g}{2}\right)\frac{dH}{dt} = \left(\frac{\pi D^2}{4}\right)\left(\frac{\mu}{4H}\right)\left(\frac{dD}{dt}\right)^2. \tag{7}$$

The right hand side of equation 7 is identical to the viscous dissipation scaling derived by Madejski when he considered impacts. Since the splat height can be related to the splat diameter through the splat volume (which is constant):

$$V = \frac{\pi H D^2}{4}, \tag{8}$$

equation 7 can be transformed to a first order differential equation. If we fix the viscosity at its initial value (it will increase as the splat cools), the solution is easily obtained:

$$\frac{D}{D_0} = \sqrt[8]{1 + \frac{2^{11}\rho g V^3 t}{\mu \pi^3 D_o^8}}. \tag{9}$$

For short times (less than 0.05 seconds), the solution may be approximated as:

$$\frac{D}{D_o} \approx 1 + \frac{2^8 \rho g V^3 t}{\mu \pi^3 D_o^8} \tag{10}$$

and for long times (greater than 0.05 seconds), the solution may be approximated as:

$$\frac{D}{D_o} \approx \sqrt[8]{\frac{2^{11} \rho g V^3 t}{\mu \pi^3 D_o^8}} \tag{11}$$

The above solutions show that increases in the gravitational field will have minimal effects on the growth of the splat. Doubling the gravitational force will have the same effect as halving the viscosity.

From equation 6, the thermal wave has penetrated 0.2 mm when the second term under the radical in equation 9 becomes unity (0.05 seconds). At this point the diameter ratio in equation 9 is 1.09. After this time the spreading occurs at a much slower rate as indicated by equation 11. In reality, the rate will be slower still due to the increased viscosity that results from the colder glass. (The increased viscosity was ignored in deriving equations 9 through 11.)

Conclusions

In this memo the scaling laws for splat spreading are presented as applied to a high viscosity molten glass. It is shown that the spreading is minimal for the impact velocities that are typical in the Corning process.

Further spreading after impact is slow due to the large viscosity of the melt. Scaling equations show that increasing the gravitational force would have minimal impact on the spreading velocity. The effect of surface tension and solidification (large increases in viscosity in the case of molten glass) will eventually stop the spread of the splat. However, these effects are small at early times, and thus has been ignored in this analysis.

Keywords: thermal sciences, 4199.100 (Corning CRADA)

Distribution:

MS0828 1502	P. J. Hommert (route to: 1511)
MS0441 1503	J. H. Biffle (route to: 1517, 1518)
MS0828 1504	E. D. Gorham (route to: 1514)
MS0834 1512	A. C. Ratzel (route to: 1516)
MS0835 1513	R. D. Skocypec
MS0835 1513	R. C. Dykhuizen
MS0835 1513	V. J. Romero
MS0835 1513	Dayfile
MS0825 1515	R. S. Baty
MS0825 1515	W. H. Rutledge

Nomenclature

C	thermal heat capacitance (1200 J/kg-K)
d	droplet diameter (0.1 m)
D	splat diameter (m)
g	gravitational acceleration (m/s^2)
H	splat thickness (m)
K	thermal conductivity (2.5 W/m-K)
Re	Reynolds number, $\rho Ud/\mu$
t	time
U	impact velocity (m/s)
V	splat volume (m^3)
We	Weber number, $\rho_L U^2 d/\sigma$

Greek

δ	penetration of thermal wave (m)
σ	surface tension ($0.3\ J/m^2$)
ρ	density ($2500\ kg/m^3$)
μ	droplet viscosity ($1000\ N\text{-}s/m^2$)

Intentionally Left Blank

Appendix F

R.C. Dykhuizen

Motion of a Viscous Liquid Exposed to Various Acceleration Fields

Intentionally Left Blank

Sandia National Laboratories

Albuquerque, New Mexico 87185

date: January 24, 1995

to: John Feddema, Org. 2111, MS-0949

from: R. C. Dykhuizen, 1513

subject: Motion of a viscous liquid exposed to various acceleration fields

Introduction and summary

Department 1513 was asked to estimate the motion of a molten glass blob sitting on a flat surface that was accelerated. Two accelerational motions are of concern. First is the lateral acceleration of the substrate that would simulate the motion of a robotic handler moving the glass from one station to another. The second acceleration of concern is the rotation of the substrate. Experimental observations of a rotating substrate have shown that this motion helps spread out the glass onto the substrate.

The analysis presented in this memo provides an estimate for the motion of the molten glass which experiences the above accelerations. From the analysis, one can impose limits on the robotic motions that are performed.

Linear Accelerations

Figure 1 shows the linear acceleration considered in this section. The molten glass blob is resting on a flat substrate that is accelerated to the right. This will cause the glass blob to move to the left in the reference plane that accelerates along with the substrate.

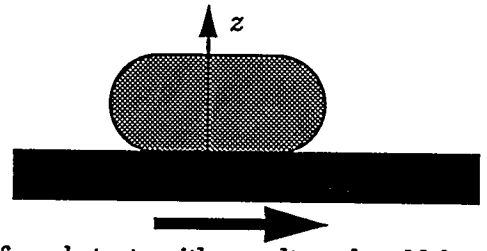

Figure 1: Acceleration of a substrate with a molten glass blob.

The following equation is used to estimate the motion of the molten glass blob of figure 1:

$$\rho \frac{\partial u}{\partial t} = \frac{\partial \tau_{zx}}{\partial z} \tag{1}$$

where ρ is the glass density, u is the glass velocity in the direction of acceleration, τ is the shear stress, and z is the coordinate normal to the substrate. The shear stress is defined as:

$$\tau_{zx} = \mu \frac{\partial u}{\partial z} \tag{2}$$

where μ is the glass viscosity. The boundary conditions that are required are that the velocity at the lower boundary is equal to the substrate velocity (at), and that the partial derivative of the velocity with respect to z at the upper boundary is zero. The initial condition is zero velocity everywhere.

By use of the following transformation:

$$u = at + f(z) , \tag{3}$$

the glass velocity (f) is written in the reference plane of the accelerating substrate. A constant acceleration (a) is assumed. Note that the transformed glass velocity, f, is assumed to only be a function of z. By ignoring any time dependence in f, this analysis will not be applicable for early times when the effect of the accelerating plate is not felt by the upper layers of the molten glass. This time period can be estimated from the following equation:

$$\Delta t = \frac{\rho \delta^2}{\mu} \tag{4}$$

where δ is the thickness of the layer. For thin layers of the viscous glass melt, this time is typically small. For a 10 cm thick layer of 10,000 poise material, the transient time is approximately 0.025 seconds. To estimate how much relative motion occurs between the glass blob and the substrate during this transient time period, I will assume that the glass does not move at all (in the inertial reference frame) during this time period. Thus, the relative movement is equal to the negative of the distance the plate moves in this time period:

$$\Delta x = -\int_0^{\frac{\rho\delta^2}{\mu}} (at)\, dt = \left(\frac{-a}{2}\right)\left(\frac{\rho\delta^2}{\mu}\right)^2 \tag{5}$$

By using the approximation of equation 3, the initial condition is no longer involved, and equation 1 becomes an ordinary differential equation:

$$\rho a = \mu f'' \tag{6}$$

The transformed boundary conditions are zero velocity at the substrate, and a zero derivative in the velocity at the free surface. The solution to equation 6 is:

$$f = \frac{\rho a}{\mu}\left(\frac{z^2}{2} - \delta z\right) \tag{7}$$

To estimate how fast the glass blob moves when the substrate is accelerated, the average velocity can be obtained by integrating equation 7. The average velocity is given below:

$$\langle f \rangle = -\frac{\rho a \delta^2}{3\mu} \tag{8}$$

The average velocity is negative indicating that the glass blob will move in the opposite direction in which the substrate is accelerated.

To estimate the total distance the glass blob moves, it is simply required to multiply equation 8 by the length of time that the substrate is accelerated (Δt), and add this to the result from equation 5. This total relative movement is given below (the negative sign has been deleted):

$$\Delta x = \left(\frac{\rho a \delta^2}{2\mu}\right)\left(\frac{\rho \delta^2}{\mu} + \frac{2\Delta t}{3}\right) \tag{9}$$

Equation 9 can be used to estimate the movement of the glass blob relative to the substrate during the substrate acceleration. Note that the movement has a strong dependence on the thickness of the blob (δ). For the following assumed conditions:

$a = 0.1G = 0.98 m/s^2$ $\mu = 10{,}000$ poise $\rho = 2.5$ g/cc

$\delta = 5$ cm $\Delta t = 0.5$ seconds

it is found that the molten glass blob will move 1 mm with respect to the substrate. Only 2 percent of this motion is due to the movement during the transient start-up (the first term in the second parentheses of equation 9).

Since, the glass tends to stick to the substrate, motion of the left and right ends (figure 1) of the glass blob will not track each other as assumed in the above analysis. Also, the thinning of the glass blob due to gravitational forces (memo to J. Feddema from R. C. Dykhuizen, Jan. 11, 1995) has been ignored here. These two mechanisms will prevent the glass blob from returning to its original position upon deceleration.

Rotation

At the January 12 meeting, rotation was discussed as a possible mechanism for spreading the molten glass blob on the substrate. Al Gossie of Corning stated that they had experimental success with this method, but it had not been incorporated into any production line. In this section a scaling analysis of the molten glass motion due to rotation is provided.

The following equation describes the flow for a rotating substrate relative to the rotating frame (W. D. Morris, Heat Transfer and Fluid Flow in Rotating Coolant Channels, Research Studies Press, 1981):

$$\rho\frac{\partial u}{\partial t}+\rho u\frac{\partial u}{\partial r}+\frac{\rho v\partial u}{r\,\partial\theta}+\rho w\frac{\partial u}{\partial z}-\frac{v^2}{r}-2\omega v=\mu\left(\frac{1}{r^2}\frac{\partial^2 u}{\partial\theta^2}+\frac{1}{r\partial r}\left(r\frac{\partial u}{\partial r}\right)-\frac{u}{r^2}-\frac{2}{r^2}\frac{\partial v}{\partial\theta}+\frac{\partial^2 u}{\partial z^2}\right)+\rho\omega^2 r \tag{10}$$

where u is now the radial velocity, and ω is the constant rotational speed (radians/second) of the cylindrical coordinate system about the z axis. It will be assumed that the axial velocity (w), and the azimuthal velocity (v) are not significant when compared to the radial velocity. Recall that all velocities are relative to a rotating coordinate system.

The accelerational period where the substrate approaches its constant rotational velocity is ignored. It is assumed that the velocity can be written as a linear function of the radial position:

$$u = rf(z,\delta) \tag{11}$$

The linear dependance on the radial position admits a solution with uniform thinning of the glass blob. The velocity form assumed is an implicit function of time through the parameter δ, which is the blob height. If the vertical and tangential velocities are assumed small, the following equation is obtained:

$$\mu f'' = -\rho\omega^2-\rho f^2 \tag{12}$$

The last term causes difficulty because it makes the ordinary differential equation non-linear. It will at first be assumed that this term is zero. Then the solution is easily obtained. The boundary conditions on f are zero at zero elevation, and a zero gradient at δ. The solution is for the radial velocity is easily obtained:

$$u = \frac{\rho r\omega^2}{\mu}\left(\delta z-\frac{z^2}{2}\right) \tag{13}$$

To check if ignoring the non-linear term in equation 12 is proper, we can now evaluate the solution to determine when the non-linear term is indeed small.The maximum value of the function f is when it is evaluated at the free surface. So the magnitude of the two terms on the right hand side of equation 12 can be conservatively compared at the free surface. It is found that when the following is true, equation 13 provides a reasonable approximation of the solution:

$$\left(\frac{\rho\delta^2\omega}{2\mu}\right)^2 \ll 1 \tag{14}$$

Equation 14 is satisfied for many conditions, including those given in the example problem that follows equation 21, in which case the term on the left-hand-side of equation 14 is 0.0001.

We must still determine the time dependence of the blob thickness δ. The volume of the blob is estimated from the maximum radius (R) and the height:

$$V = \pi R^2\delta \tag{15}$$

The differential of the volume is zero:

$$dV = 0 = \pi R^2 d\delta + 2\pi R\delta dR \tag{16}$$

The average velocity of the blob at the maximum radius is used to estimate the radial growth rate of the blob:

$$\frac{dR}{dt} = \frac{1}{\delta}\int_0^{\delta} u(R,z)\,dz = \frac{\delta^2 \rho\omega^2 R}{3\mu} \tag{17}$$

Equations 13 through 16 are combined to determine the thinning of the slab as a function of time:

$$\frac{d\delta}{dt} = -\frac{2\delta^3 \rho\omega^2}{3\mu} \tag{18}$$

The solution to equation 18 is easily obtained:

$$\delta = \left(\frac{1}{\delta_o^2} + \frac{4t\rho\omega^2}{3\mu}\right)^{-\frac{1}{2}} \tag{19}$$

Then, using equations 15, one can obtain the radial extent of the blob as a function of time:

$$\frac{R}{R_o} = \left(1 + \frac{4\delta_o^2 t\rho\omega^2}{3\mu}\right)^{\frac{1}{4}} \tag{20}$$

Equation 19 applies only to a cylindrical blob of molten glass on the substrate. It is important to recall that Al Gossie of Corning indicated that many real industrial processes do not yield cylindrical blobs, but blobs of irregular shapes. Therefore, equation 20 should only be used as an approximate scaling analysis of the movement of molten glass on a rotating substrate.

It is interesting to compare the above solution to that obtained earlier for the flattening of the molten glass blob due to gravitational forces (memo to J. Feddema from R. C. Dykhuizen, Jan. 11, 1995):

$$\frac{R}{R_o} = \left(1 + \frac{8\delta_o^3 t\rho g}{R_o^2 \mu}\right)^{\frac{1}{8}} \tag{21}$$

For the following assumed conditions:

ω =100 rpm μ = 10,000 poise ρ = 2.5 g/cc

δ_o = 5 cm R_o = 10 cm

it is found that 16 seconds are required to double the radius due to spinning the substrate, and 100 seconds are required due to gravitational flattening. Further, the flattening rate due to spinning decreases slower.

Conclusions

In this memo the scaling laws for molten glass blob movement are derived. These motions are due to linear acceleration of the substrate, or spinning of the substrate. The motion of the glass blob due to linear accelerations is predicted. These are found to be small for nominal linear acceleration rates.

As found experimentally by Corning, spinning of the substrate, even at modest rates, causes significant spreading (over what would occur due to gravitational forces alone). However, since the initial molten glass blobs are not cylindrical, prediction of the molten glass motion will require a much more detailed analysis than presented here.

Keywords: thermal sciences, 4199.100 (Corning CRADA)

Distribution:

MS0828 1502	P. J. Hommert (route to: 1511)
MS0441 1503	J. H. Biffle (route to: 1517, 1518)
MS0828 1504	E. D. Gorham (route to: 1514)
MS0834 1512	A. C. Ratzel (route to: 1516)
MS0835 1513	R. D. Skocypec
MS0835 1513	R. C. Dykhuizen
MS0835 1513	V. J. Romero
MS0835 1513	Dayfile
MS0825 1515	R. S. Baty
MS0825 1515	W. H. Rutledge

conf paper cycled separately ds

DISTRIBUTION LIST

186 UC810

SNL/NM	Mailstops	Names, Orgs
1	0151	G. Yonas, 9000
1	0322	P.J. Eicker, 9600
1	0949	R.W. Harrigan, 9602
1	0505	P.A. Molley, 2336
5	0949	Rush Robinett, 9611
1	0951	D.R. Strip, 9621
1	0660	M.E. Olson, 9622
1	1176	R.D. Palmquist, 9651
1	1177	D.S. Horschel, 9661
1	1006	P. Garcia, 9671
1	1007	A.T. Jones, 9672
1	0310	A.C. Bustamante, 2416
1	0439	D.R. Martinez, 9234
1	0825	W. Rutledge. 9115
1	0835	R.D. Skocypec, 9113
5	0439	Clark Dohrmann, 1434
5	0439	Gordon Parker, 1434
5	0825	Roy Baty, 1515
5	0835	Ron Dykhuizen, 1513
5	0835	Vicente Romero, 1513
10	0949	J. T. Feddema, 9611
1	0949	K.S. Kwok, 9611
1	0949	Dan Schmitt, 9611
5	0949	D.S. Lenfest, 9602
1	0949	J.D. Stauffer, 9602
1	0949	D.M. Kozlowski, 9672
1	0800	Central Technical Files, 8523-2
5	0899	Technical Library, 134414
2	0899	Technical Library, 134414
1	0619	Print Media, 12615
2	0100	Document Processing, 7613-2 for DOE/OSTI

•U.S. GOVERNMENT PRINTING OFFICE 1996-0-774-030/20028